

Modeling and Testing of a Series Elastic Actuator with Controllable Damping

by

Sidharth Iyer

A Thesis

Submitted to the Faculty

of the

WORCESTER POLYTECHNIC INSTITUTE

in partial fulfillment of the requirements for the

Degree of Master of Science

in

Mechanical Engineering

by

---

Jan 2012

APPROVED:

---

Dr. Stephen Nestinger, Major Advisor

---

Dr. John J. Blandino, Graduate Representative

---

Dr. Michael Demetriou, Grad Committee

---

Dr. Gregory Fischer, Grad Committee

# Acknowledgements

I would like to acknowledge Professor Stephen Nestinger, my thesis advisor, Professor Michael Demetriou and Professor Gregory Fischer, my thesis committee members, and Professor John Blandino my graduate committee representative. I would also like to acknowledge Neil Whitehouse for his assistance in constructing the testbed, Barbara Fuhrman for her assistance in ordering parts, and Barbara Edilberti for her assistance with setting up the defense.

I would also like to acknowledge my parents, Suresh and Shantha Iyer, and my uncle Velayudhan Nair for all their help and support.

# Abstract

Compliant actuators are much safer than traditional stiff joint actuators, but at the cost of high overshoot, positional accuracy, and speed. A damper that varies its damping torque during motion is introduced to alleviate these downsides. The equations of motion for the system are derived and simulated. The simulations demonstrated a decrease in the overshoot and ringing time. A physical proof of concept was manufactured and tested. The results from the physical model were inconclusive due to a fault in the physical model. A more accurate physical test model using an MR damper is proposed and simulated. The simulation is shown to capture both the static and dynamic nonlinearities of the damper.

# Table of Contents

<b>ACKNOWLEDGEMENTS</b> .....	<b>I</b>
<b>ABSTRACT</b> .....	<b>II</b>
<b>TABLE OF CONTENTS</b> .....	<b>III</b>
<b>LIST OF FIGURES</b> .....	<b>V</b>
<b>LIST OF TABLES</b> .....	<b>VIII</b>
<b>INTRODUCTION</b> .....	<b>1</b>
1.1    BACKGROUND .....	1
1.2    COMPLIANT ACTUATORS.....	3
1.2.1    Series Elastic Actuators.....	3
1.2.2    Magnetorheological Actuators.....	5
1.3    ADVANTAGES AND DISADVANTAGES OF COMPLIANCE .....	7
1.4    COMPLIANCE WITH PRECISION .....	8
1.5    THESIS LAYOUT .....	9
<b>SEA WITH CONTROLLABLE DAMPING</b> .....	<b>11</b>
2.1    MATHEMATICAL MODEL.....	14
2.1.1    Series Elastic Actuator Model.....	14
2.1.2    Series Elastic Actuator with Controllable Damping Model .....	16
2.1.3    Simplification of the Equations of Motion.....	17
2.2    COMPARISON OF THE MODELS .....	20
2.2.1    Series Elastic Actuator Case .....	20
2.2.2    Series Elastic Actuator with Controllable Damping Cases.....	22
2.3    ALTERNATIVE DAMPER CONTROL STRATEGY .....	25

<b>EXPERIMENTAL VALIDATION .....</b>	<b>31</b>
3.1 ROTOR-CALIPER VALIDATION.....	32
3.2 DESIGN AND MANUFACTURING .....	37
3.3 COMPLIANCE .....	39
3.4 COMPONENTS .....	40
3.5 CONTROL.....	43
3.6 TESTING .....	48
<b>RESULTS.....</b>	<b>50</b>
4.1 STIFF JOINT CASE .....	51
4.2 SERIES ELASTIC ACTUATOR CASE.....	52
4.3 SERIES ELASTIC ACTUATOR WITH CONTROLLABLE DAMPING CASE .....	56
4.4 ANALYSIS .....	59
4.4.1 <i>Maximum Overshoot</i> .....	60
4.4.2 <i>Ringing Time</i> .....	60
<b>MR FLUID BASED CONTROLLABLE SEA DESIGN .....</b>	<b>62</b>
5.1 MODELING AN MR DAMPER .....	62
5.2 SELECTING AN MR FLUID .....	65
5.3 CHOOSING KEY MR DAMPER DIMENSIONS.....	66
5.4 SIMULATION OF THE SEA-CD WITH A MR DAMPER.....	68
<b>FUTURE WORK .....</b>	<b>72</b>
<b>CONCLUSION.....</b>	<b>73</b>
<b>REFERENCES .....</b>	<b>74</b>
<b>APPENDIX A .....</b>	<b>80</b>
<b>APPENDIX B.....</b>	<b>86</b>
<b>APPENDIX C .....</b>	<b>93</b>

# List of Figures

Figure 1: A Series Elastic Actuator .....	3
Figure 2: Force measurement in an SEA .....	4
Figure 3: Schematic of a Magnetorheological Damper [19] .....	6
Figure 4: SEA (upper) and SEA-CD (lower) comparison .....	11
Figure 5: Block diagram of an SEA.....	14
Figure 6: Block diagram of a SEA-CD.....	16
Figure 7: Result of the SEA Simulation .....	21
Figure 8: Error between the arm and motor position in the SEA case .....	21
Figure 9: Comparison of the arm response for each test case.....	23
Figure 10: Arm-motor error at varied damping rates.....	24
Figure 11: Comparison of two damper control strategies for $b = 10$ .....	26
Figure 12: Comparison of two damper control strategies for $b = 20$ .....	27
Figure 13: Comparison of two damper control strategies for $b = 50$ .....	28
Figure 14: Comparison of two damper control strategies for $b = 100$ .....	29
Figure 15: Comparison of two damper control strategies for $b = 200$ .....	29
Figure 16: The entire test bed .....	32
Figure 17: Friction force vs. velocity in a caliper at different normal forces on the caliper. Higher damping force magnitude corresponds to higher normal forces.....	33
Figure 18: Shear stress vs. Velocity in a MR damper. Higher stress magnitudes correspond to higher magnetic fields.....	34
Figure 19: Motive force vs. Friction force in a rotor-caliper .....	35
Figure 20: Shear stress vs. Motive Force in a MR damper.....	36

Figure 21: SolidWorks Model of the Test Bed.....	37
Figure 22: Image of the error from the laser cutter cutting too thick of a plastic. The square edges should be flush.....	38
Figure 23: The antagonistic spring setup .....	39
Figure 24: The motor, gearbox and encoder .....	40
Figure 25: Image of the rotor-caliper setup .....	41
Figure 26: Image of the servo connected to the rotor-caliper setup .....	42
Figure 27: The US Digital encoder connected to the arm .....	43
Figure 28: Motor encoder calibration .....	45
Figure 29: Result for the stiff case .....	51
Figure 30: Result from the Undamped Case.....	52
Figure 31: Test 1: Arm and Motor response .....	53
Figure 32: Test 1: Arm-Motor error.....	54
Figure 33: Test 2: Arm and Motor response .....	54
Figure 34: Test 2: Arm-motor error .....	55
Figure 35: Controllably damped case .....	56
Figure 36: Test 1: Arm and Motor response .....	57
Figure 37: Test 1: Arm-motor error .....	58
Figure 38: Test 3: Arm and Motor response .....	58
Figure 39: Test 3: Arm-motor error .....	59
Figure 40: SolidWorks model of a prototype MR damper .....	64
Figure 41: Comparison of Damping torque at different angular velocities ( $h = .2 \text{ mm}$ )..	66
Figure 42: Comparison of Damping torque at different angular velocities ( $h = .02 \text{ mm}$ )	67

Figure 43: No magnetic field .....	70
Figure 44: Small magnetic field $\tau B = 5 \text{ kPa}$ .....	70
Figure 45: Higher magnetic field $\tau B = 10 \text{ kPa}$ .....	71
Figure 46: Test 3: Arm and Motor position .....	93
Figure 47: Test 3: Arm-motor error .....	94
Figure 48: Test 4: Arm and Motor position .....	94
Figure 49: Test 4: Arm-motor error .....	95
Figure 50: Test 5: Arm and Motor position .....	95
Figure 51: Test 5: Arm-motor error .....	96
Figure 52: Test 2: Arm and Motor response .....	97
Figure 53: Test 2: Arm-motor error .....	97
Figure 54: Test 4: Arm and Motor response .....	98
Figure 55: Test 4: Arm-motor error .....	98
Figure 56: Test 5: Arm and Motor response .....	99
Figure 57: Test 5: Arm-motor error .....	99



# List of Tables

Table 1: Simulation Parameters .....	19
Table 2: Max damping rates for the controlled damping cases .....	22
Table 3: Comparison of Crossing Times .....	26
Table 4: PID gains .....	47
Table 5: Simulated MR damper specifications .....	69

# Chapter 1

## Introduction

### 1.1 Background

At present, most robots are designed for precise positioning, and rapid motion. In industrial settings, high precision allows for tight control over the variations between successive parts, and rapid motion increased the throughput of the robot.

However, robots are increasingly seen as potential assistants for humans. The National Robotics Initiative, for instance, is a NSF program to encourage research into

co-robots acting in direct support of individuals and groups. These co-robots will work directly alongside humans in homes and work areas.

In 1979, Robert Williams was killed in an Industrial accident when he was struck by a robotic arm in a casting plant in Flat Rock, Michigan [1]. In 1981, Kenji Urada was killed when he was pushed into a grinder while attempting routine maintenance on a robot he neglected to properly shut down [2]. Accidents such as these can be prevented by using safety measures such as light curtains that stop the machine if something breaches the workspace of the robot, safety fences that restrict access to the work area, and pressure pads that stop the robot if they detect an increase in pressure [3]. These safety measures and precautions have been codified for the USA in the ANSI/RIA R15.06-1999 [4], and work on the basis of restricting access to the work area of the robot while the robot is in motion, and immediately shutting down the robot if a foreign object enters the work area. These safety measures are impractical in situations where a robot must work closely with a human such as robot assisted rehabilitation and co-robot assembly.

The root cause of the accidents mentioned above is the lack of compliance within the robot design. By introducing compliance, robot parts can run into other robots and humans without generating forces high enough to cause damage, and therefore safely work in close proximity with humans and other robots.

## 1.2 Compliant Actuators

There are many implementations of compliant actuators. The two with the most publications behind them are presented below. They are Series Elastic Actuators (SEAs), and Magnetorheological Actuators (MRAs).

### 1.2.1 Series Elastic Actuators

One implementation of a compliant actuator is the Series Elastic Actuator as described by Pratt and Williamson [5]. SEAs are actuators with a spring in series between the actuator and the actuated link, as shown in Figure 1.

There are variations on the concept, such as Robinson and Pratt's hydraulic SEA [6], Park and Song's compact non-linear spring setup [7], and Wang and Huang's variable stiffness actuator [8]. In all of these cases, the spring serves as the compliant element, and its inertia is dramatically lower than the inertia of a gearbox and motor. Since the spring is in series with the actuator and the link, the deflection of the spring corresponds directly with the force applied from the actuated link to the actuating link.

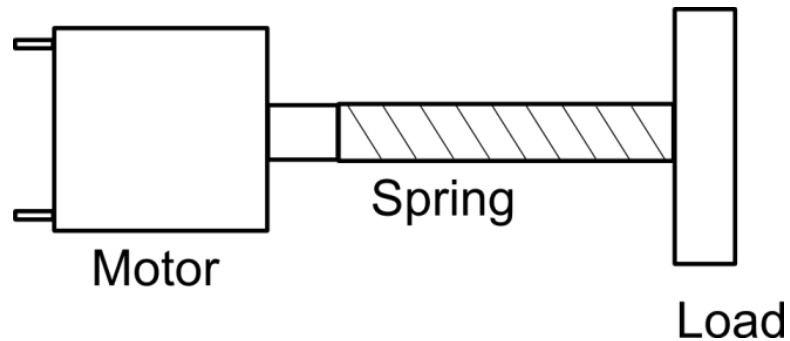


Figure 1: A Series Elastic Actuator

Measuring the deflection gives the component of the force or torque acting along the joint. Figure 1 demonstrates an example. The torque acting on the load,  $T_l$ , causes the

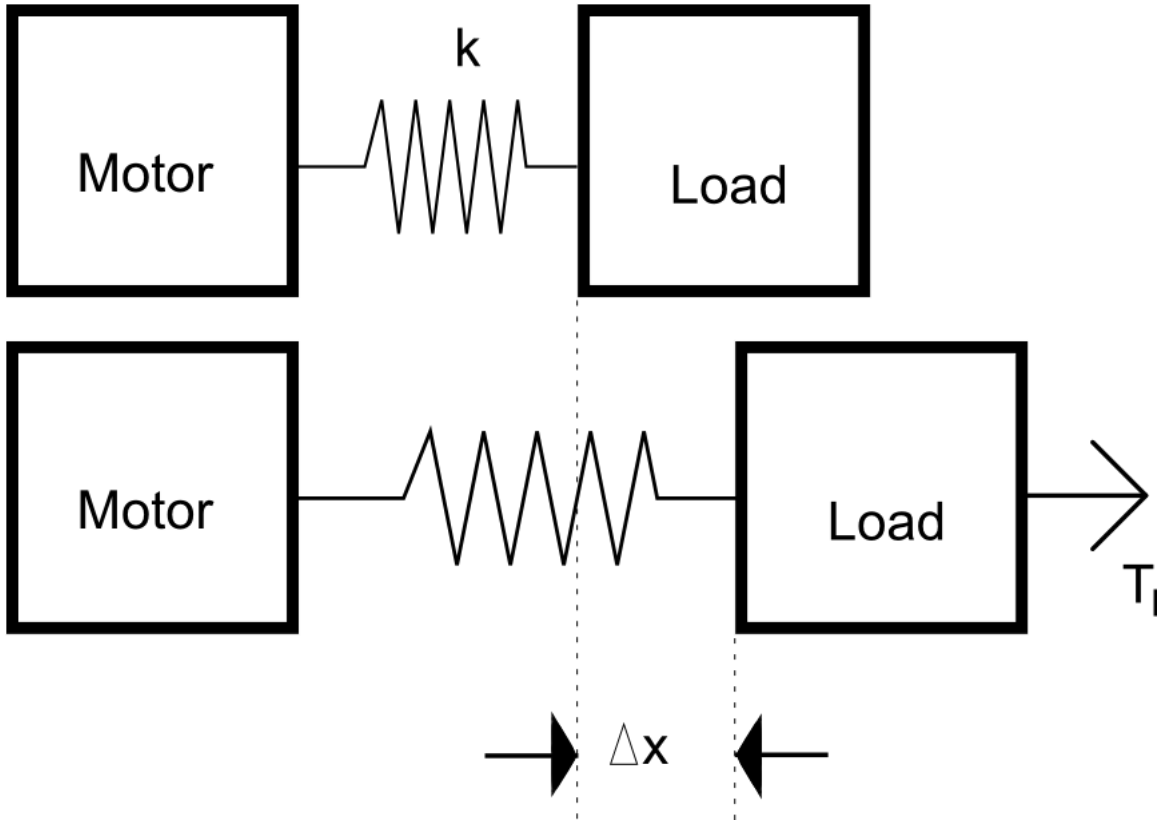


Figure 2: Force measurement in an SEA

spring to displace by  $\Delta x$ . By measuring  $\Delta x$  however,  $T_l$  can be predicted via Hooke's law ( $T_l = k \cdot \Delta x$ ). Altwegg uses this property to implement a torque controller for an SEA [9].

The ease of measuring the force acting on a joint has found use in medical applications. Sensinger and Weir proposed a non-back driveable SEA that would not require power to remain in place, for use in braces meant to assist with physical rehabilitation [10] [11]. Oblak, Cikajlo, and Matjacic developed a system for arm and wrist rehabilitation using an SEA [12], and Lagonda, Schouten, Stienen, Hekman, and

van der Kooij designed an SEA for a robot that would assist in gait rehabilitation training [13]. Kong, Bae and Tomizuka developed and tested a control algorithm for SEAs used in powered assist applications [14].

Another interesting property is the use of the spring for temporary energy storage, like a capacitor. While working on developing jumping gaits, Curran and Orin showed that in each optimal gait, the springs in the SEAs are compressed just before the motor is driven forward [15]. This advantage has been used by others in developing legged robots [16] [17].

SEA's are limited by their springs, however. Like pneumatic systems, SEAs offer excellent force control at the cost of positional accuracy and unwanted dynamic characteristics. Wyeth demonstrates a control method that provides accurate velocity control, but not position control [18]. Other limitations of Wyeth's method include the inability to deal with discontinuous velocity profiles, slower rise time, and greater energy consumption.

## **1.2.2 Magnetorheological Actuators**

In an MRA, an MR fluid damper is used as the compliant element. Much like the SEA, the MR damper is placed in series between the motor and the load. A MR fluid is a fluid whose rheology is affected by magnetic fields within the volume of the fluid [19]. One example of the changing rheology of MR fluids is a MR fluid clutch, where the viscosity of the fluid can be raised high enough to lock the input and output shafts together, and lowered to decouple the shafts. In an MR damper, an electromagnet is used

to control the magnetic field within the damper. By varying the current to the

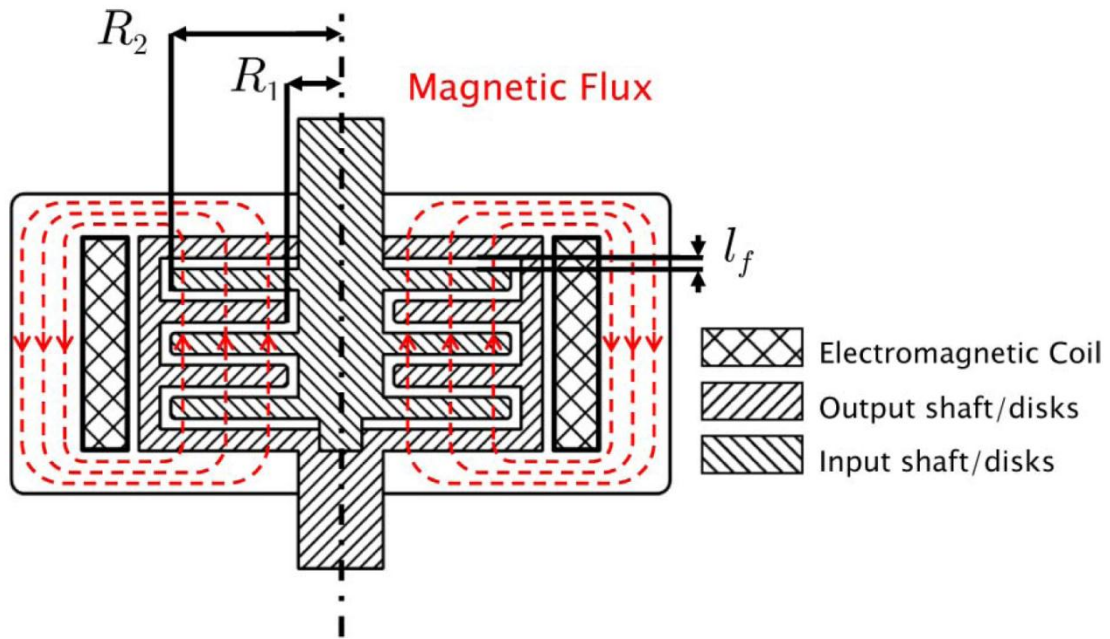


Figure 3: Schematic of a Magnetorheological Damper [19]

electromagnet, the viscosity of the fluid, and therefore the damping coefficient, can be controlled. A close relative of MR fluid is Electrorheological (ER) fluid whose rheology changes in an electric field. ER dampers are not commonly used however because ER fluid requires very high electric fields, and cannot increase its viscosity to the same degree an MR fluid can. Figure 3 shows a schematic of a MR damper. When a magnetic field is present, the MR fluid behaves like a Bingham plastic [20]. Takesue, Furusho, Kiyota, and Sakaguchi demonstrated quick response and accurate torque control using a MR actuator [21] [22] [23]. Shafer and Kermani further demonstrated that it is possible to get accurate torque control, and low reflected inertia without using an explicit torque sensor when controlling a MRA [24]. Ahmed and Kalaykov built a MRA and conducted physical tests to demonstrate the safety of these actuators under collisions [25] [26].

Like the SEAs presented earlier, MRAs are safe enough for use in medical applications. Kikuchi, Oda, and Furusho developed and utilized a MRA for use in leg braces designed to prevent spastic movement in brain damaged patients [27].

It should be noted that MRAs and SEAs are not compliant in the same manner. SEAs use a spring to allow for relative motion, while MRAs can disengage and allow one part to freely rotate around another. In this sense, compliance refers to a mechanism that allows two parts to passively move when acted upon by an external force.

### **1.3 Advantages and Disadvantages of Compliance**

Traditional robot construction guidelines dictate that joints must be as stiff as possible [28]. Non-stiff joints introduce errors in the measured position and actual position. These small errors are compounded over multiple joints within the arm to the point where the end effector can be significantly offset from the desired position. Non-stiff joints also introduce unwanted dynamic characteristics such as noticeable harmonics, large overshoots, longer rise times, and longer settling times [29], all of which increase the amount of time required before the arm reaches a desired position and remains there.

Stiff joints do not suffer from the problems of incorrect position measurement and unwanted dynamic characteristics, which is why they are overwhelmingly popular in traditional industrial robots. However, as robotics moves towards co robot systems, the disadvantages of stiff joints become a concern. Simple tasks like handing a part off to another robot require very high precision, since even small offsets will result in large reaction forces. If any link is ever near an obstacle, careful trajectory planning and



tracking is required to avoid crashes, since even small bumps will create large reaction forces in the joints. These forces can be large enough to permanently damage the joint. The joints themselves have very large reflected inertias. Reflected inertia is a measure of how much force it takes for a joint to move when under external forces i.e. not being driven by the actuator. In an unpowered actuator, this is the force required to back drive the gearbox and motor. When moving under power, the control loop may attempt to compensate for the external force by increasing the motor torque, thereby increasing the reflected inertia.

#### **1.4 Compliance with Precision**

Compliance with precision is the concept behind the work presented in this thesis. An actuator that is compliant and precise has high precision, and the capability for rapid motion, while still maintaining compliance. Rapid motion does not refer only to how quickly the joint moves. Rapid motion refers to how quickly the joint converges to commanded positions.

An example of a case where precise and compliant actuators are superior to other actuators is the insertion of a peg into a closely fitting hole. A stiff actuator would have to move to the location, then slowly and accurately position, and orient its end effector to slide the peg into the hole. A compliant system would take time to move to the position, wait for the arm to settle, repeating as necessary if the arm did not settle close enough to the hole, and finally push the peg into the hole. The compliant system does not have to accurately position and orient the peg, since the reaction forces generated by misalignment of the peg will cause the joints to move to reduce the reaction forces. A precise and compliant actuator would rapidly move to the new position, like the precise

actuator, and insert the peg using the reaction forces to align the peg like the compliant actuator.

## **1.5 Thesis layout**

The rest of this thesis is laid out as follows. Chapter 2 begins by introducing the implementation of the precise and compliant actuator presented in the rest of the thesis. Section 2.1 derives the equations of motion for an SEA and an SEA-CD, and their simplifications for purposes of testing. Section 2.2 presents the results from the simulation. Section 2.3 presents an alternative control strategy for the damper, and compares the results against the results presented in 2.2.

Chapter 3 experimentally tests the results of the simulation. Section 3.1 compares the rotor caliper to a MR damper and shows they are broadly similar. Section 3.2 presents the design and fabrication of the test bed. Section 3.3 shows how compliance was implemented in the test bed. Section 3.4 presents the off the shelf components used to complete the test bed. Section 3.5 presents the control scheme used, and how the control scheme was implemented in LabVIEW. Section 3.6 presents the test scenarios and criteria.

Chapter 4 presents and analyses the results of each of the test cases. Section 4.1 presents the data from the Stiff joint case, Section 4.2 presents the data from the Standard SEA case, Section 4.3 presents the data from the SEA-CD case, and Section 4.4 analysis the results of the tests. Chapter 5 begins the process of making a new test platform by modeling a SEA-CD that uses an MR damper. Section 5.1 presents the method used to

model an MR damper, and Section 5.2 gives a brief overview of selecting an MR fluid for the damper. Section 5.3 outlines key dimensions that affect damper performance, and Section 5.4 simulates the system using an MR damper. The thesis concludes by suggesting work that can be done to advance this area of study.

## Chapter 2

### SEA with Controllable Damping

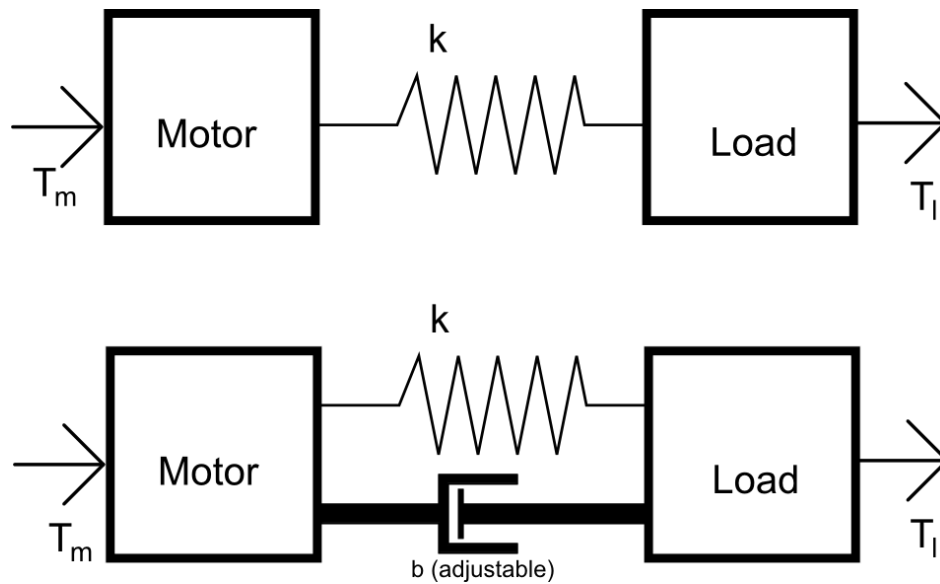


Figure 4: SEA (upper) and SEA-CD (lower) comparison

The implementation of a precise and compliant actuator described in the rest of the thesis is an SEA with a controllable resistive element in parallel with the spring, as shown

in the lower half of Figure 4. The spring serves as the compliant element as in an SEA and the damper is added to impede the relative motion between the load and the motor. If the damper has extremely high damping, the velocity of the load will be locked to the velocity of the motor, just like a conventional stiff actuator. High damping is also as safe as a stiff actuator since the damper will resist any increase in the relative velocity caused by a part of the robot running into another robot or human. On the other hand, if the damper has extremely low damping, it cannot impede much of the relative motion between the motor and the load, and the motion of the load will be dictated by the spring, like an SEA. Low damping is also as safe as an SEA, since the damper will not resist much of the relative motion caused by a part of the robot hitting another robot or a human, which allows the spring to absorb and dissipate the energy of the collision. By controlling the damping rate during motion, the relative velocity and position between the motor and the load, and the safety of the joint can be controlled.

High damping means the relative velocity between the motor and load will be very small, as mentioned earlier. With small relative velocities, the motor position and load position will converge or diverge very slowly. With low damping, the relative velocities can be much larger; therefore, the motor position and load position will converge or diverge quickly. For a precise and compliant actuator, the speed of divergence should be slow, but the speed of convergence should be high. If the damping force can be changed during the motion of the joint, the damper could have high damping when the motor position and load position are diverging and low damping when the motor position and load position are converging.

To further illustrate the need for variable damping, consider a step input. A joint is commanded to a new position, and the motor quickly moves to the new position. During the motion of the motor, the position of the load and the position of the motor is diverging quickly. Activating high damping in this period will slow the diverging rate. Depending on the motor, however, this period of time may be extremely brief, and using the damper during this time may not show any noticeable improvement. Once the motor has reached its desired position, the spring will cause the load position to converge to the motor position. If the damping remains high in this period, the relative velocity between the motor and the load will be small, so the load will converge very slowly. In contrast, lowering the damping in this period will allow for higher relative velocities, which in turn lets the load position converge to the motor position quickly. The low damping during this time also means that if the arm hits something, it will respond like an SEA, allowing the spring to dissipate the impact.

Once the load position has reached the motor position, the inertia of the load will cause the load position to overshoot the motor position (assuming an under damped system), and the load position and motor position will once again begin diverging. Continuing with the low damping from before will mean the inertia of the load is counteracted mostly by the spring, and the low damping will gradually decrease the magnitude of each overshoot until the load position eventually converges to the motor position. However, using high damping from the point in time when the load position crosses the motor position to the point when the load position reaches its maximum overshoot, allows the damper to dissipate more of the kinetic energy of the load, thereby reducing the magnitude of the overshoot. After the maximum overshoot, the load is once

again converging to the motor position, so reducing the damping will allow the load to converge faster. Using this method, subsequent overshoots have much more reduced magnitudes than with constant low damping.

In the rest of this chapter, a mathematical model for the equation of motion of the system is derived for both a SEA, and SEA-CD. The models are simulated using Matlab, and the results are compared. Finally, two damper control strategies are modeled and compared.

## 2.1 Mathematical Model

In order to compare the performance of the SEA and the SEA-CD, the governing equations for both systems are derived and simulated.

### 2.1.1 Series Elastic Actuator Model

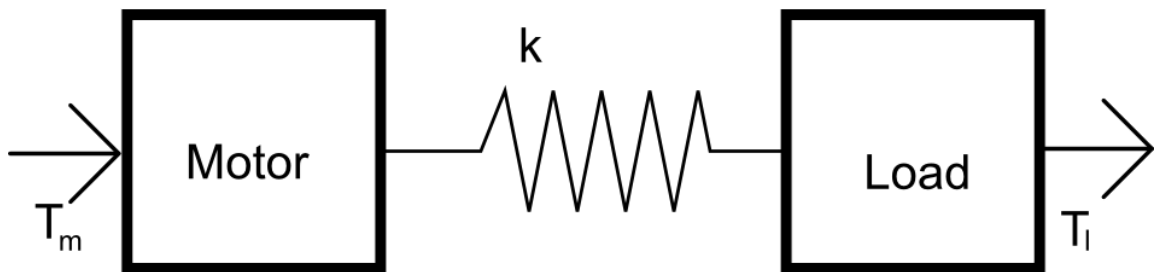


Figure 5: Block diagram of an SEA

Using Figure 5 as the block diagram for an SEA and torques toward the right denoted as positive torques in a right handed co-ordinate system, the system was divided into the motor, spring, and load sections. Newton's method gives the following equations for the motor and the load

$$J_m \ddot{\theta}_m = T_m + T_{bm} + T_s \quad (1)$$

$$J_l \ddot{\theta}_l = T_l - T_s \quad (2)$$

Where  $J_m$  = Inertia of the motor,  $J_l$  = Inertia of the load,  $\ddot{\theta}_m$  = Rotational acceleration of the motor,  $\ddot{\theta}_l$  = Rotational acceleration of the load,  $T_m$  = External Torque acting on the motor,  $T_s$  = Torque from the spring,  $T_l$  = External torque acting on the load, and  $T_{bm}$  (Not shown in Figure 5) is the lumped internal damping of the armature, bearings, and gearbox. It is modeled as a simple damper

$$T_{bm} = b \dot{\theta}_m \quad (3)$$

Where  $b$  = Damping constant, and  $\dot{\theta}_m$  = Rotational velocity of the motor

Assuming the system is using linear springs, they can be modeled as,

$$T_s = k(\theta_l - \theta_m) \quad (4)$$

where  $k$  is the Torsional spring constant,  $\theta_m$  is Rotational position of the motor, and  $\theta_l$  is Rotational position of the load

Inserting Equations (3) and (4) into Equations (1) and (2),

$$J_m \ddot{\theta}_m - b \dot{\theta}_m - k(\theta_l - \theta_m) = T_m \quad (5)$$



$$J_l \ddot{\theta}_l + k(\theta_l - \theta_m) = T_l \quad (6)$$

### 2.1.2 Series Elastic Actuator with Controllable Damping Model

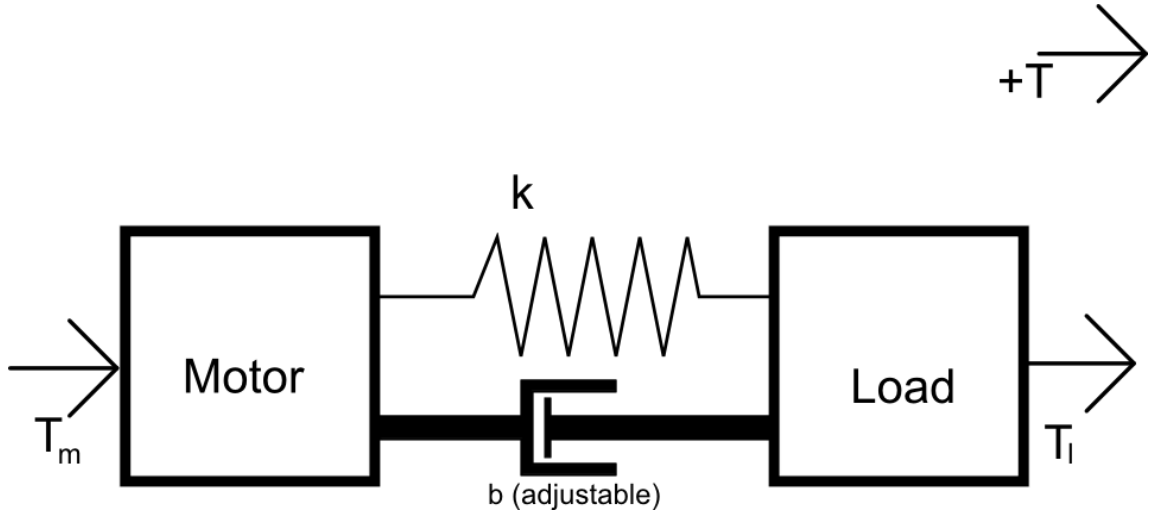


Figure 6: Block diagram of a SEA-CD

Using Figure 6 as the block diagram for the SEA-CD and following the same procedure as before,

$$J_m \ddot{\theta}_m = T_m + T_b + T_s \quad (7)$$

$$J_l \ddot{\theta}_l = T_l - T_b - T_s \quad (8)$$

$$T_s = k(\theta_l - \theta_m) \quad (9)$$

Where  $T_b$  = Torque from the damper

In order to model the damper, the damping coefficient  $b$  is replaced with a nonlinear function  $b(\theta_m, \theta_l, t)$  and assumed to account for all the damping of the system, including  $T_{bm}$  as described in Equation 3. Thus the damper can be represented as:

$$T_b = b(\theta_m, \theta_l, t) \cdot \frac{d}{dt}(\theta_l - \theta_m) \quad (10)$$

Inserting Equations 9 and 10 into Equations 7 and 8 gives:

$$J_m \ddot{\theta}_m - \left[ b(\theta_m, \theta_l, t) \cdot \frac{d}{dt}(\theta_l - \theta_m) \right] - k(\theta_l - \theta_m) = T_m \quad (11)$$

$$J_l \ddot{\theta}_l + \left[ b(\theta_m, \theta_l, t) \cdot \frac{d}{dt}(\theta_l - \theta_m) \right] + k(\theta_l - \theta_m) = T_l \quad (12)$$

Note that the only difference between Equations 11 and 12 and Equations 5 and 6 is the addition of the damping term. Thus only one set of equations needs to be programmed to simulate either an SEA or an SEA-CD. Equation 11 and Equation 12 form a basis for the governing dynamic equations for the SEA-CD.

### 2.1.3 Simplification of the Equations of Motion

Assuming the physical system has no torques acting on the motor and no load,  $T_m$  and  $T_l$  are equal to zero. Assuming  $\dot{\theta}_m$ , and  $\theta_m$  are known and can be supplied as the input, and only the arm response is being tested, Equation 12 can be simplified to

$$J_l \ddot{\theta}_l = -b(\theta_m, \theta_l, t)(\dot{\theta}_l - \dot{\theta}_m) - k(\theta_l - \theta_m) \quad (13)$$

Since Matlab's ODE solver only solves first order ODEs, Equation 13 must be placed in state space format

$$\frac{d}{dt} \vec{x} = \begin{bmatrix} 0 & 1 \\ -\frac{k}{J_l} & -\frac{b(\theta_m, \theta_l, t)}{J_l} \end{bmatrix} \vec{x} + \begin{bmatrix} 0 & 0 \\ \frac{k}{J_l} & \frac{b(\theta_m, \theta_l, t)}{J_l} \end{bmatrix} \vec{u} \quad (14)$$

where  $\vec{x} = \begin{bmatrix} x_1 \\ x_2 \end{bmatrix} = \begin{bmatrix} \theta_l \\ \dot{\theta}_l \end{bmatrix}$ , and  $\vec{u} = \begin{bmatrix} u_1 \\ u_2 \end{bmatrix} = \begin{bmatrix} \theta_m \\ \dot{\theta}_m \end{bmatrix}$

In the simulation of the system with controlled damping, the damping term  $b(\theta_m, \theta_l, t)$  is simplified by splitting it into  $b_0$  and  $b$ , where  $b_0$  represents the lower damping rate of the variable damper, and  $b$  represents the high damping rate of the variable damper. The damper is assumed to switch between the two rates much faster than the response of the components in the joint. Hence, there was no need to put in a ramp where the damping ramps up to the maximum value. This may not always be an accurate model, since real dampers have maximum damping force they can provide such as the maximum torque before any components fail or deform.

The damping control is modeled as a bang-bang system that switches between the low value and a high value given by

$$b(\theta_m, \theta_l, t) = \begin{cases} b_0 & \text{if } zc = 0 \\ b & \text{if } zc = 1 \end{cases}$$

The damper switches to the high value when the difference between motor position and arm position crosses zero ( $zc = 1$ ). It stays in this ‘high’ state for 0.4s, then returns to the low value ( $zc = 0$ ). To simulate a Heaviside step function at  $t = 1$ ,  $\dot{\theta}_m$  is manually set to a delta function.

Equation 14 was solved using Matlab’s ODE45 solver that implements a Runge-Kutta method with a variable time step for efficient computation. The initial conditions were all zero, and the time range was 6 seconds. The rest of the simulation parameters are listed in Table 1.

**Table 1: Simulation Parameters**

Parameter	Numerical Value	Units
L	5	kg·degree <sup>2</sup>
k	80	N·m/degree
b <sub>0</sub>	2	(N·m s/deg)

After running the simulation with these parameters, two plots are created. The first plot shows the motor position over time, and the arm position over time. The second plot shows the difference between the motor and arm position over time.

The Matlab code used to implement Equation 14 is in Appendix A.

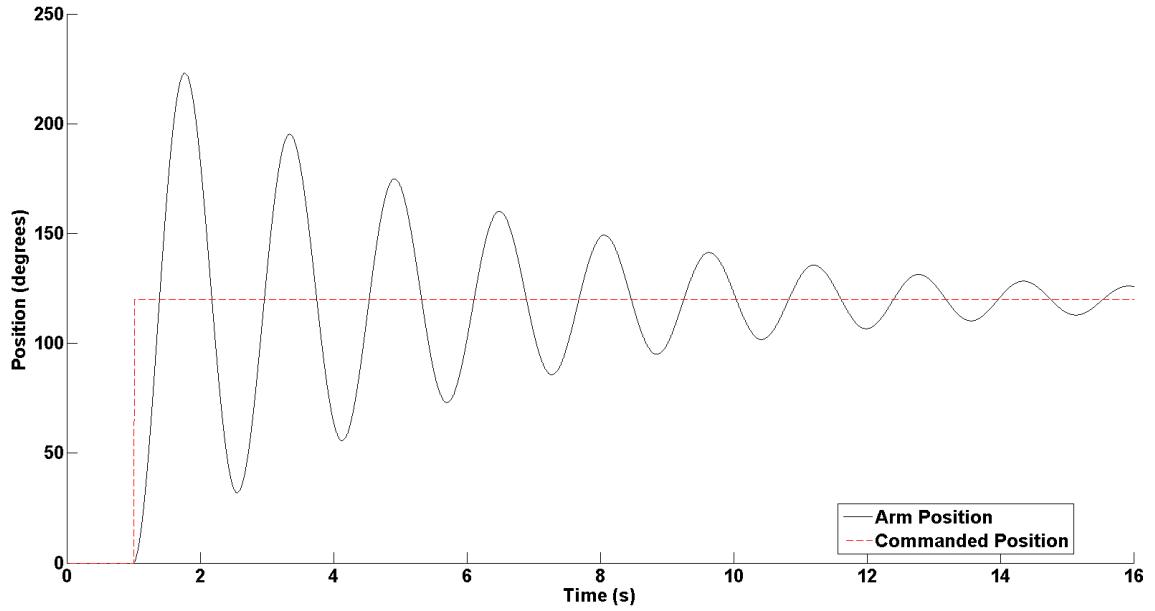
## **2.2 Comparison of the Models**

The next section presents the results from the simulations of the mathematical models derived in Section 2.1.3. Various maximum damping rates are tested, and their dynamic responses are compared. Specifically, the maximum overshoot, and the ringing time (time taken to converge to 5% of the motor position) are compared.

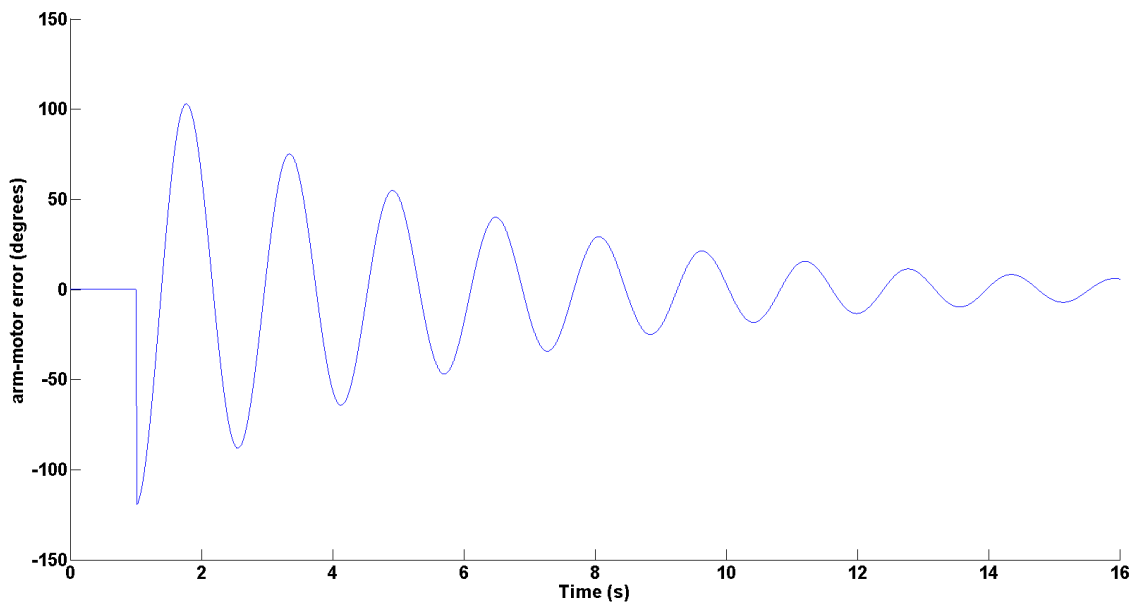
### **2.2.1 Series Elastic Actuator Case**

The first step was to simulate the system where the damper is never activated and remains at its baseline value for the entire motion of the arm. This represents the response of a typical SEA.

As is expected, the arm position behaves like a typical under damped second order system. The arm takes 1.39s to reach the commanded position (the motor input position). Even after 15 s, the system still hasn't settled to the commanded position. There is a high initial overshoot, and a long ringing time.



**Figure 7: Result of the SEA Simulation**



**Figure 8: Error between the arm and motor position in the SEA case**

Figure 8 presents the data to be compared against the following cases. Since the ideal case is a rigid joint, the error between the motor and the arm (arm-motor error) should be zero, or extremely close to zero at all times.

### 2.2.2 Series Elastic Actuator with Controllable Damping Cases

In order to test the effectiveness of different maximum damping rates on the response of the actuator, various maximum damping rates were selected as test cases. The test cases are presented in Table 2. The lower maximum damping rates reflect the behavior of the system if space/weight constraints allowed only for a relatively weak damper, and the higher damping rates demonstrate cases where stronger dampers are used.

Table 2: Max damping rates for the controlled damping cases

Case	Damping Rate (N·m s/deg)
I	10
II	20
III	50
IV	100
V	200

*Case I:* The maximum damping rate was chosen to be 10 (N·m s/deg). Even with this small of an increase in maximum damping, there is a marked improvement in the overshoot and ringing time as can be seen in Figure 9 and Figure 10. The maximum overshoot is around 80, instead of 100, and the system is beginning to settle after 6 seconds, instead of more than 15. There is no change in the time to the first zero crossing (the time to reach the commanded position), which is to be expected since the system has

the same dynamics as a SEA while the damper is inactive, and the damper is inactive until the first overshoot.

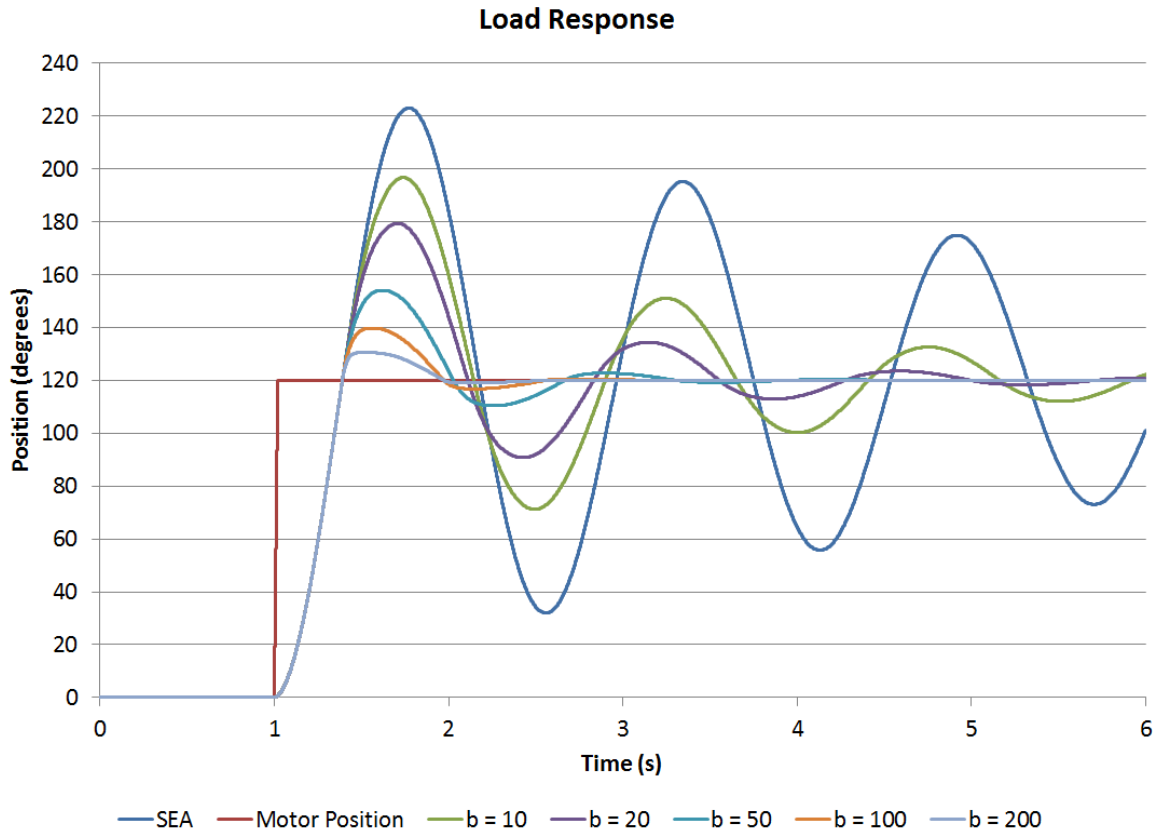


Figure 9: Comparison of the arm response for each test case

**Case II:** Further improvements in the dynamic response is demonstrated. The maximum overshoot of the arm-motor error has been reduced further to around 60, and the ringing time has decreased to around 4 s. Thus, even with a weak damper, drastic improvements in the dynamic characters of a SEA-CD over a SEA can be seen.

**Case III:** Case III continues the trend of decreasing arm-motor error overshoot, and reduces the ringing time to 2.5s. The arm-motor error overshoot was decreased to around 40.



*Case IV:* Diminishing returns from high damping rates is becoming evident. The overshoot is down to 20 degrees, but the ringing time is still around 2 s.

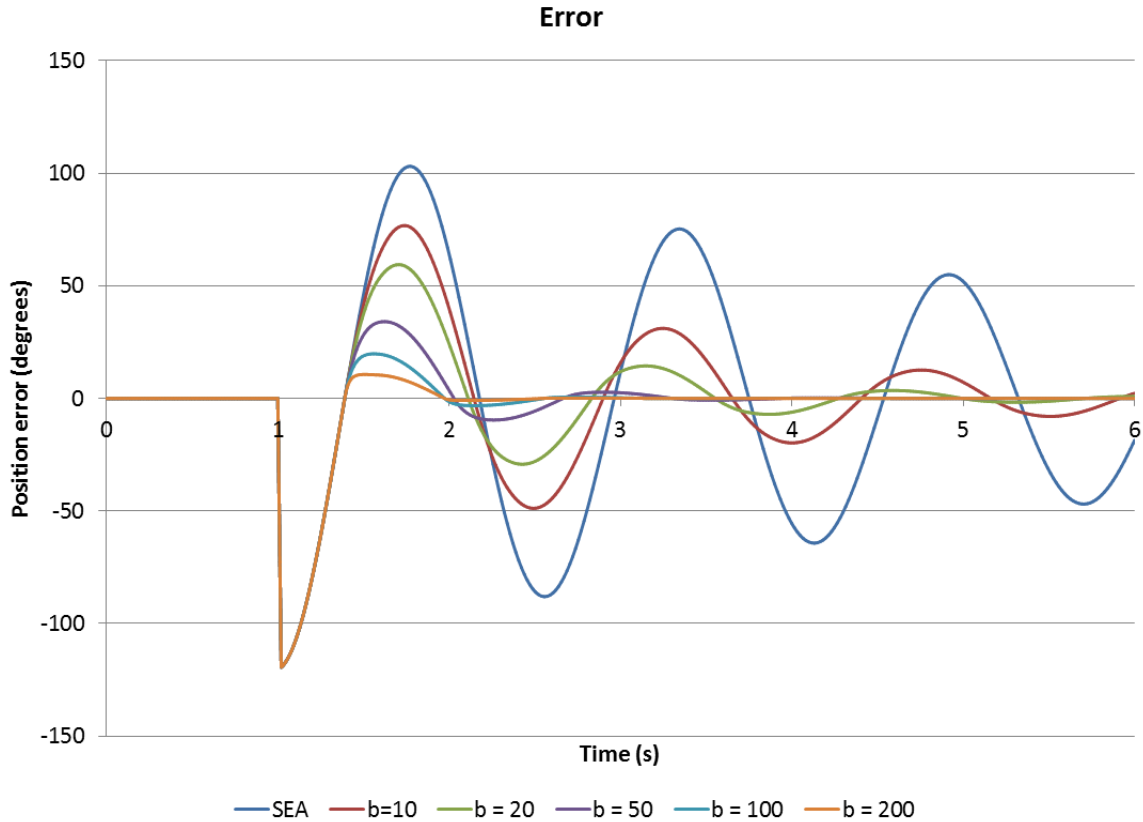


Figure 10: Arm-motor error at varied damping rates

*Case V:* Case V shows what would happen if the damper is powerful enough to almost instantly dissipate the kinetic energy of the load. The system behaves almost like a stiff joint.

After looking at these tests, there are a number of observations that can be made. Using this control scheme for the damper, increasing the damping force has no effect on the rise time of the system, however, the ringing time, and magnitude of overshoot are

reduced. Low damping rates have a high impact on the ringing time, but significantly reducing the overshoot requires more powerful dampers with high damping rates. More importantly adding the variable damper does improve the response of the load in two areas. Firstly, the maximum overshoot is significantly reduced, and secondly the ringing time is significantly reduced.

### **2.3 Alternative Damper Control Strategy**

An alternative damper control strategy is to use high damping at the start of the motion of the load, and use the previous control strategy the rest of the time. The damper is kept inactive until just before the step input. It is then activated, and kept active for a short period just after the step input. The damper then activates again once the arm position crosses the motor position. This control strategy is more complex since it requires knowledge of the planned trajectory before it is executed.

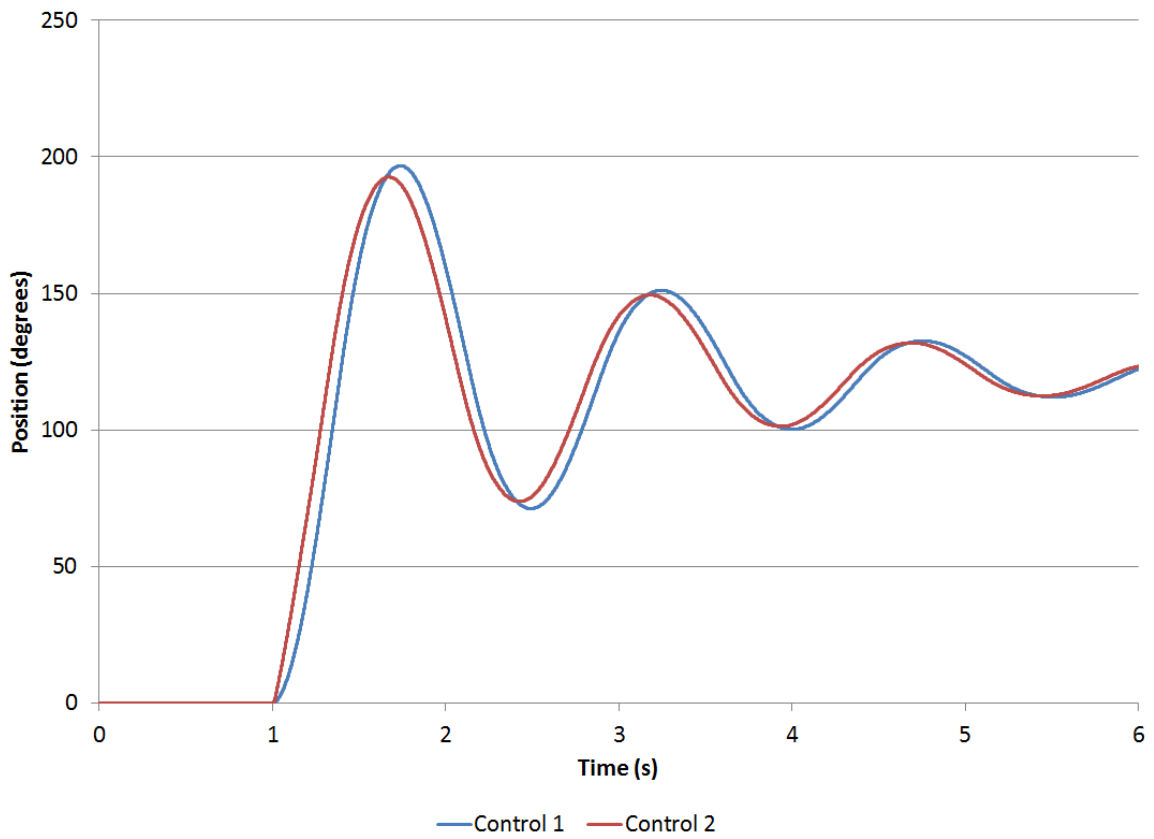
**This strategy keeps the damper inactive during the trajectory execution, so during motion, the reflected inertia motion, the reflected inertia of the joint is governed by the inertia of the spring, just like an SEA. The crossing an SEA. The crossing time (the time taken for arm to first cross the motor position) is given in**

**given in**

Table 3. Figure 11 through Figure 15 compare the results of the simulation. Control 1 refers to the control scheme used in the previous results (Figure 9 and Figure 10). Control 2 is the new control scheme proposed in this section.

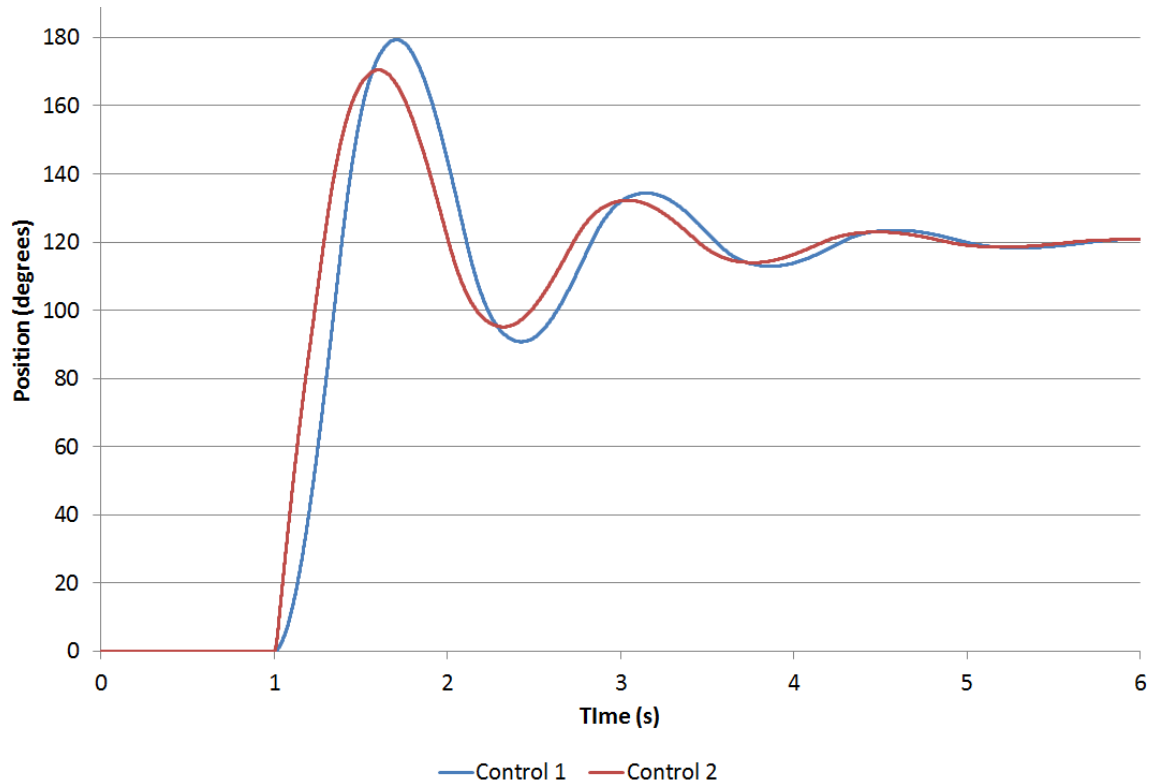
**Table 3: Comparison of Crossing Times**

Case	Original time (s)	Alternative time (s)
I	0.39	0.32
II	0.39	0.29
III	0.39	0.23
IV	0.39	0.18
V	0.39	0.13



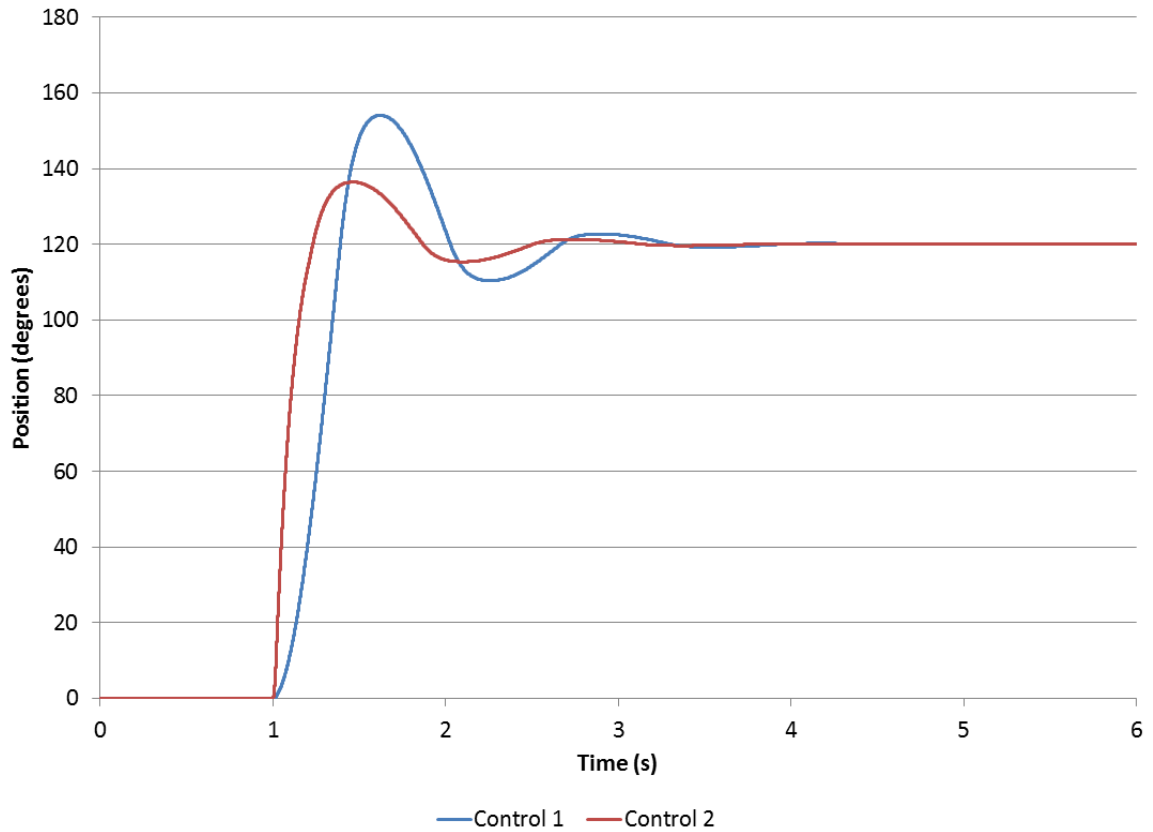
**Figure 11: Comparison of two damper control strategies for  $b = 10$**

Using the lowest damping rate, there isn't much difference between the two control schemes. There is a slight improvement in the crossing time and overshoot, but not enough to justify the increased complexity of the second control scheme. There is also negligible difference in settling time.



**Figure 12: Comparison of two damper control strategies for  $b = 20$**

With increased damping, the difference between the control schemes is becoming increasingly pronounced. The crossing time and overshoot show greater improvement. The effect on settling time is still very small however.



**Figure 13: Comparison of two damper control strategies for  $b = 50$**

The higher damping rate now shows a significant improvement in the crossing time, overshoot and settling time. This trend continues in the next two tests as well.

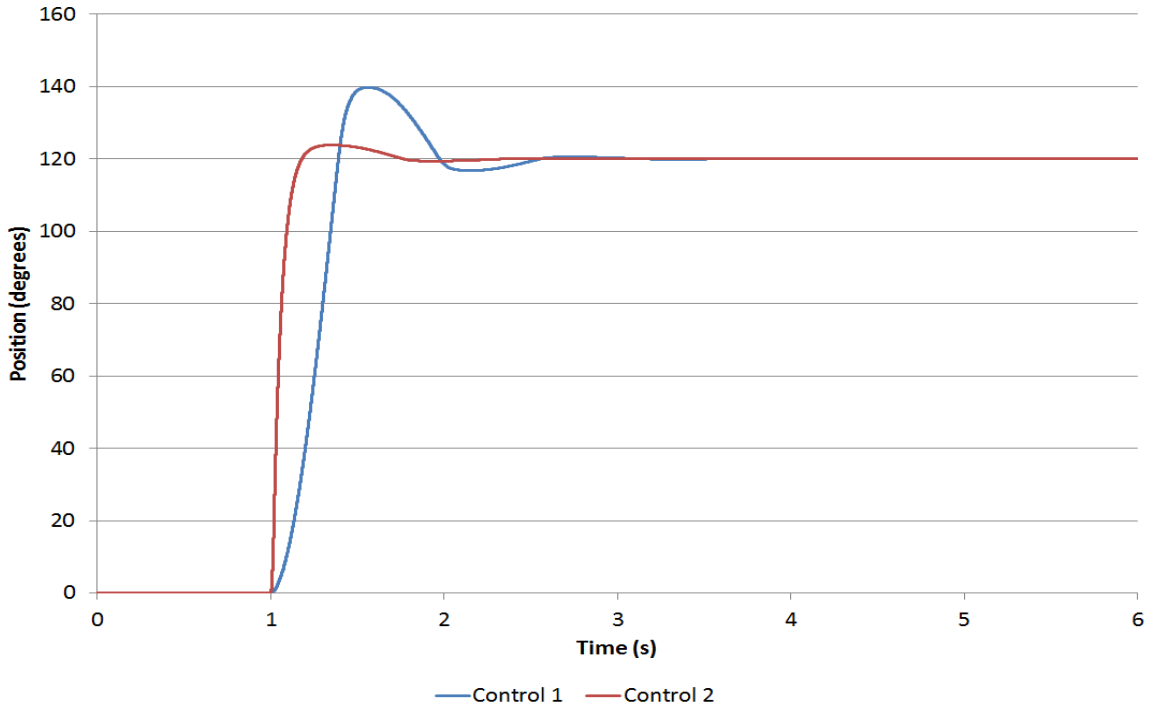


Figure 14: Comparison of two damper control strategies for  $b = 100$

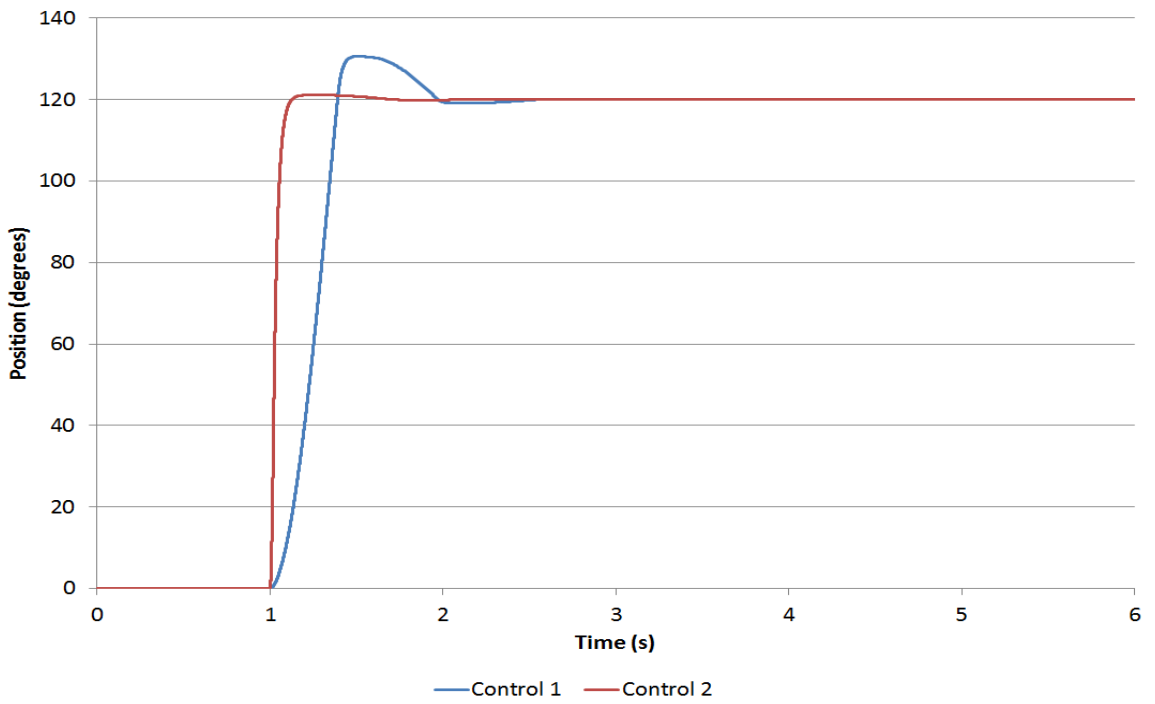


Figure 15: Comparison of two damper control strategies for  $b = 200$

At this high damping rate, the system almost behaves like a zero order system. The crossing time has been greatly reduced, and the overshoot is almost nonexistent. However, comparing the response between Figure 14, and Figure 15 shows that the system behaves almost the same at only half the damping rate.

These tests demonstrate that when using a lower damping rate, the more complex damper control scheme doesn't have much effect on the response. Increasing the damping rate will bring better improvements to a point, after which the improvements start diminishing again.

## Chapter 3

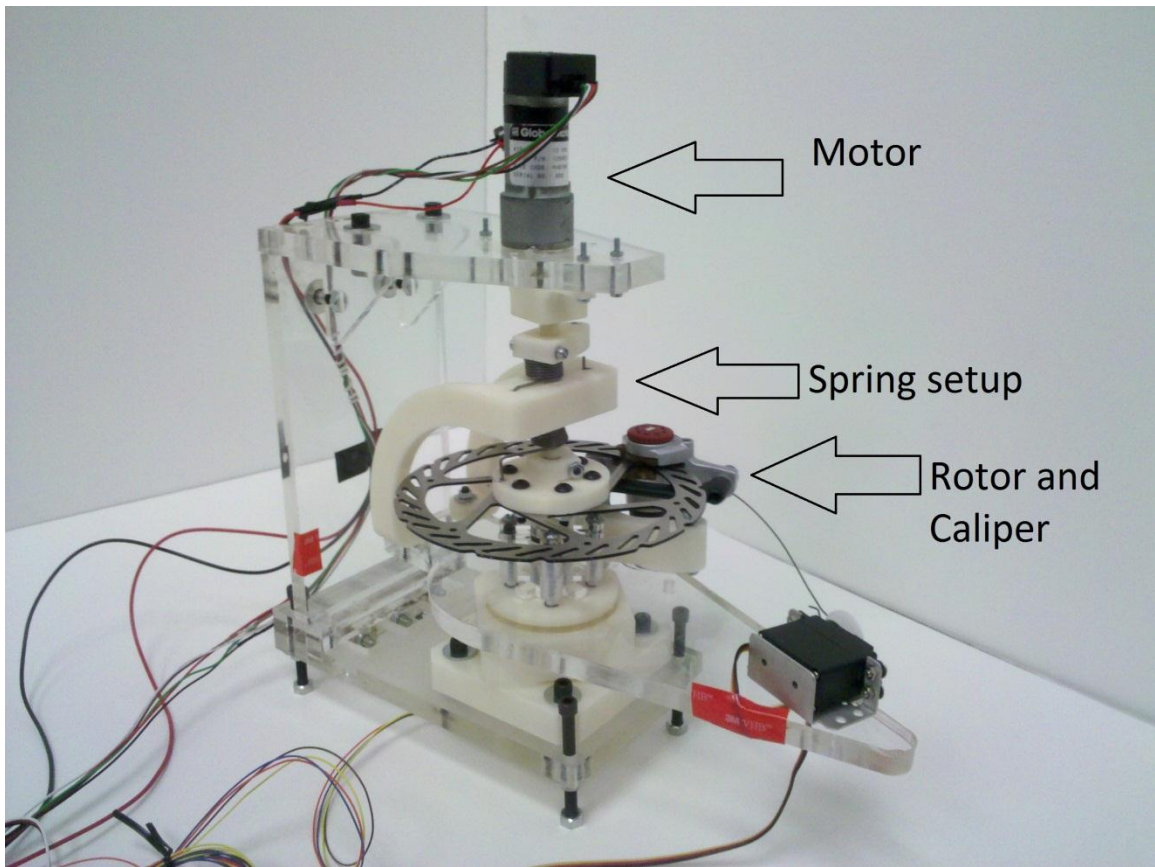
### Experimental Validation

A suitable variable damper for use in a precise and compliant actuator is an MR damper. However, a prototype MR based SEA-CD would be expensive, and a more reasonable priced alternative would be tested first, to see if the variable damper idea had any merit. The primary cost in the MR damper is the MR fluid itself, which is only sold in bulk. The volume of MR fluid used in each damper is quite small however, so the cost of the MR fluid per device is low.

As a substitute for the MR damper, a disk brake type rotor-caliper setup was used. The rotor-caliper can vary its damping torque by adjusting the normal force the brake pads exert on the rotor. The caliper used for the physical model has a spring loaded lever



that controls the normal force the pads apply on the rotor. Compared to a MR damper, the rotor-caliper has similar responses in most areas, and similar nonlinearities, but the rotor-caliper is more difficult to align and mount, takes more space than a comparable MR damper, and its modulation speed and range is dictated by the device actuating the caliper. The assembled test bed is shown in Figure 16.

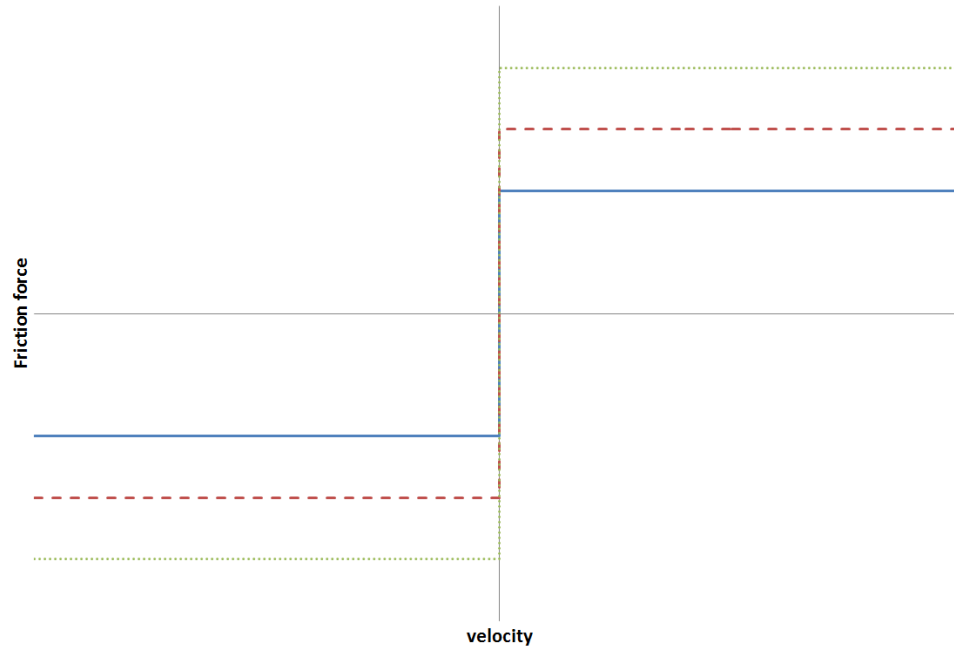


**Figure 16: The entire test bed**

### **3.1 Rotor-Caliper Validation**

To validate the rotor-caliper setup, the behavior of each system is checked in the two operating regimes of concern. Namely their behavior in the static and dynamic regions is compared. Please note that the following four figures (Figure 17, Figure 18, Figure 19, and Figure 20) are not to scale, and are merely meant to demonstrate the

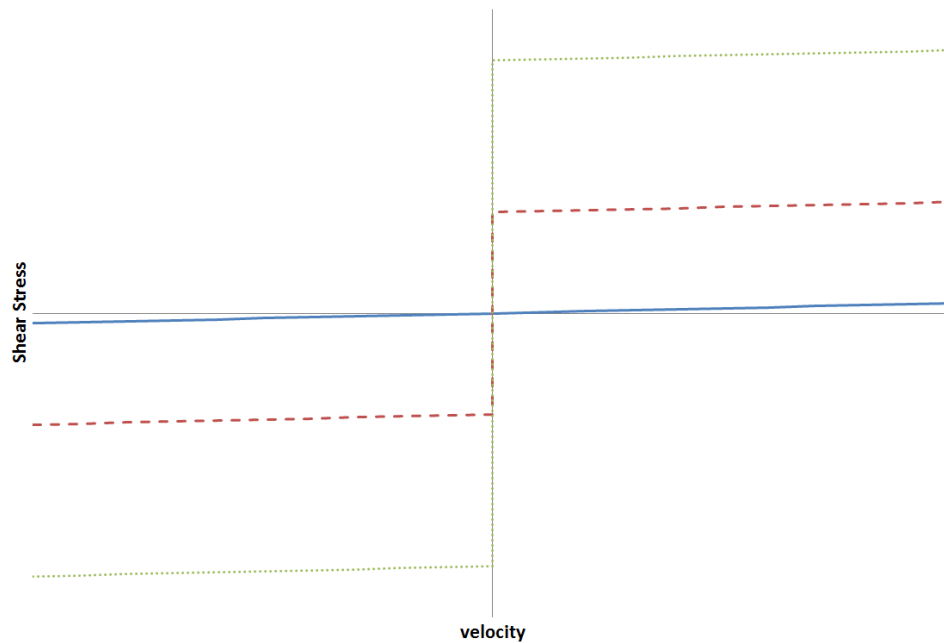
differences between a rotor-caliper type variable damper and an MR fluid based variable damper.



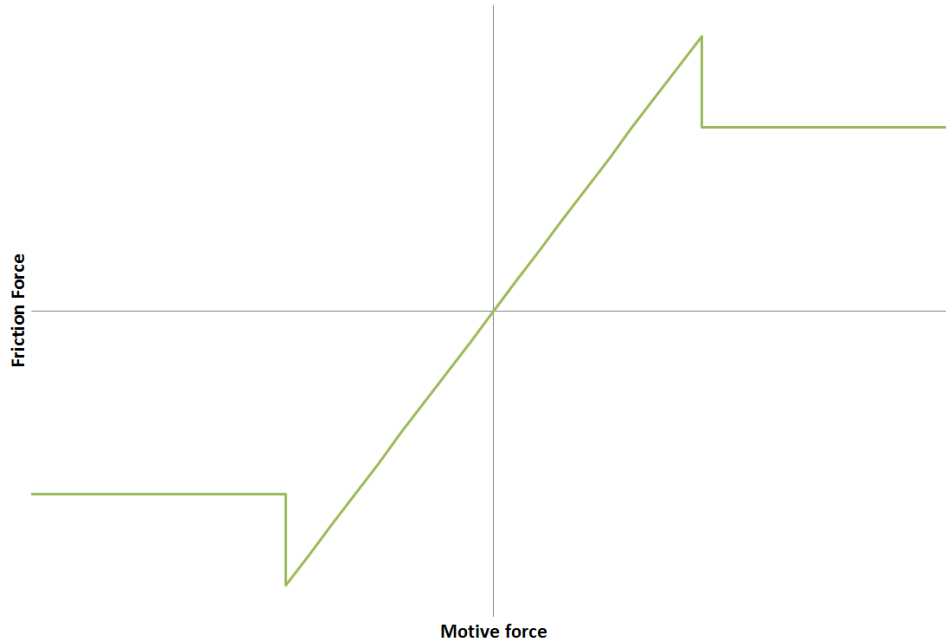
**Figure 17: Friction force vs. velocity in a caliper at different normal forces on the caliper. Higher damping force magnitude corresponds to higher normal forces.**

Figure 17 shows the damping force generated by the brake pads vs. the velocity of the rotor at different normal forces on the caliper. The rotor cannot move until the static braking force is overcome, at which point, the rotor begins moving, and the brake pads produce a constant damping force. The force applied by the brake pads depends only on the normal force acting on the brake pads. Increasing the normal force means a higher motive force is required to move, and the pads supply a higher damping force.

Compare this behavior to the Shear stress vs. velocity graph of a MR damper. When no magnetic field is present, the system behaves like a fluid damper using a newtonian fluid. Higher relative motion between the plates leads to higher shear stress, and therefore higher damping. This corresponds to the blue line in Figure 18. Once a magnetic field is applied, however, the fluid begins behaving like a Bingham plastic [30]. The output cannot move until the motive force reaches a certain threshold, the yield stress which is dependent on the magnetic field. Upon reaching the yield stress, the MR fluid behaves like a fluid, but with an offset corresponding to the yield stress.



**Figure 18: Shear stress vs. Velocity in a MR damper. Higher stress magnitudes correspond to higher magnetic fields.**

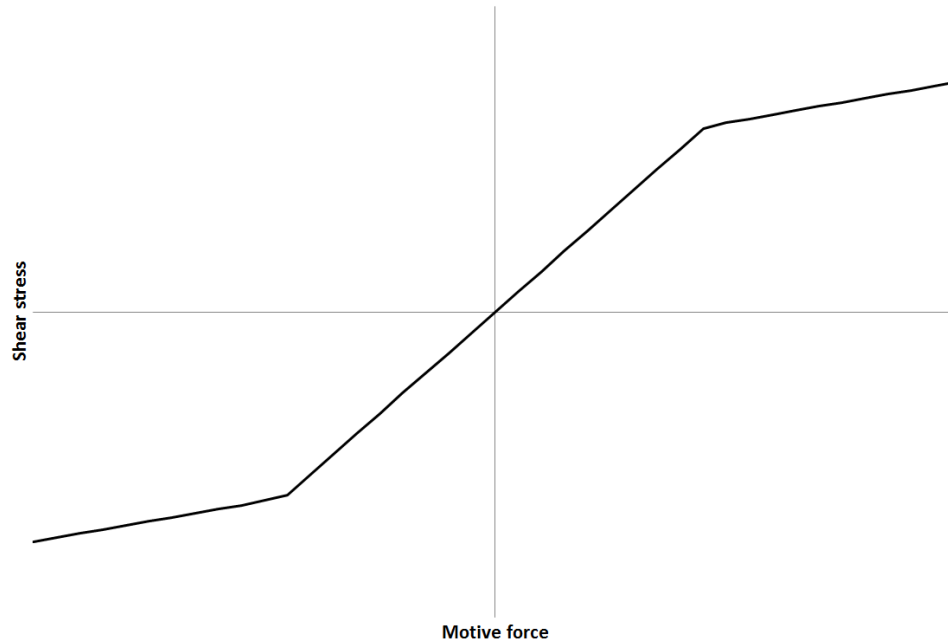


**Figure 19: Motive force vs. Friction force in a rotor-caliper**

Figure 19 is a diagram of the motive force vs. the damping force generated by a rotor-caliper setup, under a constant normal force. The damping force exactly matches the motive force to a set point, as predicted by coulomb friction using,

$$F_{fr} \leq \mu_s F_n$$

Where  $F_{fr}$  is the friction force,  $\mu_s$  is the coefficient of static friction, and  $F_n$  is the normal force. When the motive force exceeds the maximum static friction, the rotor-caliper setup enters the dynamic friction zone, and provides a constant damping force regardless of the motive force. Compare this to the same diagram for a MR fluid damper at a constant magnetic field strength. Until the threshold is reached, the damper provides exactly enough force to counter the motive force. When the motive force exceeds the threshold, the damping depends on the velocity.



**Figure 20: Shear stress vs. Motive Force in a MR damper**

The rotor-caliper and MR damper behave similar enough in the static and dynamic region that one can be made to look like the other. The normal force on the rotor-caliper can be modulated so that the damping force increases at higher velocities, like an MR damper, and the magnetic field in a MR damper can be modulated to get a flat damping rate independent of the velocity. The transition between the two static and dynamic zones, however, is very different between the two systems.

The force plot is discontinuous at the transition point for the rotor-caliper where the magnitude of the damping force jumps to a lower value. In the case of the MR damper, only the derivative of the damping force with respect to the motive force changes to a new value. While this discrepancy is somewhat mitigated when considering that over the entire motion, the system has very few points when the damper switches between the

static and dynamic regions, the joint response when using a rotor-caliper type variable damper will be slightly different from the joint response when using a MR fluid based variable damper.

It should be noted, however, that neither the rotor-caliper based variable damper, or the MR fluid based variable damper follow the damping behavior of the variable damper used in the simulations in Chapter 2. The simulations in Chapter 2 are quick studies into whether or not a hypothetical variable damper can theoretically improve the response of an SEA. The physical model is not meant to be compared to the simulations in Chapter 2.

### 3.2 Design and Manufacturing

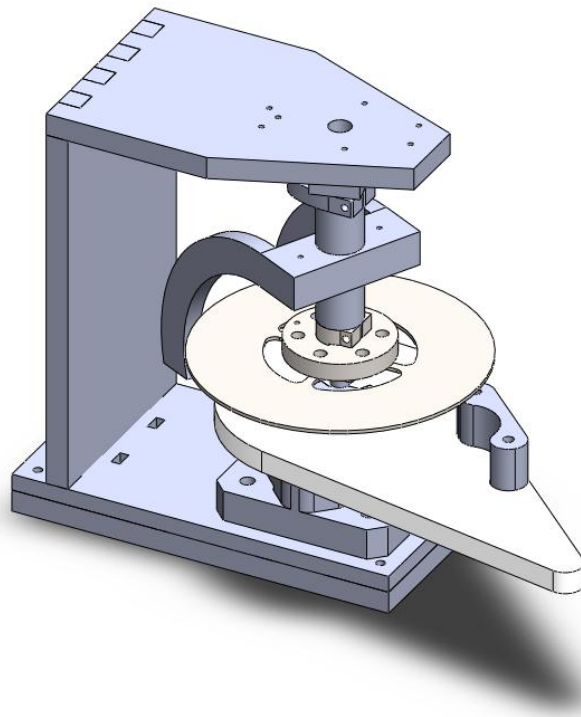
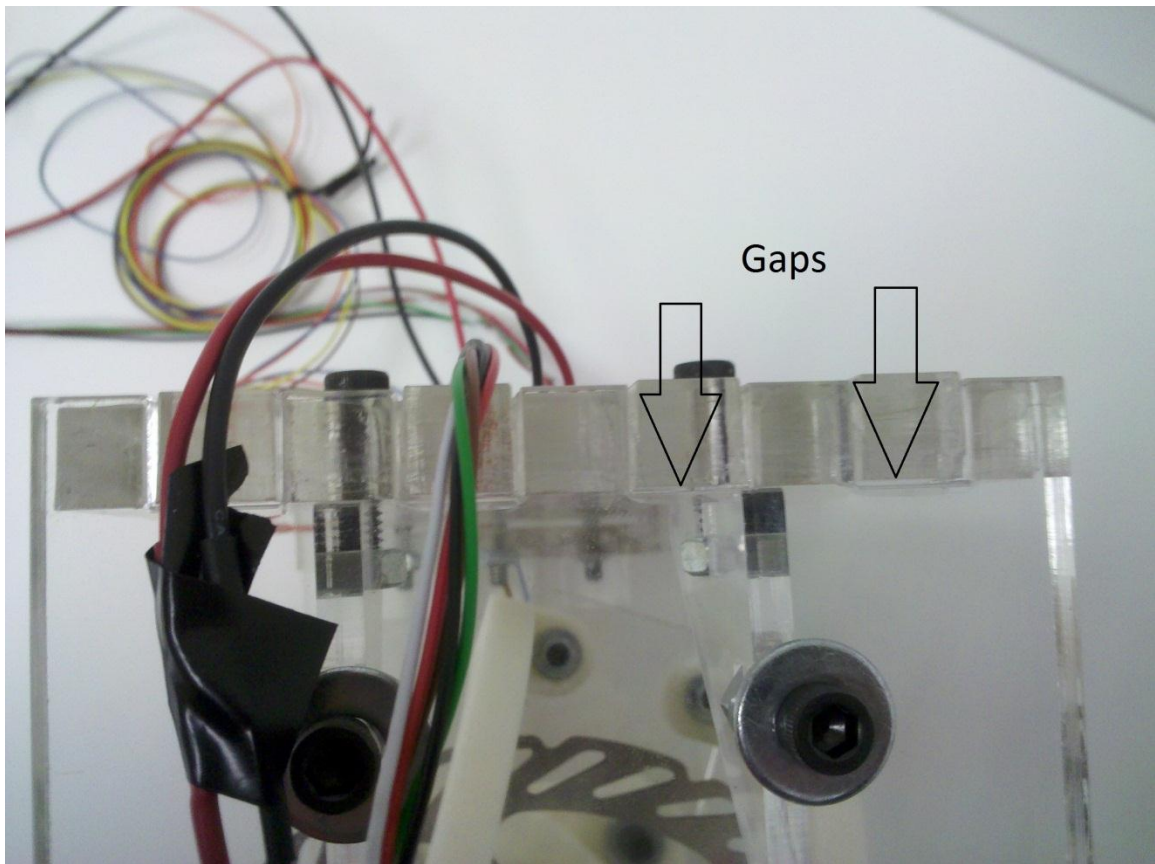


Figure 21: SolidWorks Model of the Test Bed

The test bed was first designed in SolidWorks, as shown in Figure 21, and key parts were tested using the inbuilt finite element analysis to ensure the part would not yield. Since the test bed is made to prove the concept, rather than demonstrate a prototype, it is made primarily from plastic to reduce costs. Large parts were remade into pieces that could be made on a 2D laser cutter. The smaller pieces were made using a Rapid Prototyping Machine.



**Figure 22: Image of the error from the laser cutter cutting too thick of a plastic. The square edges should be flush.**

Many of the parts are laser cut, but the thickness of the plastic load bearing elements meant the laser cutter could not make straight cuts into the plastic. Figure 22 shows an example of this. The teeth were designed to lie flush against each other, but the

errors in cutting caused introduced the gaps seen in the figure. This created some errors in alignment, which increased the friction between some sliding surfaces. The RPM pieces are also quite soft, and repeated testing caused some interfaces to deform. Most notably, the interface between the RPM shaft the springs and rotor are clamped to, and the motor deformed to the point where either the motor or the shaft could move by  $2^0$  without affecting the other. This degree of slack was measured by moving the rotor and checking the motor position

### 3.3 Compliance

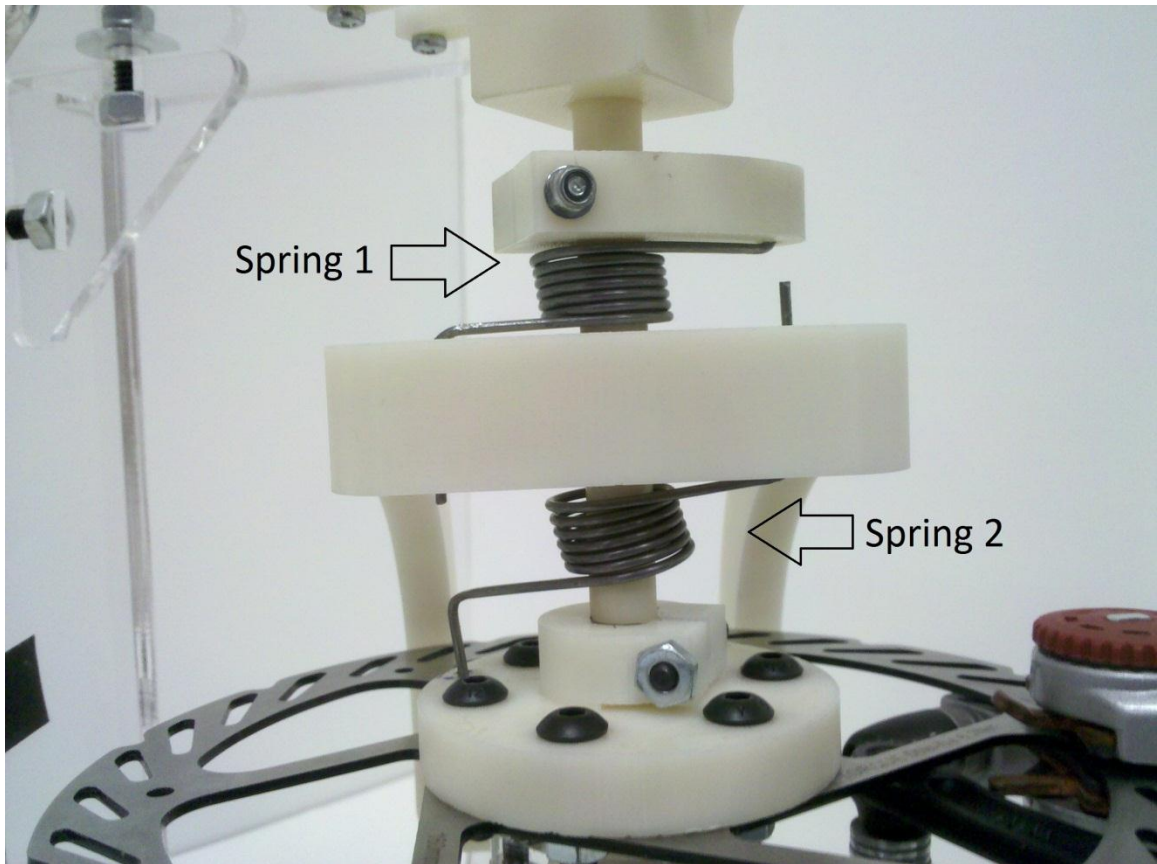


Figure 23: The antagonistic spring setup



To keep the system inexpensive, simple, wound music wire torsional springs are used, as shown in Figure 23. The two springs are mounted in an antagonistic fashion, and are pre compressed to half their useable range so that the springs remain in compressed range even when moving counter to the direction of compression. This also gives the spring setup a linear spring rate, and eliminates any slack in the spring subsection.

### 3.4 Components

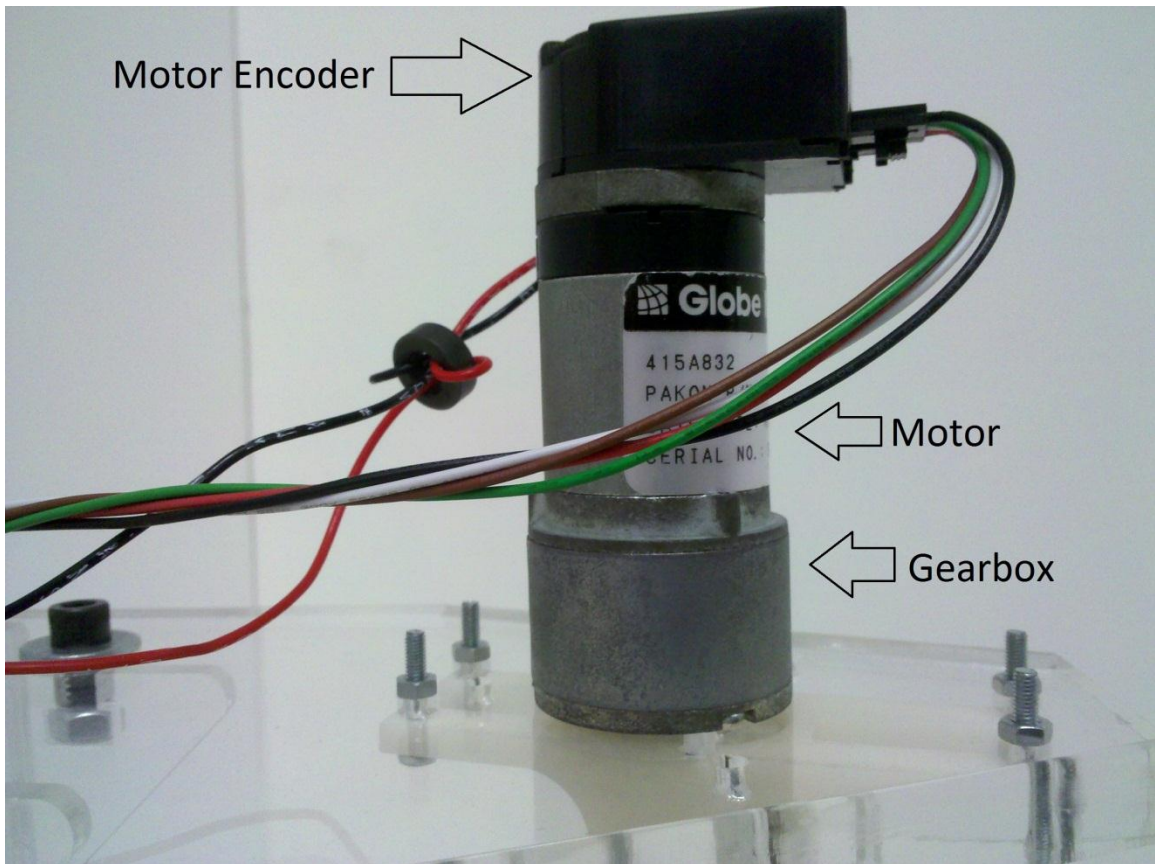
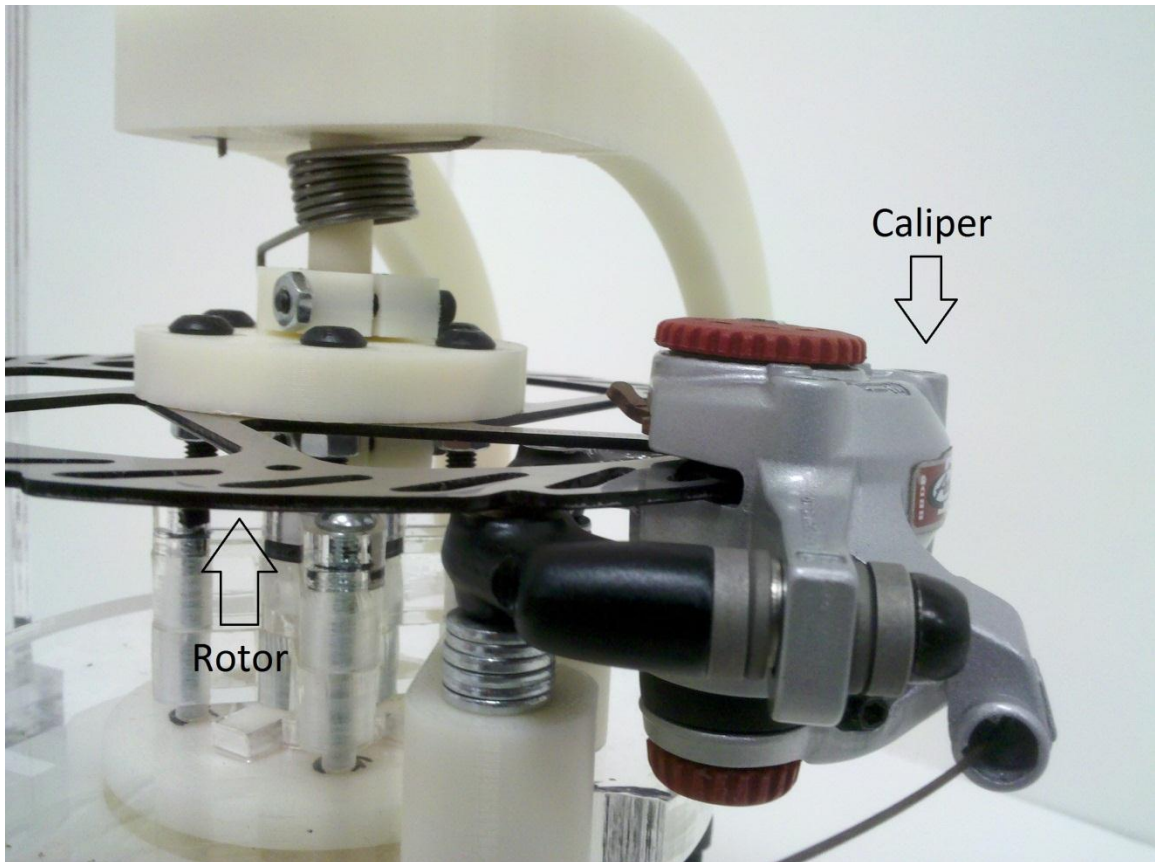


Figure 24: The motor, gearbox and encoder

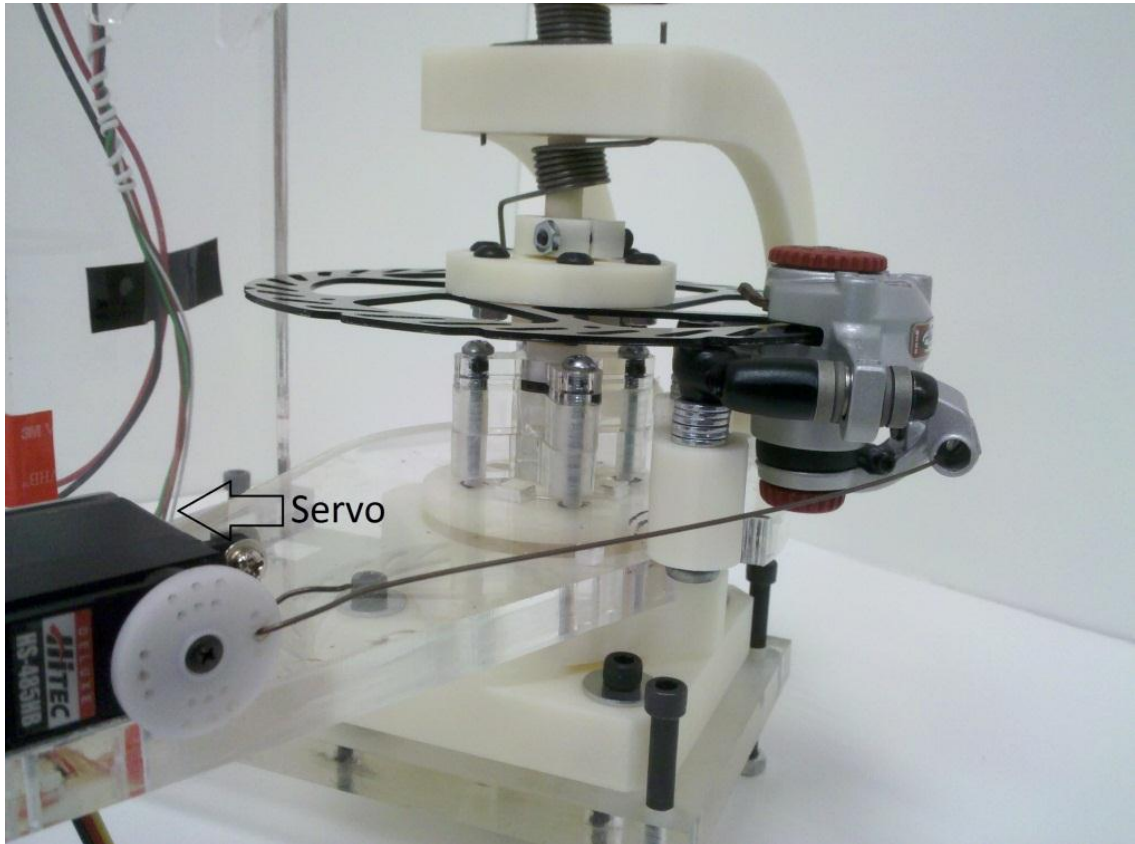
The system uses a Globe motors 415A832 12 V dc motor [31] with a built in encoder (As shown in Figure 24), and an s4 360-250-B-D US digital encoder [32] for the arm (Figure 27). The motor encoder has a  $0.18^\circ$  resolution and the arm encoder has a  $0.25^\circ$  resolution. The brake rotor and caliper are Avid 160 mm rotors with a BBDB caliper [33] (Figure 25) which is actuated by a Hitec HS-485HB servo [34] by means of a steel cable. The steel cable had a kink in it to hook into the servo horn, as shown in Figure 26, and the other end was clamped in the caliper (Figure 25). The spec sheets for the motor, arm encoder and servo are listed in Appendix B.



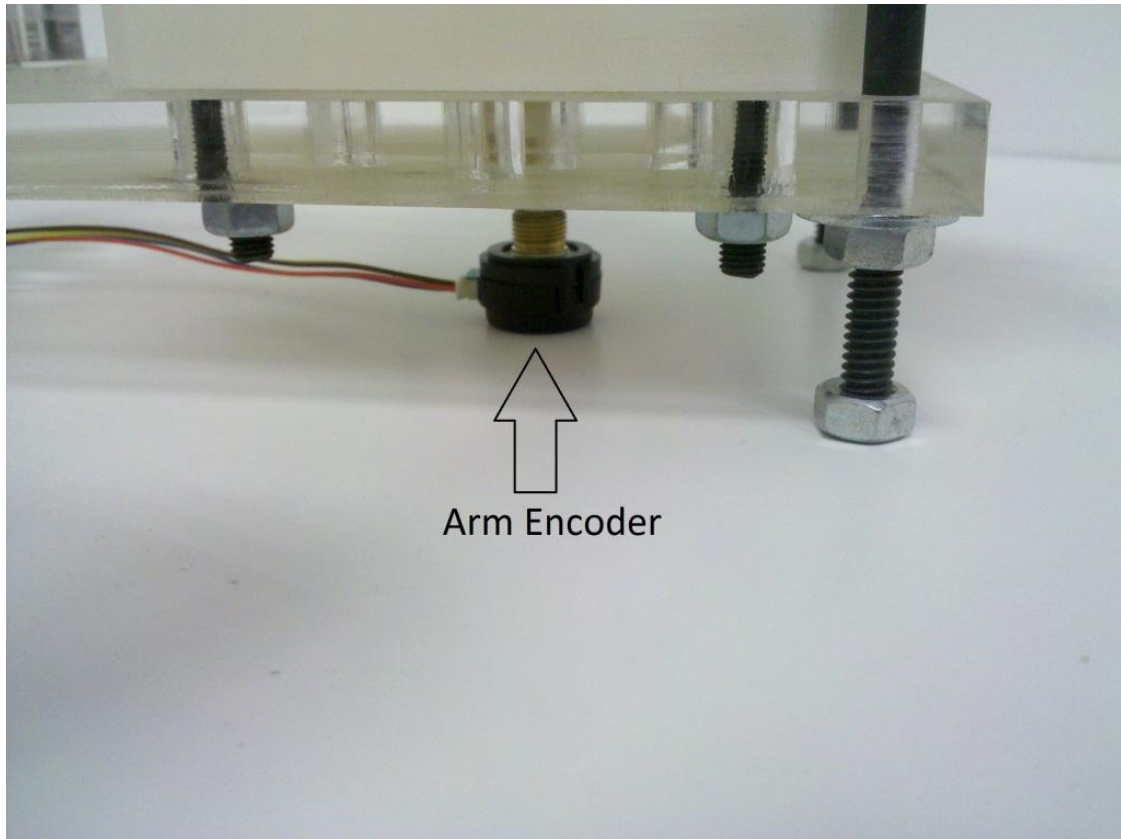
**Figure 25: Image of the rotor-caliper setup**

Since the caliper is meant to work with cable brakes in bicycles, it had a jaw and a screw that could be tightened to secure the cable in place. This end was adjusted so that

the caliper was fully closed when the servo was fully closed, in order to prevent breakage from the servo pulling too hard on the cable. The servo itself was secured to a metal bracket which in turn was secured to the arm.



**Figure 26: Image of the servo connected to the rotor-caliper setup**

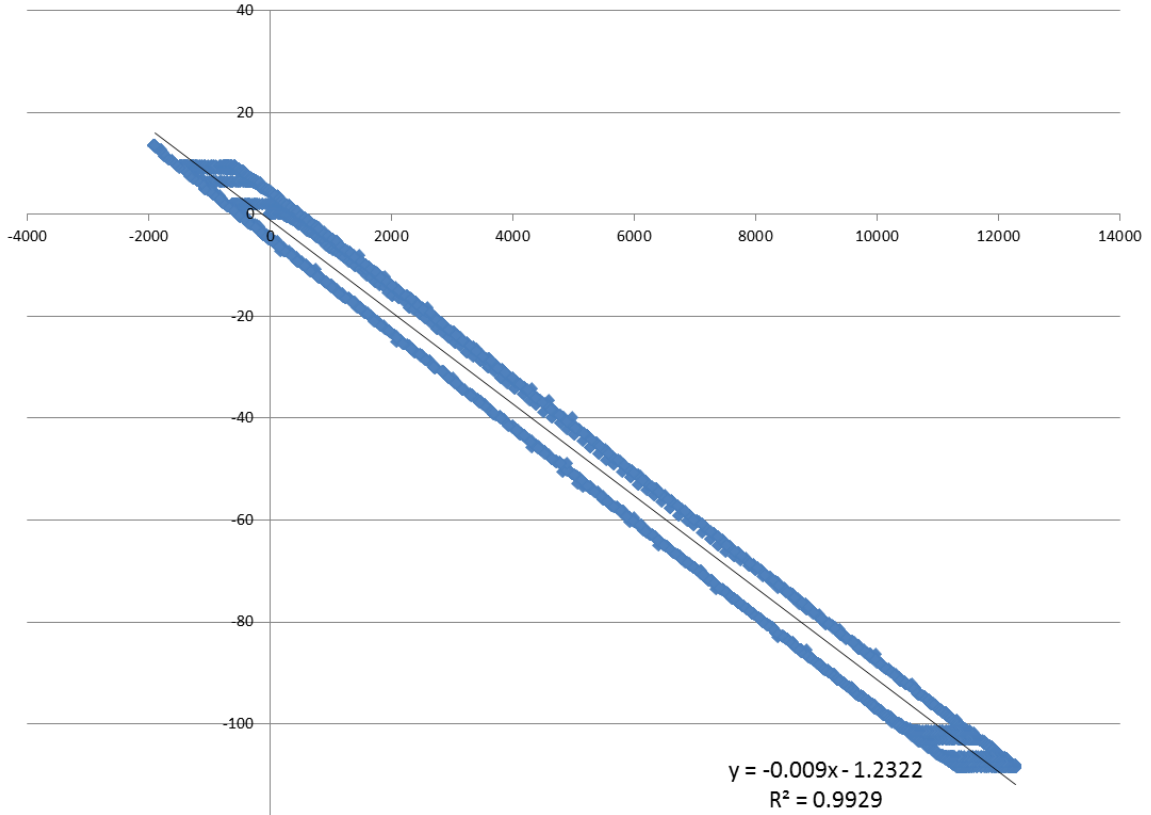


**Figure 27: The US Digital encoder connected to the arm**

### **3.5 Control**

In order to control the motor, servo, and gather data from the encoders, Phidgets USB boards [35] are used. These were chosen for their ease of use, and high data collection rate. The Phidgets boards are controlled using a LabVIEW VI [36]. Interfacing with the Phidgets boards was handled from within the LabVIEW VI using the API provided by Phidgets. Before starting the test, the arm is moved so it points straight forward and the encoders are zeroed to the position. Since the arm is only performing a  $120^\circ$  sweep, there is no need for exact zeroing.

Unfortunately, the datasheet for motor had the wrong gearbox value. The data sheet for the encoder states that it is 500 counts per revolution encoder, but without the gearbox reduction, the encoder counts per revolution of the gearbox output shaft was unable to be determined. A workaround was devised where the servo locked the input and output shafts, and the arm was moved around. Since the arm encoder reported the position of the arm in degrees, and the motor and arm were locked together, the arm position must correspond to the motor position. A motor was given a sinusoid signal, and the resulting motor encoder counts and arm encoder counts were recorded. This data was plotted in excel, and using Excels inbuilt linear regression tool, an equation to relate motor encoder counts to degrees was found, as shown in Figure 28. The hysteresis is due to the slop between the gearbox output shaft, and the RPM shaft with the springs and rotor.



**Figure 28: Motor encoder calibration**

Another limitation discovered during testing is the servo response time. The servo takes .2s to travel 60°, which is approximately the degree of travel between just open, and fully clamped. This complicated the tests, since the .2s delay means the arm has moved well past the motor position before the high damping activates. An unexpected side effect of this delay portrayed the destabilization of the system with improper damping actuation. The damper would engage at the point of maximum overshoot, release, then engage at maximum overshoot in the other direction; doing this repeatedly to incite resonance. The magnitude of the maximum overshoot was bounded, but the system was not settling to a point. To prevent this from happening, the gains of the PID loop

(explained in the next section) were adjusted. Specifically, the  $k_i$  gain was reduced till this phenomenon could not be recreated.

Preliminary testing showed that the motor used to drive the system was too easily back driven to give a step input to the system. Therefore, a PID control loop was used to control the position of the arm. The output from the PID is the direction and duty cycle with which to drive the motor. The PID loop is a simple sub VI that accepts the current position error from the main VI. It then stores this value as the previous error for use in the next time step. The integral of the error is calculated by taking the current error, multiplying it by the time step (.005 s), and adding it to a running sum of the error. The derivative of the error is calculated by taking the current error, subtracting the previous error, and dividing by the time step (.005s). Each of these values, the position error, integral of the error, and derivative of the error is multiplied by a unique gain. The gains were tuned with the servo holding the caliper open to prevent interference. They were first tuned to elicit an under damped response from the arm. After noting the resonance behavior from the first set of gains,  $k_i$  was lowered to prevent the above noted behavior. In doing so, the system no longer settles to zero quickly, but since the thesis is not concerned with optimal control, this tradeoff was deemed acceptable. The output from the PID is a percentage of the full speed the motor should be driven at. This output would regularly exceed 100%, especially just after the step, so a saturating function was placed that would replace any value above 100% with 100%, and any value below -100% with -100%.

Table 4: PID gains

Gain	Value
$k_p$	2.5
$k_i$	0.01
$k_d$	2.0

At the start of the program, the Phidgets API was called to initialize each board, and open the servos, encoders, and motor to receive commands, set the encoders to zero at their current position, set the maximum motor acceleration, and set the servo type. The servo settings include values such as the maximum speed the servo can achieve, the range of PID signals accepted as valid position commands, etc. The API includes the standard servo settings for the Hitec servo, so these settings were used to control the servo. The timer is also started at this point. The main portion of the program is contained within a while loop that terminates when a stop button on the front panel is pressed.

The while loop is divided into three sections. The first section reads the current position from both encoders, and converts the reading from counts to degrees. After this, two errors are calculated. One is the error between the arm position and the commanded position, which is passed to the PID loop, and the other is the error between the arm position and the motor position, which is passed to the servo control loop. The next section calculates the output from the PID loop and the servo control.

The servo control is another sub VI that accepts the current error between the arm and motor, and the type of actuator being tested. Type 1 is a standard SEA, and the servo



is commanded to fully open the caliper. Type 2 is a rigid joint, and the servo is commanded to clamp the caliper to the rotor with maximum force. Type 3 is the SEA-CD being tested, and the servo is commanded to start at a position where the calipers are barely touching the rotor. The servo is then commanded to close the caliper for .4 s when the arm-motor error crosses zero. The output from the servo control is a position the servo should move to.

The last section of the main program sends the PID output to the Phidgets motor control board, and the servo control output to the Phidgets servo control board. It also assembles the time and position data, and prints it to a text file in a tab delineated format. Once the stop button on the front panel is pressed, the program stops execution of the while loop, sets the motor speed to 0, the servo to open, and finally frees up the Phidgets control boards.

### 3.6 Testing

Testing consists of giving the arm a step input to move  $120^\circ$ , and recording the position of the motor and arm at 5 ms increments. The PID control for the motor is reset between tests, but the gains are left unchanged. There are 3 basic situations to test.

***No damping:*** This replicates the behavior of the joint, if it were a standard series elastic actuator. This test gives us a baseline with which to compare future tests.

***High damping:*** This replicates the behavior of the joint, if it were a traditional, stiff joint. This gives the best possible dynamic behavior of the system.

*Variable damping:* The results from this test will provide a comparison between the prototype to the baseline and best case scenario. Unfortunately, the alternative control strategy discussed in section 2.3 cannot be implemented here, since it requires a damper that can modulate orders of magnitude faster than the servo can provide.

Each test case was repeated 4 times for a total of 5 sets of data per test case. The first test is the joint response if it was a traditional stiff joint. The second test is the joint response if it is a SEA. The third test is the joint response as a precise and compliant actuator.

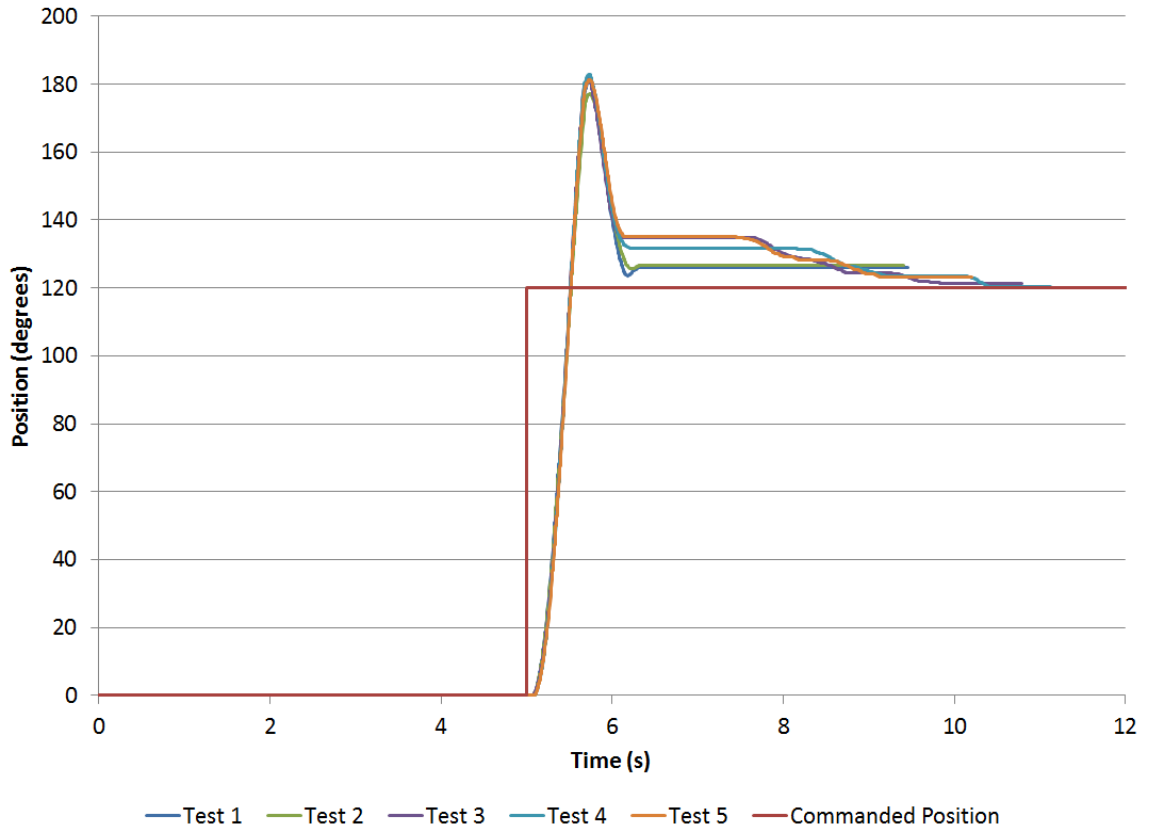
# Chapter 4

## Results

The following sections present the results from the three test scenarios. Section 4 shows the result from the arm if it were a stiff joint. Section 4.2 presents the results from the arm as if it were a SEA. Section 4.3 presents the response with the joint using controllable damping.

There are two main criteria used to compare the dynamic behavior of the different cases: the maximum overshoot, and the ringing time. The maximum overshoot is the maximum distance between the arm and motor position, and always occurs right after the first time the arm position crosses the motor position. The ringing time is the time taken before the system stops oscillating. In all the results, there is a distinct point in time when the response stops looking like a harmonic response, and asymptotically converges to the commanded position.

## 4.1 Stiff Joint Case



**Figure 29: Result for the stiff case**

This test demonstrates the best possible outcome. The maximum overshoot is around  $180^\circ$  and the system quickly stops ringing, and starts approaching the commanded position.

## 4.2 Series Elastic Actuator Case

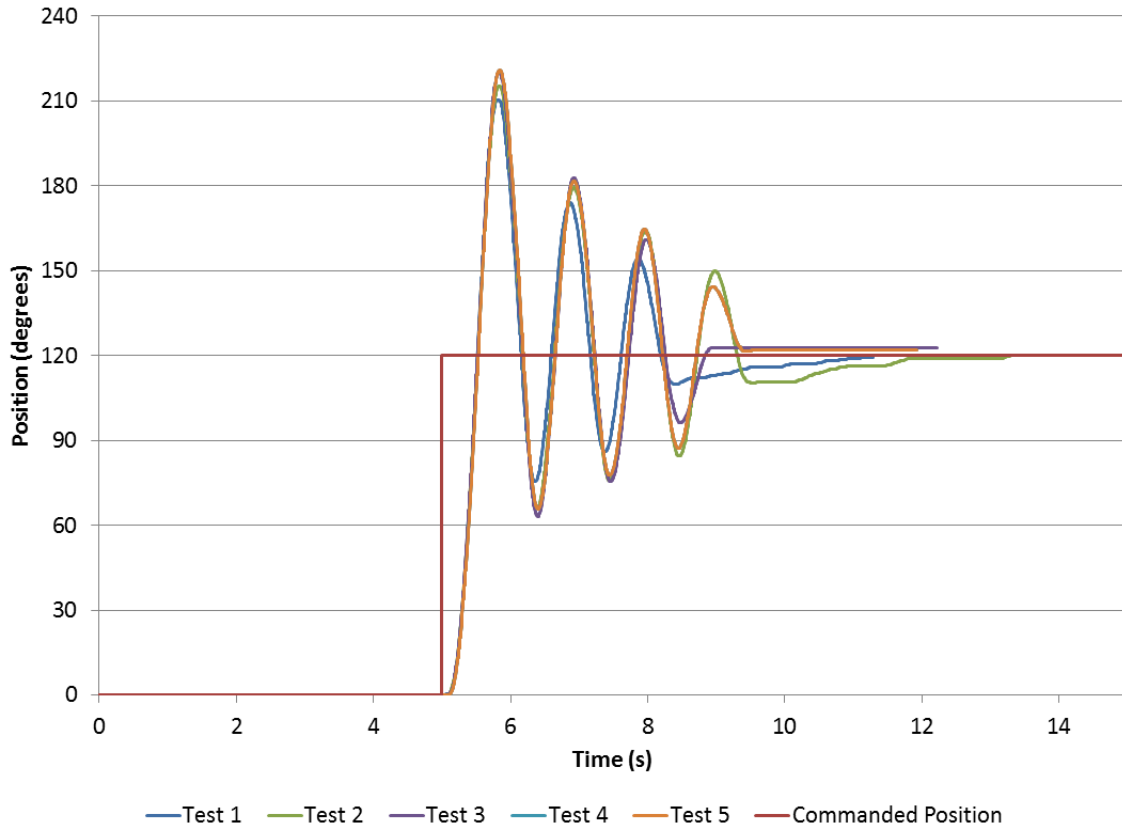


Figure 30: Result from the Undamped Case

The SEA case reflects what is expected from an under damped second order system. What is interesting however, is the effect of slack in the system. In Test 1 and 3, the system stopped oscillating after 3 oscillations, whereas in the other tests, the system took 4 oscillations to stop oscillating. Figure 31 and Figure 32 show the results from test 1, where the system stopped oscillating after three time periods. Figure 33 and Figure 34 show the results from test 2, where the system took four time periods to stop oscillating. The rest of the test results are in Appendix C. The arm-motor error graphs below show the same result, with the average maximum arm-motor error being about  $65^\circ$ . Also note

that the maximum overshoot is the first positive spike on the arm-motor error graphs. The initial negative spike is due to the motor leading the arm, which is expected since the motor needs to compress the springs before the springs generate enough force to move the arm.

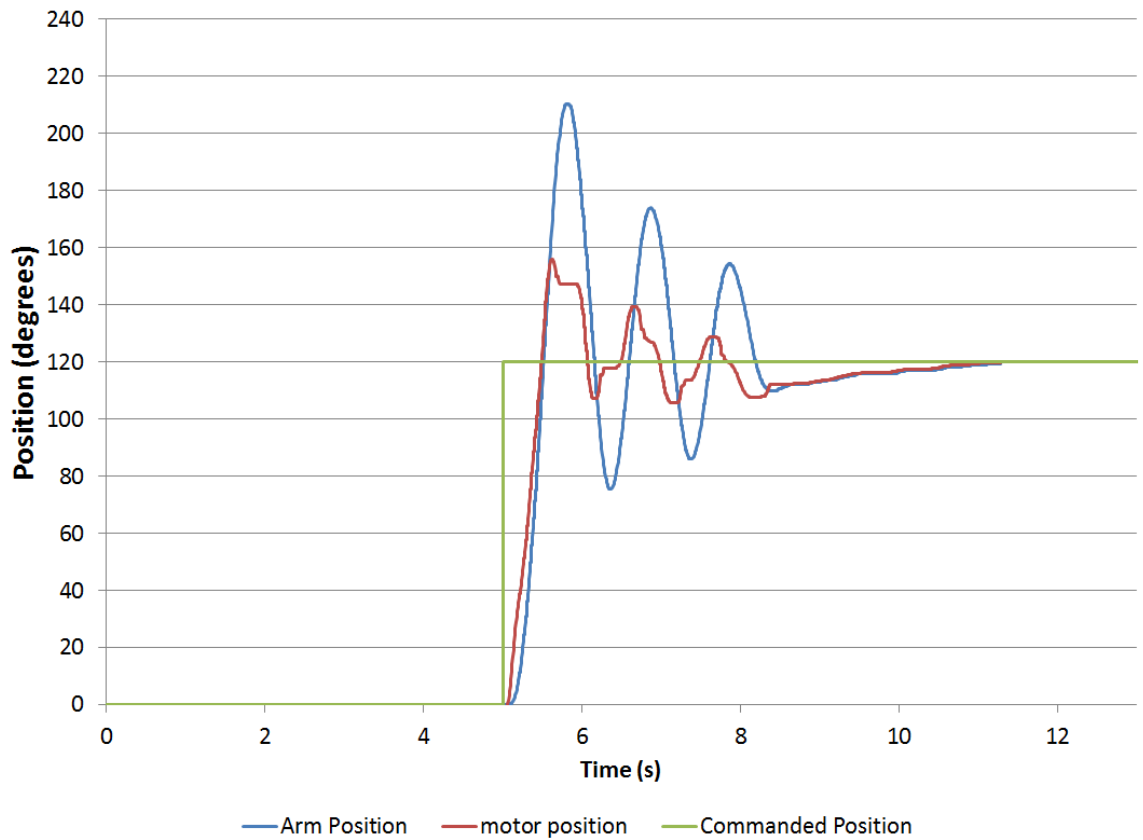


Figure 31: Test 1: Arm and Motor response

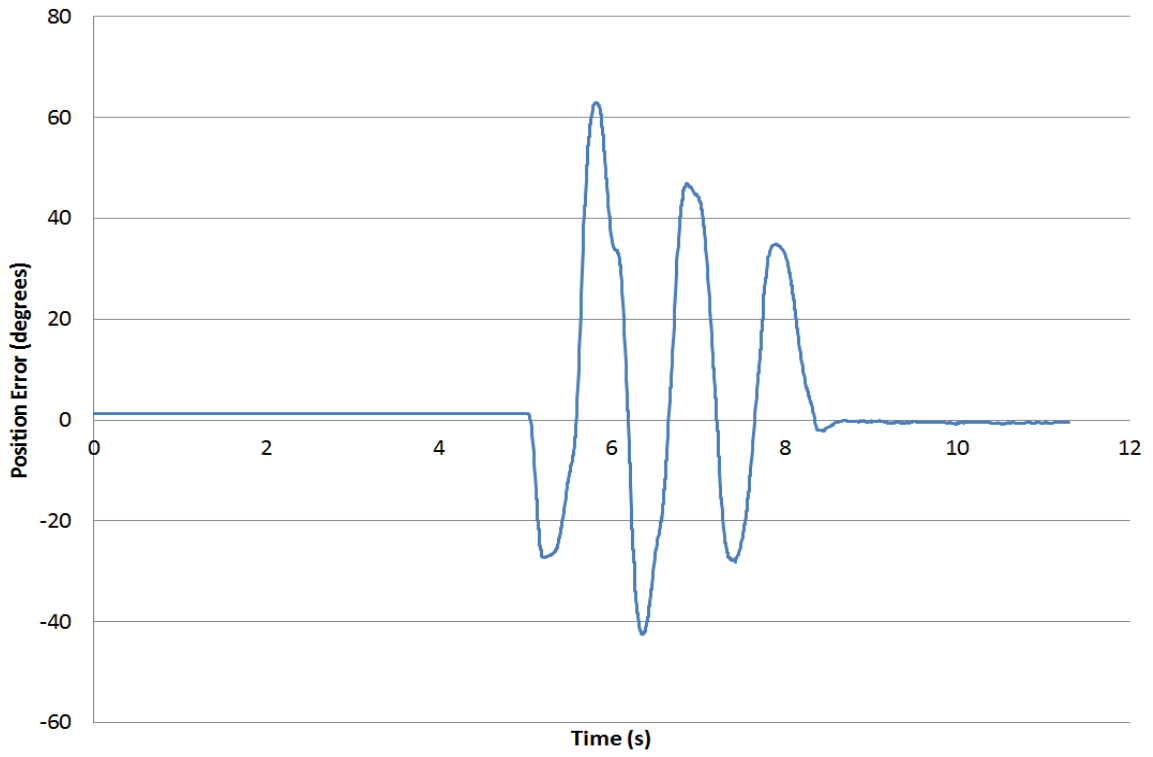


Figure 32: Test 1: Arm-Motor error

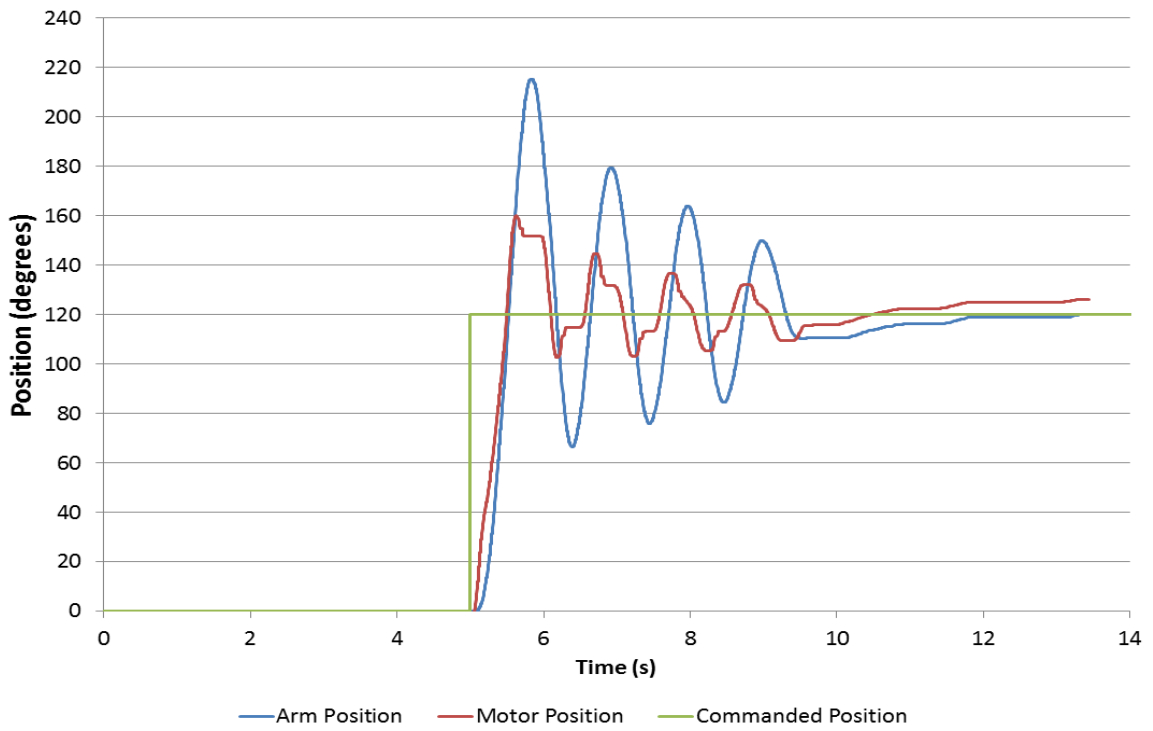
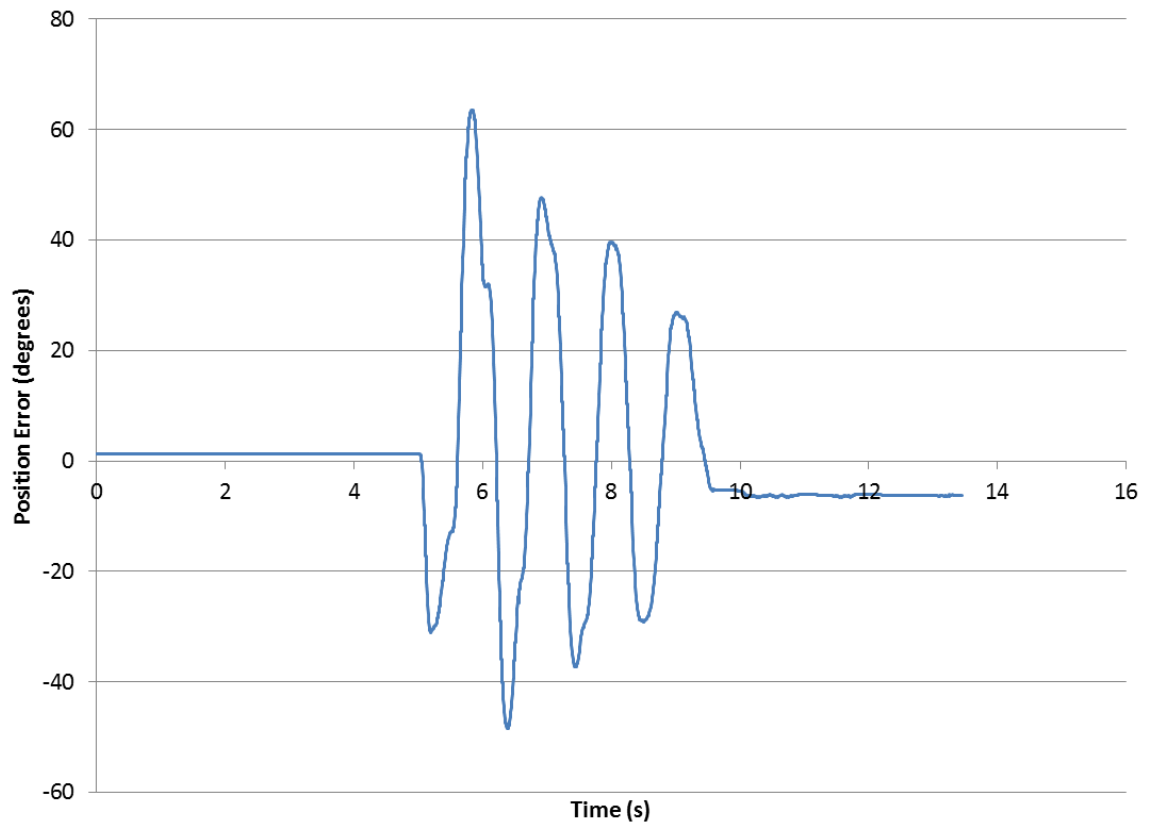


Figure 33: Test 2: Arm and Motor response



**Figure 34: Test 2: Arm-motor error**



### 4.3 Series Elastic Actuator with Controllable Damping Case

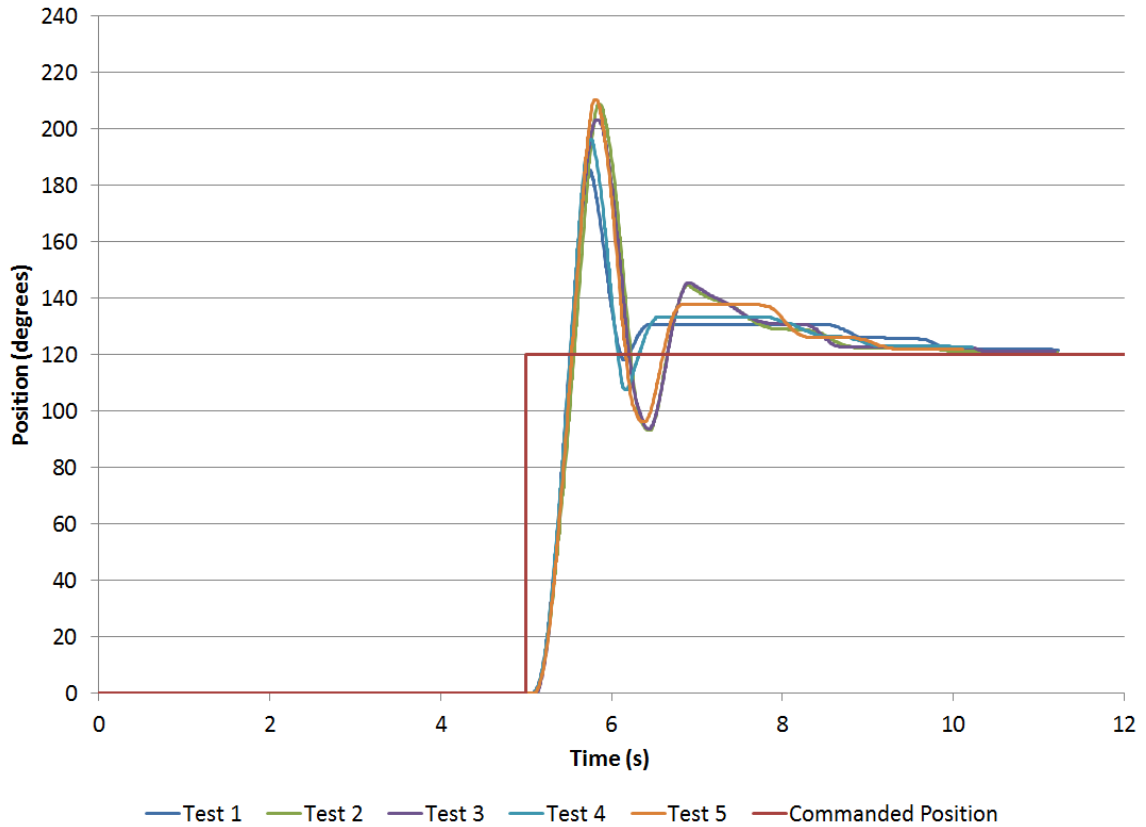
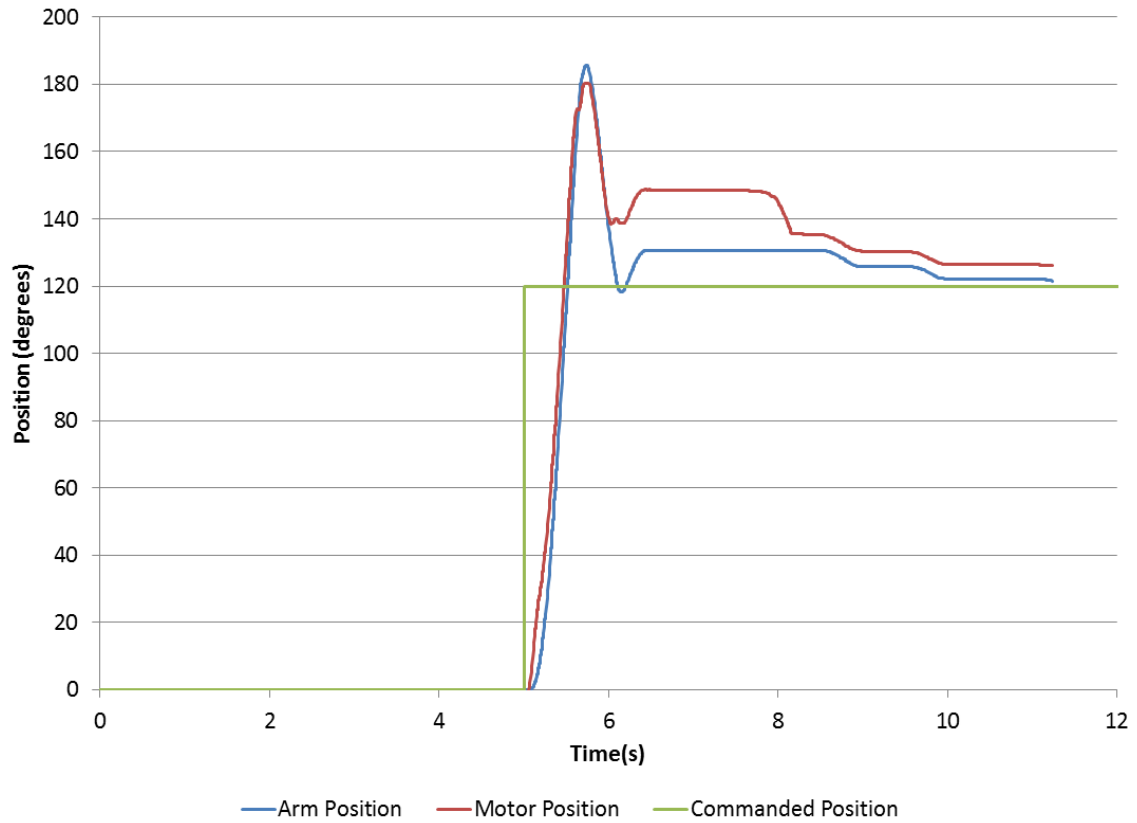


Figure 35: Controllably damped case

Figure 35 shows that the precise and compliant joint has a similar response to the traditional stiff joint. There is only one oscillation before the system goes to the commanded position, instead of three as in the undamped cases. While the maximum overshoot is not affected a great amount due to the caliper actuation delay because of the servo, the ringing time was cut by a third. In all cases except the first one, the maximum overshoot was around  $40^\circ$ .

Test 1 (Figure 36 and Figure 37) show the best case scenario. Normally it would have been discarded as an outlier, but it was included to demonstrate how a MR damper

would respond. Test 3 (Figure 38 and Figure 39) shows the typical response of the precise and compliant actuator. The rest of the tests are in Appendix D.



**Figure 36: Test 1: Arm and Motor response**

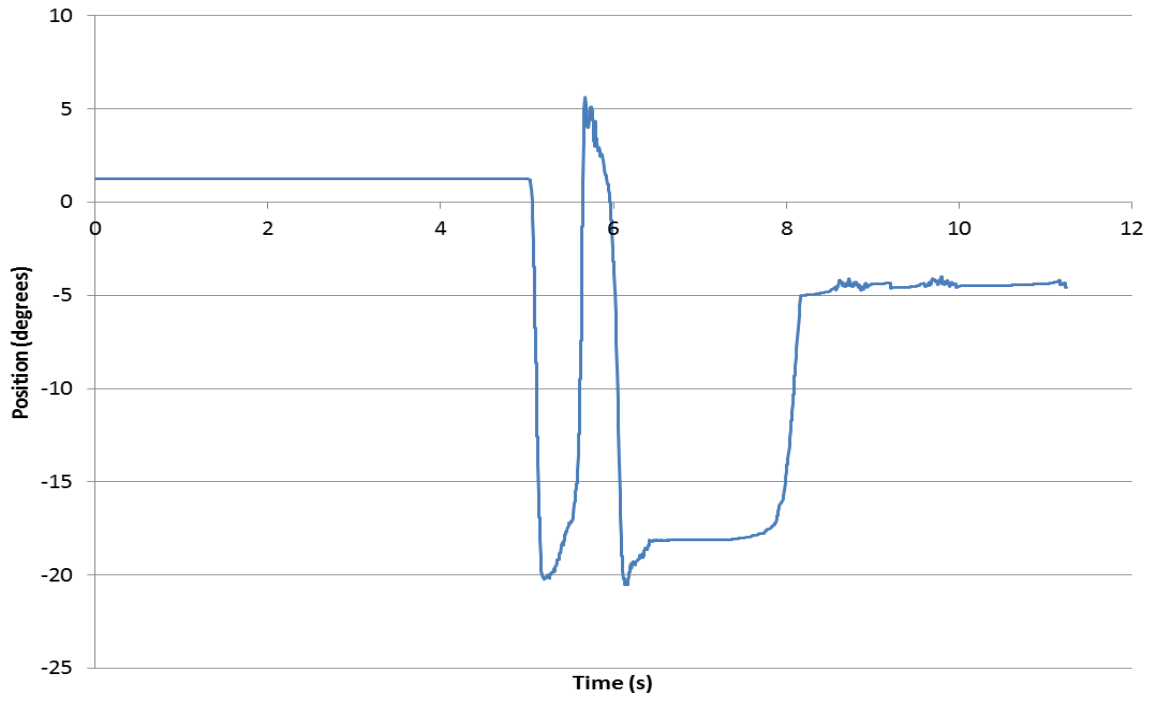


Figure 37: Test 1: Arm-motor error

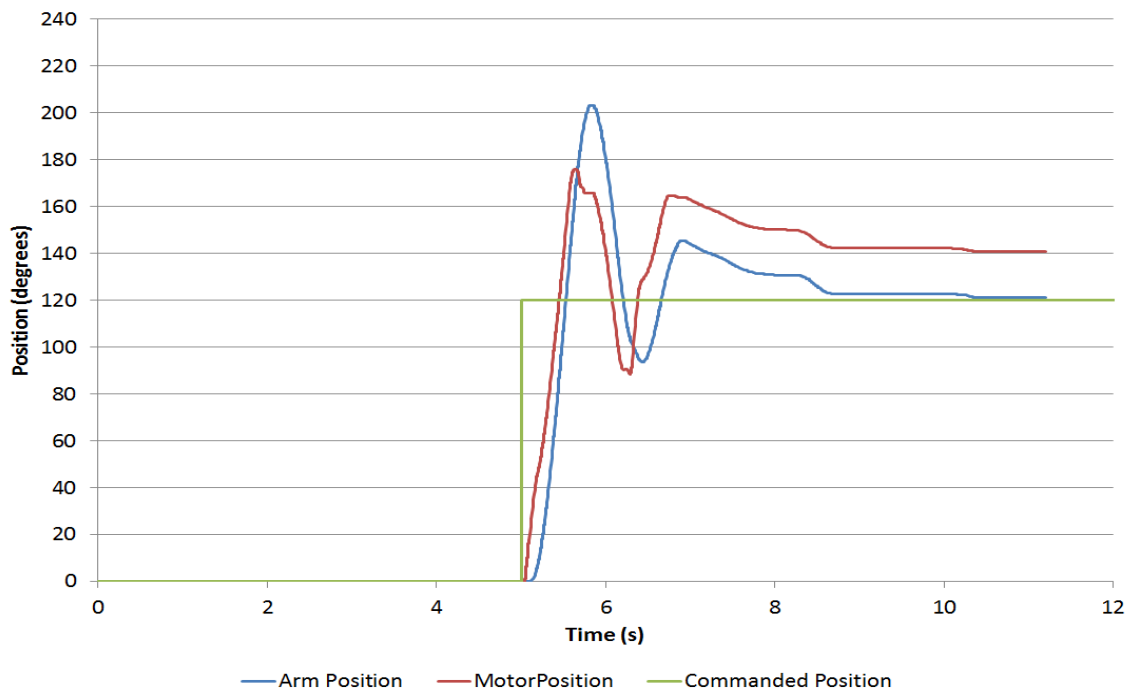
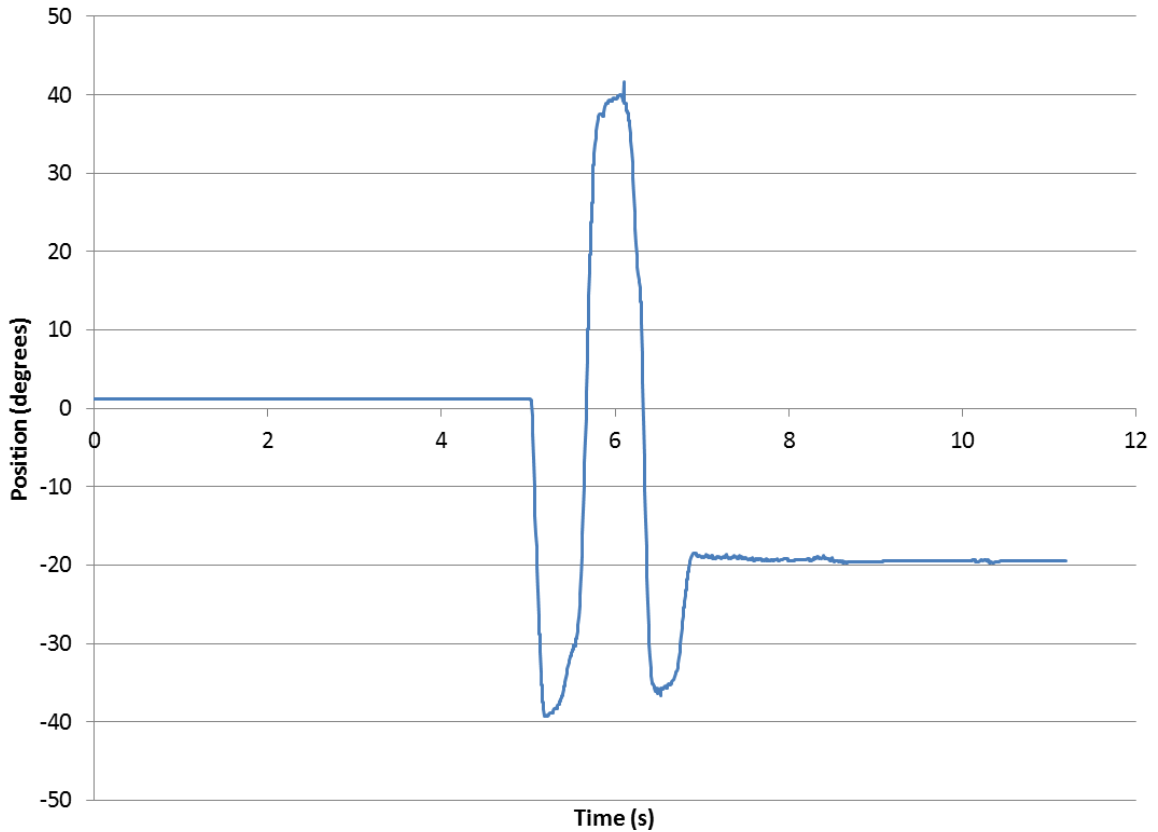


Figure 38: Test 3: Arm and Motor response



**Figure 39: Test 3: Arm-motor error**

#### **4.4 Analysis**

As stated in Section 2.2, the simulations showed that adding a variable damper will have 2 major effects on the response of the load. Firstly, the maximum overshoot will be significantly reduced, and secondly the ringing time will be significantly reduced. These experiments were conducted to test those results, and the outcome is inconclusive.

#### **4.4.1 Maximum Overshoot**

The simulations in Section 2.2 show a large reduction in the maximum overshoot of the load. Unfortunately, the experimental results do not demonstrate the same sort of improvement in the overshoot. The experimental results only show a reduction of 20° on average. There was a test that showed a reduction of 55°, but those results could not be repeated over the subsequent tests.

The primary reason for this lack of improvement is likely the .2s delay caused by the servo. Looking at the speed of the arm when it crosses the motor position, the arm had already covered a significant distance (around 20°) before the damper could respond.

With these results, the experiment cannot be said to have confirmed the improvement in maximum overshoot as predicted by the simulations in Section 2.2. There was some improvement, but not to the degree suggested by the simulations.

#### **4.4.2 Ringing Time**

The simulations in Section 2.2 show a drastic reduction in the ringing time of the system. The experimental results validate this result as in all the cases, the ringing time was decreased to at least a third of the ringing time of the SEA case. The SEAs took on average around 4 seconds to stop ringing, while the SEA-CD stopped ringing after 1 second on average.

This result would suggest that either the reduction in ringing time is not as strongly dependent on the timing as the reduction in maximum overshoot is, or with a damper that could be activated during the correct point during the motion, the reduction in ringing time would have been even greater. A 75% reduction does not leave much room for

improvement however, so it is likely that while a properly timed damper could have improved the reduction in ringing time, on the whole the reduction in ringing time is tolerant of improperly timed dampers.

## **Chapter 5**

# **MR Fluid based Controllable SEA Design**

One of the main improvements that can be made to the test bed is to replace the rotor-caliper damper with an MR damper. The MR damper is easier to mount, and has inbuilt bearings to ensure the rotating surfaces are properly aligned. MR dampers can also respond on the order of milliseconds [21] thereby eliminating the 200 ms timing delay caused by the servo.

### **5.1 Modeling an MR damper**

Before constructing a MR damper for use in a SEA-CD, it should be modeled and simulated to predict its performance, and to ensure the MR damper is neither too weak

nor too strong. The modeling of the damping torque from a MR damper is presented below

Hongsheng, Juan, Liang, Jiong and Xuezheng provide a guide for specifying the outer radius of the inner disk, and the yield stress of the MR fluid based on the desired torque output from the clutch [37]. Specifically they provide:

$$T_{tim} = \frac{2}{3}\pi(R_2^3 - R_1^3)\tau_B \quad (15)$$

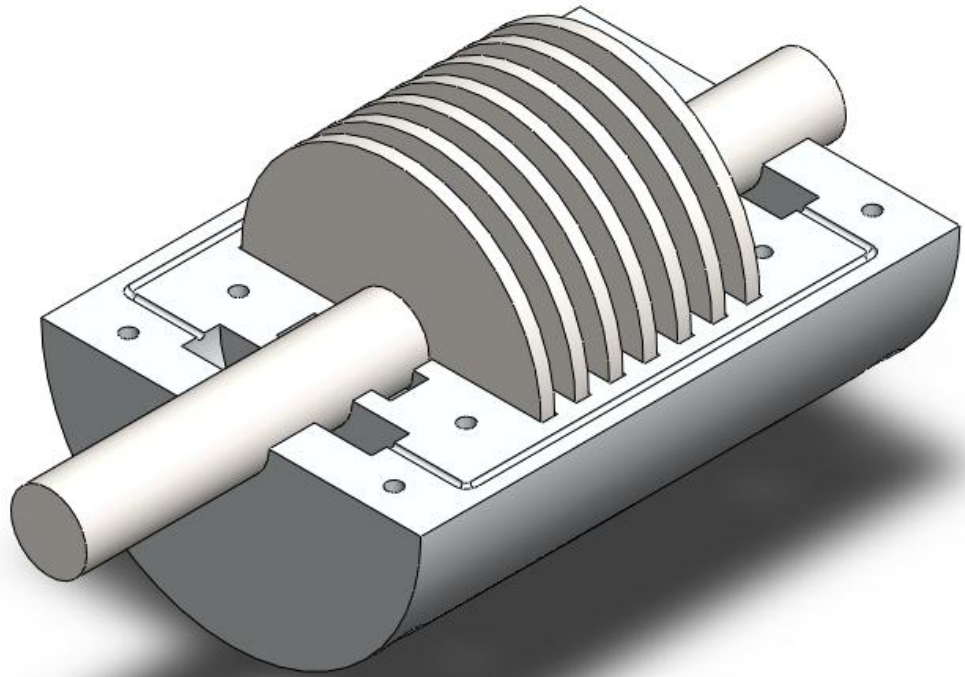
$$T_{vis} = \frac{\pi\eta \cdot |\Delta\omega|}{2h}(R_2^4 - R_1^4) \quad (16)$$

Where  $T_{tim}$  is the maximum static transmission torque,  $R_1$  is the inner radius of the inner plate,  $R_2$  is the outer radius of the inner plate,  $\tau_B$  is the yield stress of the MR fluid for a specific magnetic field strength,  $T_{vis}$  is the viscous torque from the damper,  $\eta$  is the viscosity of the MR fluid,  $\Delta\omega$  is the difference in rotational speed between the output and input shafts, and  $h$  is the working clearance between the rotating plates. The sum of Equation 15 and Equation 16 gives the total torque produced by a single face of a disk. They can be modified for a multi disk MR damper by multiplying the torque from a single disk by the number of disks (assuming the disks are identical).

$$T = n \cdot \left[ \frac{2}{3}\pi(R_2^3 - R_1^3)\tau_B + \frac{\pi\eta \cdot |\Delta\omega|}{2h}(R_2^4 - R_1^4) \right] \quad (17)$$

Where  $T$  is the total torque produced by the damper, and  $n$  is the number of faces.





**Figure 40: SolidWorks model of a prototype 7 disk (14 face) MR damper**

Another useful equation Hongsheng, Juan, Liang, Jiong and Xuezheng provide is:

$$T = 90\% \cdot \frac{2}{3} \pi R_2^3 \tau_B \quad (18)$$

Equation 18 describes the static transmission torque of a single disk MR clutch as a function of the outer radius of the inner disk, and the yield stress of the MR fluid at a given magnetic field. It is derived from Equation 15, and simplified when testing showed that the working clearance and the inner radius of the inner plate had a very small effect on the maximum static torque transmission. The torque scales with the number of disks as shown in Equation 17.

Equation 18 and Equation 17 give the maximum static torque and the dynamic torque transmission of an MR damper of the type shown in Figure 40 as a function of the properties of the MR fluid used in the damper. Therefore, the next step is to select a MR fluid.

## **5.2 Selecting an MR fluid**

It is possible to make MR fluid by mixing iron filings with oil. However, the size of the filings cannot be accurately controlled without using manufacturing techniques for the specific purpose of making evenly sized iron filings. Without evenly sized particles, the performance of the MR fluid will be inconsistent. The size of the particles will also affect the settling behavior of the fluid. Micrometer sized iron particles are too heavy to stay suspended in solution, and will eventually settle out. In contrast, nano scale particles can remain suspended indefinitely thanks to Brownian motion. The settling issue can be alleviated by adding surfactants to the suspension. Adding surfactants however causes a decrease in the magnetic saturation limit. Magnetic saturation limits are an upper limit inherent in all MR fluids where increasing the magnetic field strength no longer increases the yield stress of the fluid. This in turn imposes an upper limit on the static torque a damper can produce. The magnetic saturation limit is affected by the size of the iron particles used in the suspension. MR fluids made using nano scale particles (more commonly known as Ferrofluids) have lower magnetic saturation limits than MR fluids using micrometer scale iron particles.

As an alternative to personally making and characterizing batches of MR fluid, MR fluids can be purchased from commercial vendors, specifically from the LORD Corporation [38]. Since they tightly control the size of the iron particles, the oil base

used, and additives, these fluids would have much more consistent performance than personally produced batches. For the rest of the analysis, the MR fluid used is assumed to be Lord Corporations MR-140CG MR fluid. It has a viscosity of 0.280 Pa-s, and a max yield stress of around 60 kPa.

### 5.3 Choosing key MR damper dimensions

According to Equation 17, the two major design choices are the outer radius of the inner disk ( $R_2$ ), and the fluid gap between the disks ( $h$ ).

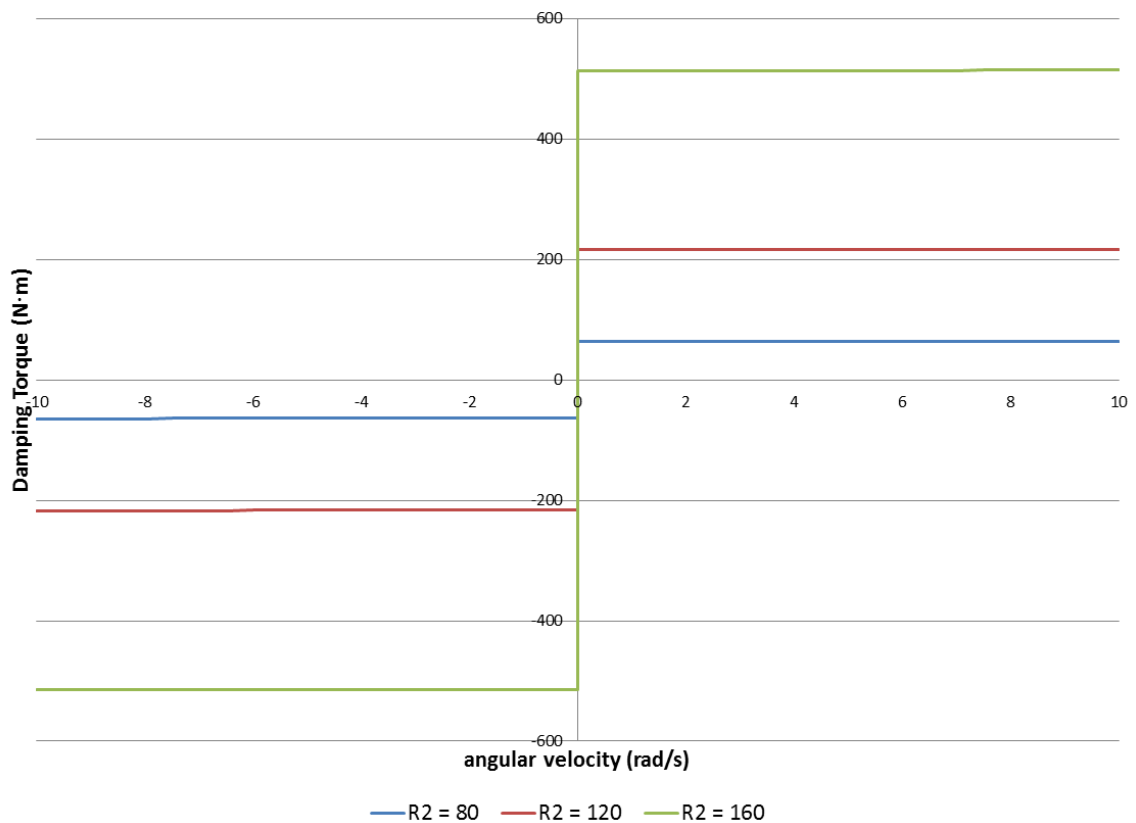
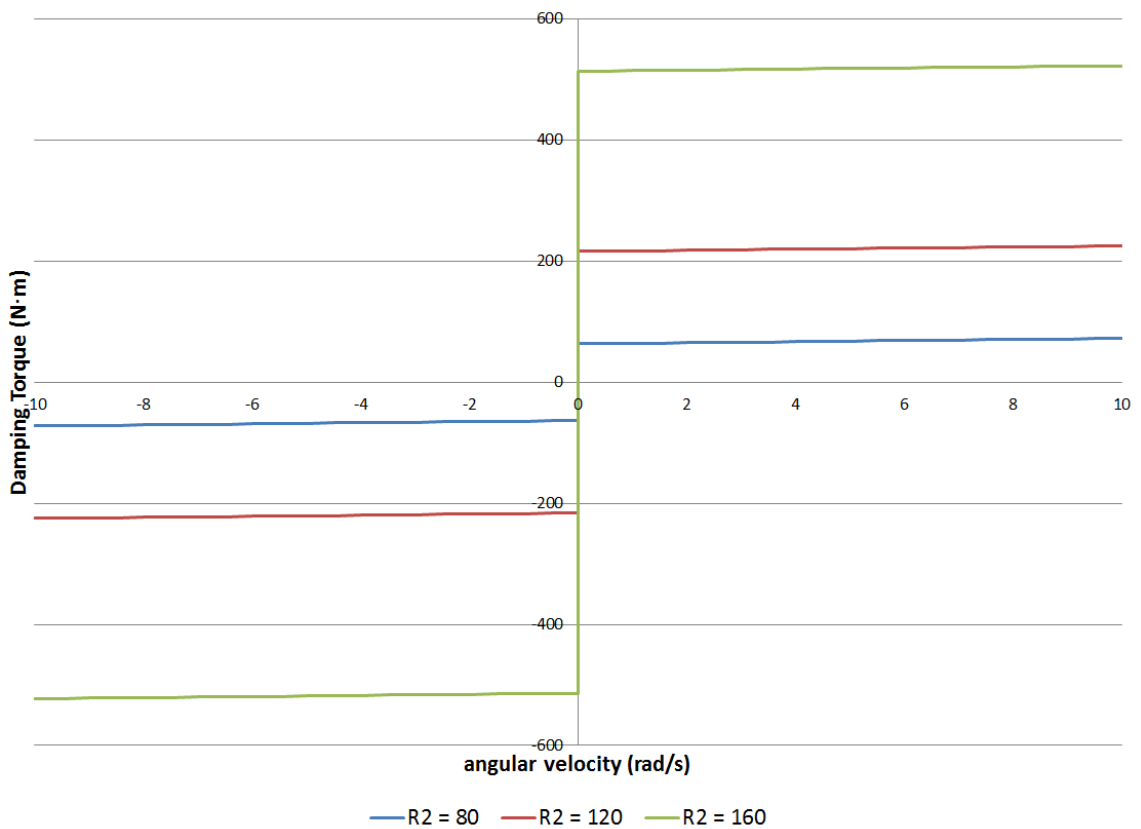


Figure 41: Comparison of Damping torque at different angular velocities ( $h = .2$  mm)

To see the effect of each on the maximum damping torque produced by the damper, two graphs were made. Figure 41 compares the maximum damping torque produced vs the angular velocity of the damper for three different  $R_2$  values, and Figure 42 is the same graph as Figure 41, but with an order of magnitude smaller fluid gap. Both graphs show the damping torque from a single face, so a single plate would produce double the torque. The other variables needed to solve the equations are listed in Table 5.



**Figure 42: Comparison of Damping torque at different angular velocities ( $h = .02$  mm)**

As can be seen in the graphs,  $R_2$  has the largest effect on the maximum damping torque the MR damper can provide. In contrast, increasing  $h$  had a very small effect, and only increased the slope of the damping torque with respect to the angular velocity. Further decreasing  $h$  might have produced greater gains in terms of increasing the slope

over the dynamic range, but there is a lower limit on how small of a fluid gap can be used. Since MR fluid is a suspension of micrometer sized iron particles, the fluid gap has to be bigger than the particles themselves. 0.20 mm is 200 microns, which is wide enough for the iron particles, but 0.02 mm is 20 microns which is approaching the size of the particles themselves.

In summary, when specifying the dimensions of the MR damper, the radius of the inner plate has the biggest effect on the maximum torque the damper can produce, and should be as large as possible. If space restrictions do not allow for a large enough plate, increasing the number of plates will also increase the maximum torque, but not by the same magnitude as the size of the plate. Finally, the fluid gap has a small effect and should be specified by machining capabilities, keeping in mind a smaller gap will use less of the expensive MR fluid.

#### **5.4 Simulation of the SEA-CD with a MR damper**

The simulation was once again an ODE placed into state space form and solved using Matlab. The basic equation is the same as the equation simulated in Section 2.2, but this time the damping torque term is more computationally intensive. The damping torque is split into two regions. One where the torques acting on the damper are greater than the maximum torque the damper can provide, and one where the torques acting on the damper are less than the maximum torque the damper can provide.

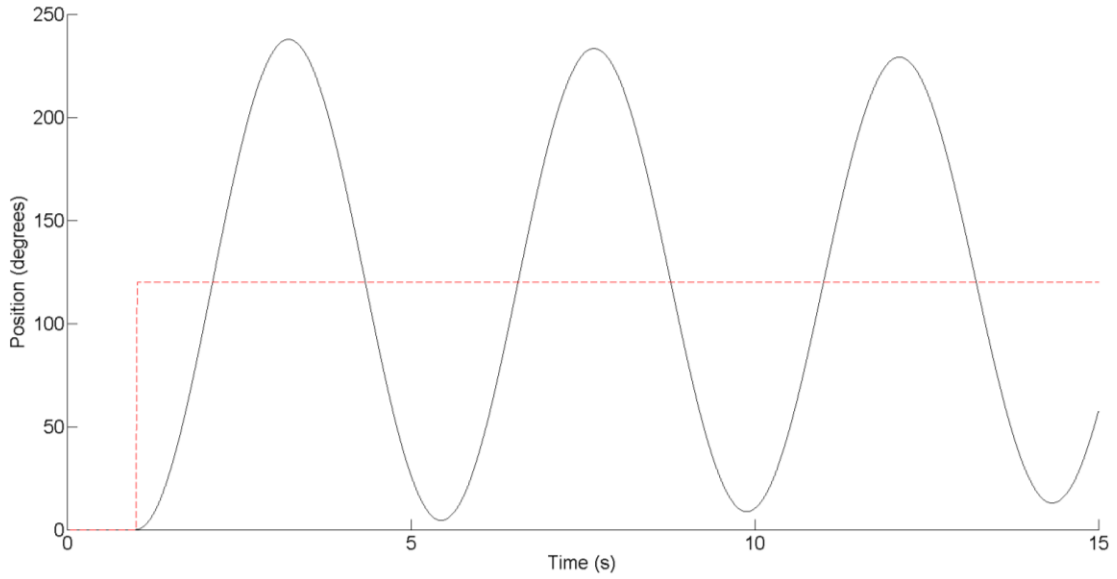
In the first case (damper torque less than the external torques), the maximum damping torque is calculated and used to calculate the position and velocities for the current time step. However, calculating the damping torque requires the current velocity

of the damper. To overcome this situation, the current velocity is substituted by the velocity during the previous time step, which is assumed to be very close to the velocity for the current time step. In the simulation, the maximum time step is restricted to 0.0001s, so this is a reasonable assumption. The same technique is used to calculate the torque from the inertia of the load, which requires the acceleration of the load to determine. In the second case (damper torque greater than external torques), the damper torque is replaced with the sum of the external torques. The other damper parameters required to solve Equation 18 are given in Table 5. Note that  $n = 2$  refers to 2 faces on a single plate, and not 2 plates.

**Table 5: Simulated MR damper specifications**

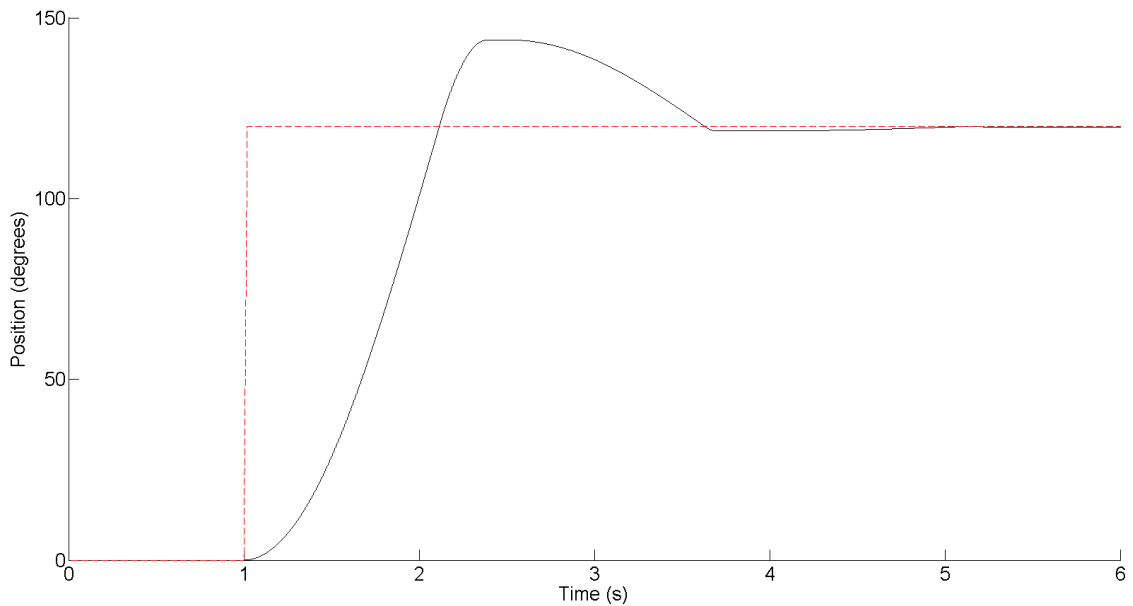
Parameter	Numerical Value	Units
$R_1$	20	mm
$R_2$	80	mm
h	0.2	mm
n	2	
$\eta$	.280	Pa-s
$\tau_B (max)$	60	kPa

The rest of the simulation proceeds as before but uses different parameters. The load is taken to be 1 kg·radian<sup>2</sup>, and the spring constant to be 2 N·m/radian. Several plots are shown below that demonstrate the performance of the damper at various yield strengths, corresponding to different magnetic fields in the MR fluid.



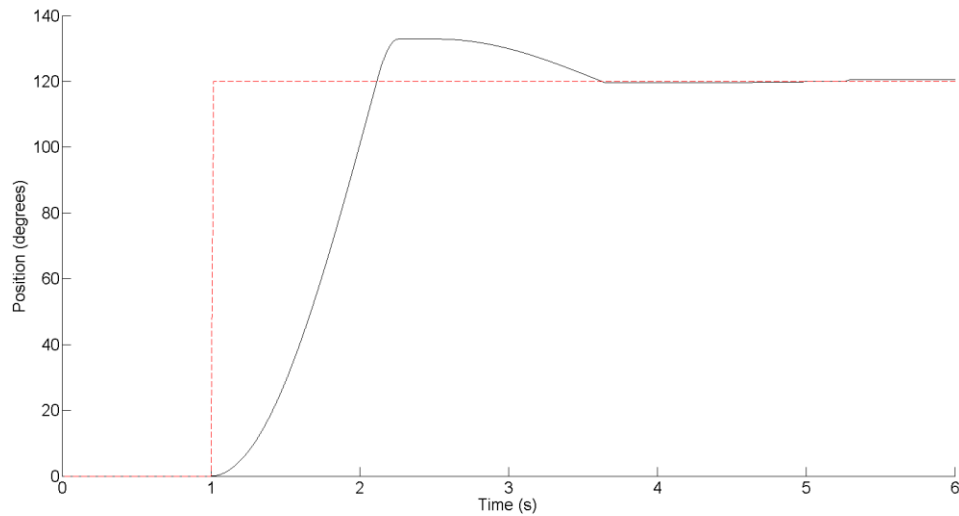
**Figure 43: No magnetic field**

Figure 43 shows the baseline response of the system, if the MR damper were never activated. There is only a small amount of damping from the dynamic damping of the MR damper.



**Figure 44: Small magnetic field  $\tau_B = 5 \text{ kPa}$**

Figure 44 shows the response of the system when using a small magnetic field. A yield stress of 5 kPa is only 8.3% of the maximum yield stress of the MR fluid. The large improvement in the response likely means the damper is too powerful for a system like this. A smaller damper would probably suffice.



**Figure 45: Higher magnetic field  $\tau_B = 10 \text{ kPa}$**

Figure 45 shows the response at a slightly higher magnetic field. This graph also shows how the simulation captures the nonlinearity of the MR damper in the static region between  $t = 2.1$  and  $t = 2.3$ , the position of the load does not move relative to the position of the arm because the external torques are not high enough to overcome the maximum static torque generated by the damper.



# Future Work

In order to eliminate some of the flaws of the physical proof of concept presented in Chapter 4, a more accurate test platform is required. A more accurate test platform will definitively prove or disprove the concept of using a variable damper to make a precise and compliant actuator. The present designs are tested for plastics, so a new platform would require a redesign of some components. Some of the parts are made for 2D fabrication, so they can be easily fabricated on a water jet. The smaller parts like the spring holders, and the rotor mount would require more complex machining. In the end however, a properly designed metal test bed would be much more accurate, and decrease the friction due to misalignment. Some parts can remain plastic, such as the arm and the spacers. Remaking those parts is suggested however. The current arm was designed to work with a rotor and caliper. Without those bulky pieces, the arm can be thinner and lighter.

The MR simulation can also be improved. The MR damper model used earlier does not account for the hysteresis in an MR damper. Several papers referenced in section 1.2.2 propose models to model the hysteresis. For instance, Ahn, Islam, and Truong propose to model the hysteresis in MR dampers via a self-tuning fuzzy control algorithm [20]. A downside of this model is that it requires a physical MR damper to create an accurate model of its hysteresis.

# Conclusion

Compliant Actuators are much safer than traditional stiff joint actuators, but at the cost of positional accuracy and speed. A solution to this shortcoming was proposed by adding a variable damper, and a control scheme that will modulate the damper during arm motion to reduce the overshoot and ringing time of the arm. The equations of motion for the system were derived, and simulated using Matlab. The simulation predicted that the precise and compliant actuator converges to the commanded position with fewer oscillations than the SEA, and has a lower initial overshoot than the SEA. Two damper control schemes were also simulated, a simple scheme that was found to be suitable for low damping rates, and a more complex one that was suitable for higher damping rates. The findings from the simulation were tested with a physical system. The results from the physical system were inconclusive as the oscillations before converging were reduced, but the initial overshoot was not reduced by the same margin the simulations showed. This was most likely the fault of the physical test platform, so a new test platform with a MR damper is proposed and simulated. The simulation captures both the dynamic and static nonlinearities of the MR damper.

The test platform can be improved by making it from tougher materials such as aluminium or steel. A non-backdriveable motor should also help in comparing the simulation results with the physical test results. Further improvements and testing should show that the SEA-CD is a good implementation of the concept of a precise and compliant actuator.

# References

- [1] "10 million awarded to family of plant worker killed by robo," *The Ottawa Citizen*, Ottawa, 1983.
  
- [2] "Trust me I'm a robot," *The Economist*, 2006.
  
- [3] J. T. C. Tan, F. Duan, Y. Zhang, R. Kato and T. Arai, "Safety Design and Development of Human-Robot Collaboration in Cellular Manufacturing," *IEEE Conference on Automation Science and Engineering*, pp. 537-542, 2009.
  
- [4] "American National Standard for Industrial Robots and Robot Systems," Robotics Industries Association, 1999.
  
- [5] G. A. Pratt and M. M. Williamson, "Series Elastic Actuators," in *Conference on Human Robot Interaction and Cooperative Robots*, 1995.
  
- [6] D. W. Robinson and G. A. Pratt, "Force Controllable Hydro-Elastic Actuator," *IEEE International Conference on Robotics and Automation*, vol. 2, pp. 1321-1327, 2000.
  
- [7] J.-J. Park and J.-B. Song, "Safe joint Mechanism using Inclined Link with Springs for Collision Safety and Positioning Accuracy of a Robot Arm," *International Conference on Robotics and Automation*, pp. 813-818, 2010.
  
- [8] R.-J. Wang and H.-P. Huang, "An Active-Passive Variable Stiffness Elastic Actuator

- for Safety Robot Systems," *International Conference on Intelligent Robots and Systems*, pp. 3664-3669, 2010.
- [9] S. Altwegg, "Torque Control of High Compliant Series Elastic Actuator," Swiss Federal Institute of Technology Zurich, 2010.
- [10] J. W. Sensinger and R. F. Weir, "Design and Analysis of a Non-backdrivable Series Elastic Actuator," *International Conference on Rehabilitation Robotics*, pp. 390-393, 2005.
- [11] J. W. Sensinger and R. F. Weir, "Unconstrained Impedance Control Using a Compact Series Elastic Actuator," *Mechatronic and Embedded Systems and Applications*, pp. 1-6, 2006.
- [12] J. Oblak, I. Cikajlo and Z. Matjacic, "Universal Haptic Drive: A Robot for Arm and Wrist Rehabilitation," *IEEE Transactions On Neural Systems and Rehabilitation Engineering*, vol. 18, pp. 293-302, 2010.
- [13] C. Lagonda, . A. C. Schouten, A. H. A. Stienen, E. E. G. Hekman and H. van der Kooij, "Design of an electric Series Elastic Actuated Joint for robotic gait rehabilitation training," *International Conference on Biomedical Robotics and Biomechanics*, pp. 21-26, 2010.
- [14] K. Kong, J. Bae and M. Tomizuka, "Control of Rotary Series Elastic Actuator for Ideal Force-Mode Actuation in Human-Robot Interaction Applications," *IEEE Transactions on Mechatronics*, vol. 14, pp. 105-118, 2009.

- [15] S. Curran and D. E. Orin, "Evolution of a Jump in an Articulated Leg with Series-Elastic Actuation," *International Conference on Robotics and Automation*, pp. 352-358, 2008.
- [16] B. T. Knox and J. P. Schmiedeler, "A Unidirectional Series-Elastic Actuator Design Using a Spiral Torsion Spring," *Brian T. Knox and James P. Schmiedeler*, vol. 131, 2009.
- [17] D. W. Robinson, J. E. Pratt, D. J. Paluska and G. A. Pratt, "Series Elastic Actuator Development for a Biomimetic Walking Robot," *International Conference on Advanced Intelligent Mechatronics*, pp. 561-568, 1999.
- [18] G. Wyeth, "Demonstrating the Safety and Performance of a Velocity Sourced Series Elastic Actuator," *IEEE International Conference on Robotics and Automation*, pp. 3642-3647, 2008.
- [19] R. Stanway, "The Development of Force Actuators using ER and MR Fluid Technology," *Actuator Development: Current Practice and new developments*, vol. 6, pp. 1-5, 2002.
- [20] K. Kwang Ahn, . M. Aminul Islam and D. Truong, "Hysteresis modeling of Magneto-Rheological (MR) fluid damper by Self Tuning Fuzzy Control," *International Conference on Control, Automation and Systems*, pp. 2628-2633, 2008.
- [21] N. Takesue, J. Furusho and Y. Kiyota, "Development and Experiments of Actuator Using MR Fluid," *Industrial Electronics Society, IECON 2000*, vol. 3, pp. 1838-

1843, 2000.

- [22] N. Takesue, J. Furusho and Y. Kiyota, "Analytic and Experimental Study on Fast Response MR-Fluid Actuator," *International Conference on Robotics and Automation*, vol. 1, pp. 202-207, 2003.
- [23] N. Takesue, J. Furusho and M. Sakaguchi, "Improvement of Response Properties of MR-Fluid Actuator by Torque Feedback Control," *International Conference on Robotics and Automation*, vol. 4, pp. 3825-3830, 2001.
- [24] A. Shafer and M. Kerman, "On the Feasibility and Suitability of MR Fluid Clutches in Human-Friendly Manipulators," *IEEE Transactions on Mechatronics*, vol. 16, pp. 1073-1082, 2011.
- [25] M. R. Ahmed and I. Kalaykov, "Semi-Active Compliant Robot Enabling Collision Safety for Human Robot Interaction," in *International Conference on Mechatronics and Automation*, 2010.
- [26] M. R. Ahmed and I. Kalaykov, "Static and Dynamic Collision Safety for Human Robot Interaction using Magneto-Rheological Fluid based Compliant Robot Manipulator," in *International Conference on Robotics and Biomimetics*, 2010.
- [27] T. Kikuchi, K. Oda and J. Furusho, "Simulation of Clonic Movement with Leg-Robot Driven by Compact MR Fluid Clutch," *International Conference on Rehabilitation Robotics*, pp. 80-85, 2009.

- [28] G. Dudek and M. Jenkin, *Handbook of Robotics*, Springer-Verlag, 2008.
- [29] P. Bagheri Ghaleh and S. M. Malaek, "On the Dynamics of the Flexible Robot Arm in a Real Deployment Profile," in *International Conference on Robotics and Automation*, 2010.
- [30] W. Zhou, C.-M. Chew and G.-S. Hong, "Property Analysis for Series MR-Fluid Damper Actuator System," *IEEE Conference on Robotics, Automation and Mechatronics*, vol. 1, pp. 560-565, 2004.
- [31] *Globe motors*, [www.globe-motors.com](http://www.globe-motors.com), 2011.
- [32] *US Digital Motion Control Products*, [www.usdigital.com](http://www.usdigital.com), 2011.
- [33] *Avid*, [www.sram.com/avid](http://www.sram.com/avid), 2011.
- [34] *HITEC RCD USA*, [www.hitecrcd.com](http://www.hitecrcd.com), 2011.
- [35] *Phidgets Inc.*, [www.phidgets.com](http://www.phidgets.com), 2011.
- [36] *National Instruments*, [www.ni.com/labview/](http://www.ni.com/labview/), 2011.
- [37] H. Hongsheng, W. Juan, C. Liang, W. Jiong and J. Xuezheng, "Design, control and test of a magnetorheological fluid fan clutch," *International Conference on Automation and Logistics*, pp. 1248-1253, 2009.
- [38] *LORD Corporation*, <http://www.lord.com/products-and-solutions/magneto-rheological-%28mr%29.xml>, 2011.

[39] *Mathworks*, <http://www.mathworks.com/products/matlab/>, 2011.



# Appendix A

## A.1 Matlab Code for the simulation in Section 2.2

```
%Code for calling the SEA or SEA-CD simulation
%Programmed by Sid Iyer

close all; clear all; clc;

global L prevq tstart;

L = 5;
counter = 0;
iter = 1;
tstart = -200;

q = [0,0,0];
t = [0,6];

options = odeset('JConstant', 'on', 'RelTol', 1e-8, 'AbsTol', 1e-8,
'MaxStep', 1e-4);
[time, q] = ode45(@SEDposfunc, t, q, options);
figure(1)
hold on
plot(time, q(:,1), '-k')
plot(time, q(:,3), '--r')
xlabel('Time (s)'); ylabel('Position (degrees)');
legend('Arm Position', 'Commanded Position', 'Location', 'best')
figure(2)
hold on
plot(time, (q(:,1)-q(:,3)));
xlabel('Time (s)'); ylabel('arm-motor error (degrees)')
```

## A.2 Matlab Code for the function called in A.1.

```
%Code for the ODEs
%Programmed by Sidharth Iyer
function [qdot] = SEDposfunc(t,q)
global L prevq tstart

k = 80;
b0 = 2;
Fs = k*(q(1)-q(3));
b = 0;

qdot = zeros(3,1);
%Inputs
Fl = 0;
```

```

if (t < 1)
    qdot (3) = 0;
elseif( t < 1.02)
    qdot(3) = 6000;
else
    qdot(3) = 0;
end

%Calculate b
%Find zero crossing

b = 0;
zerocrossing = 0;

if(t > 1.1)
    if((q(1)-q(3)) < 0 && (prevq(1)-prevq(3)) > 0)
        zerocrossing = 1;
    elseif((q(1)-q(3)) > 0 && (prevq(1)-prevq(3)) < 0)
        zerocrossing = 1;
    end
end

if(zerocrossing)
    tstart = t
end

if((t-tstart) <= .2)
    b=50;
end

qdot(1) = q(2);
qdot(2) = ((1/L)*F1) - ((1/L)*(b0+b)*(qdot(1)-qdot(3))) - ((1/L)*Fs);

prevq = q(:);
end

```

### A.3 Code for the MR damper based SEA-CD

```

% Code to simulate the behavior of the SEA-CD using an MR damper
%Coded by Sid Iyer

close all; clear all; clc;

global L prevq tstart prevqdot prevt prevFb Fb;

```

```

L = 1;
counter = 0;
iter = 1;
tstart = -200;
prevq = zeros(3,1);
prevqdot = zeros(3,1);
prevt = 0;
prevFb = 0;
Fb = 0;

%
% sim('SED.mdl');
%
% hold on;
% plot(time,x2, '-k');
% plot(time,x1, '--r');

q = [0,0,0];
t = [0,6];

options = odeset('RelTol', 1e-6, 'AbsTol', 1e-6, 'MaxStep', 1e-4);

%options = odeset('JConstant', 'on', 'RelTol', 1e-8, 'AbsTol', 1e-8);
[time, q] = ode45(@SEDposfunc, t, q, options);
qdeg = q.*(180/pi());
figure
hold on
plot(time, qdeg(:,1), '-k')
plot(time, qdeg(:,3), '--r')
xlabel('Time (s)'); ylabel('Position (degrees)');

```

#### A.4 Matlab code for the function called in A.3

```

%ODE to simulate the behavior of the SEA-CD using an MR damper
%Coded by Sid Iyer

```

```

function [qdot] = SEDposfunc(t,q)
global L prevq tstart prevqdot prevt prevFb Fb;

k = 2;
Fs = k*(q(1)-q(3));
taub = 0;
prevedot = prevqdot(1)-prevqdot(3);
n = 2;
h = 2e-3;
eta = .280;
static = 'static';
dynamic = 'dynamic';

qdot = zeros(3,1);
%Inputs
F1 = 0;
if( t > 1 && t < 1.02)
    qdot(3) = 104.71976;

```

```

else
    qdot(3) = 0;
end

%Calculate b
%Find zero crossing

%b = 0;
zerocrossing = 0;

if (t > 1.2)
    if((q(1)-q(3)) < 0 && (prevq(1)-prevq(3)) > 0)
        zerocrossing = 1;
        t
    elseif((q(1)-q(3)) > 0 && (prevq(1)-prevq(3)) < 0)
        zerocrossing = 1;
        t
    end
end

% if(t > .8 && t < 1.2)
%     zerocrossing = 1;
% end

if(zerocrossing)
    tstart = t;
end

if((t-tstart) <= .4)
    %Code for calculating the 'on' state
    taub = 40000;
end

if(t ~= prevt)
    Fb = n*(9.29357e-4)*taub;
    Fb = Fb*sign(prevedot);

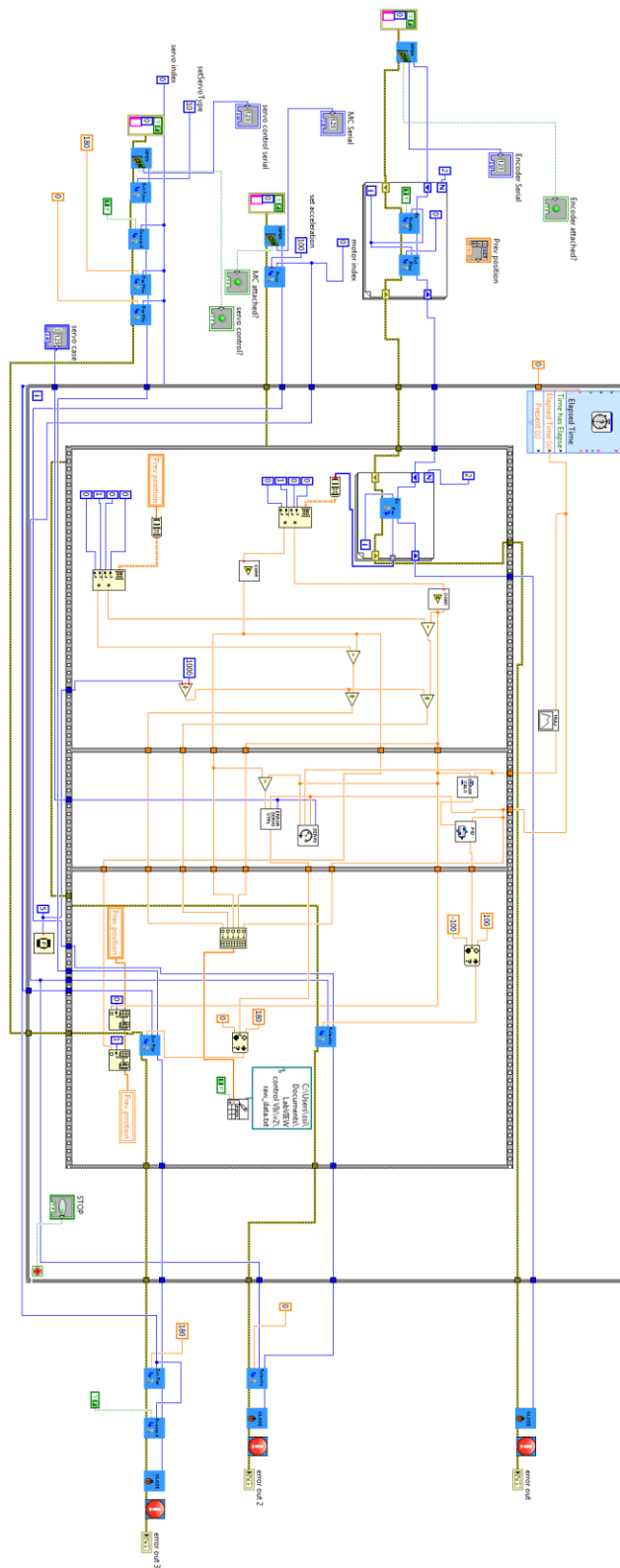
    if(abs(Fb) >= abs(-(L*prevqdot(2))+(Fs)))
        status = static;
        Fb = -(L*prevqdot(2))+(Fs);
    else
        status = dynamic;
        Fb = n*((0.00101586*taub)+((6.09313e-5)*eta*abs(prevedot)/h));
        Fb = Fb*sign(prevedot);
    end
end

qdot(1) = q(2);
qdot(2) = ((1/L)*F1)-((1/L)*Fb)-((1/L)*Fs);

```

```
prevq = q(:);  
prevqdot = qdot(:);  
prevt = t;  
prevFb = Fb;  
end
```

## A.5 LabVIEW VI used to control the test bed



# Appendix B

## Hardware Spec sheets

### B.1 Hitec HS-485HB servo specifications

<b>Motor Type:</b>	3 Pole
<b>Bearing Type:</b>	Top Ball Bearing
<b>Speed (4.8V/6.0V):</b>	0.20/0.71 sec @ 60 deg.
<b>Torque oz./in. (4.8V/6.0V):</b>	72/89
<b>Torque kg./cm. (4.8V/6.0V):</b>	5.2/6.4
<b>Size in Inches:</b>	1.57 x 0.78 x 1.49
<b>Size in Millimeters:</b>	39.88 x 19.81 x 37.85
<b>Weight ounces:</b>	1.59
<b>Weight grams:</b>	45.08

# B.2 Globe Motors motor spec sheet

**ENCODER OUTPUT WAVEFORMS**  
CW ROTATION OR MOTOR (OUTPUT SWIFT END)

REV	DESCRIPTION	DATE	BY	CHKD
1	ISSUED FOR DESIGN	01/21/04	MS	MS
2	REVISED TO REFLECT CHANGES TO MOTOR	01/21/04	MS	MS
3	REVISED TO REFLECT CHANGES TO MOTOR	01/21/04	MS	MS
4	REVISED TO REFLECT CHANGES TO MOTOR	01/21/04	MS	MS
5	REVISED TO REFLECT CHANGES TO MOTOR	01/21/04	MS	MS

**ENCODER PIN-OUTS**

PIN	FUNCTION
1	CH. A
2	CH. B
3	NC
4	VEE
5	CH. A

**NOTES:**

- ROTATION (BI-DIRECTIONAL): RED LEAD IS POSITIVE (++) AND BLACK LEAD IS NEGATIVE (-). GEARBOX OUTPUT SWIFT ROTATION IS INDICATED BY THE POSITION OF THE PULSED LEAD (CH. A). ROTATION IS COUNTERWISE VIEWING PIN END OF MOTOR SWIFT END PLAY SWIFT END IN DIRECTION SHOWN.
- OUTPUT SWIFT END PLAY: .002 TO .027 (DIMENSION IS WITH END PLAY REMOVED IN DIRECTION SHOWN).
- MOTOR PERFORMANCE (BI-DIRECTIONAL):

PARAMETER	VALUE	UNITS	TYP.
VOL. TAGE-DC	12	VOLTS	12V
NO. LOAD SPEED	16.7 (4.67)	RPM	10%
NO. LOAD CURRENT	.11	AMPS	MAX
LOAD	.22	DC IN.	NON
SPEED AT LOAD	15.7 (4.88)	RPM	12%
CURRENT AT LOAD	.14	AMPS	MAX

**REVISIONS**

REV	DESCRIPTION	DATE	BY	CHKD
1	ISSUED FOR DESIGN	01/21/04	MS	MS
2	REVISED TO REFLECT CHANGES TO MOTOR	01/21/04	MS	MS
3	REVISED TO REFLECT CHANGES TO MOTOR	01/21/04	MS	MS
4	REVISED TO REFLECT CHANGES TO MOTOR	01/21/04	MS	MS
5	REVISED TO REFLECT CHANGES TO MOTOR	01/21/04	MS	MS

**PROPERTY**

415AB32  
PACKED P/N: 125052  
DATE CODE: (YY-WK)  
REV LEVEL

**ENCODER IDENTIFICATION**

HEWLETT PACKARD OPTICAL ENCODER HENS-5505-404  
RES-5505-404  
FAIR-RITE P/N: 587500301

**GEARBOX IDENTIFICATION**

3/8 X 0.5 - 61 X .175 MAX DEEP  
3 HOLES EQUALLY SPACED DN A  
1.062 DIA BOLT CIRCLE  
Ø .010 (A/B)

**ALL DIMENSIONS UNLESS SPECIFIED ARE IN INCHES**

SECTION	DATE	BY	CHKD
DESIGN	01/21/04	MS	MS
MANUFACTURING	01/21/04	MS	MS
ASSEMBLY	01/21/04	MS	MS

**GLOBAL MOTORS, INC.**  
2075 S. 10th Street  
Mesa, AZ 85206  
TEL: 480-835-8888  
WWW.GLOBE-MOTORS.COM



## B.3 US Digital Optical Encoder spec sheet

### US DIGITAL **S4** Miniature Optical Shaft Encoder

Page 1 of 5



#### Description

The S4 miniature optical shaft encoder is a non-contacting rotary to digital converter. Useful for position feedback or manual interface, the encoder converts real-time shaft angle, speed, and direction into TTL-compatible quadrature outputs without index. The encoder utilizes an unbreakable mylar disk, metal shaft, and bushing or bearing. It operates from a single +5VDC supply.

The S4 encoder is available with ball bearings for motion control applications, or static drag to feel like a potentiometer for front-panel manual interface.

The reflective sensor incorporates an LED light source and a monolithic photo detector with signal shaping electronics, providing two channel bounceless quadrature TTL outputs.

The L-option can have the power strobed on just long enough to read the A/B outputs to reduce average power consumption. It is identical to a standard S4 except that the internal bypass capacitor is not installed. The output settling time is typically 400 nsec. after power up. The S4 should be sampled faster than (Max. RPM \* CPR / 10) Hz in this case to avoid aliasing of the quadrature waveform.

The S4 can be connected by using a high retention 4 conductor snap-in polarized 1.25mm pitch connector. The mating connector is polarized and should attach smoothly to the encoder; do not force. See below for Cables & Connectors.



#### Features

- Miniature size
- Low cost
- High retention snap-in polarized connector
- Tracks from 0 to 30,000 cycles/sec
- Ball bearing option tracks up to 7,000 or 15,000 RPM
- -10 to +85C operating temperature
- 100 to 360 cycles per revolution (CPR)
- 400 to 1440 pulses per revolution (PPR)
- 2 channel quadrature TTL squarewave outputs
- Low power strobe option available




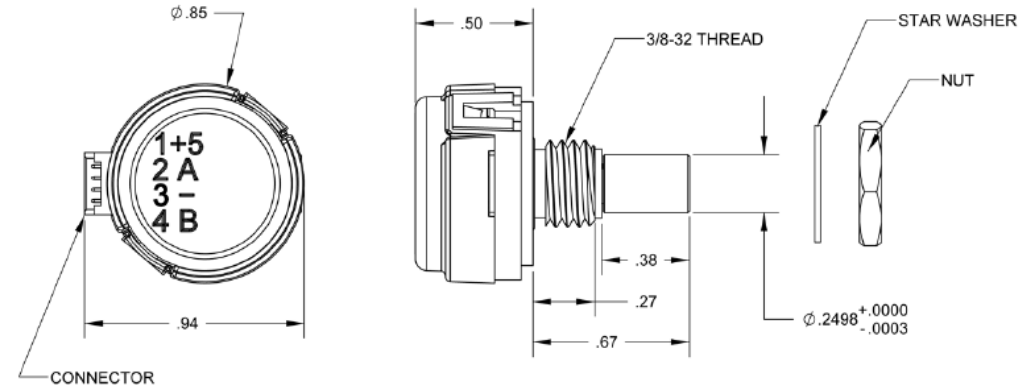
1400 NE 136th Avenue  
Vancouver, Washington 98684, USA

info@usdigital.com  
www.usdigital.com

Local: 360.260.2468  
Toll-free: 800.736.0194

Rev. 111129145348

 **Mechanical Drawing**



 **Mechanical**

Specification	Sleeve Bushing	Ball Bearing
Acceleration	10,000 rad/sec <sup>2</sup>	250,000 rad/sec <sup>2</sup>
Vibration	5 Hz to 2 kHz, 20 G	5 Hz to 2 kHz, 20 G
Shaft Speed	100 RPM max. continuous	15,000 RPM max. continuous
Shaft Torque	0.5 ±0.2 in. oz. 0.3 in. oz. max. (N-option)	0.05 in. oz.
Shaft Loading	2 lbs. max. dynamic 20 lbs. max. static	1 lb. max.
Bearing Life	> 1,000,000 revolutions	$L_{10} = (22/Fr)^3$ * Where $L_{10}$ = bearing life in millions of revs, and $Fr$ = radial shaft loading in pounds
Weight	0.46 oz.	0.42 oz.
Shaft Runout	0.0015 T.I.R. max.	0.0015 T.I.R. max.

\* only valid with negligible axial shaft loading.

 **Materials**

Shaft	Brass or Stainless
Bushing	Brass
Connector	Gold plated

### Mounting

Hole Diameter	0.375" +0.005 - 0
Panel Thickness	0.125 in. max.
Panel Nut Max. Torque	20 in.-lbs.

### Phase Relationship

B leads A for clockwise shaft rotation, A leads B for counter clockwise shaft rotation viewed from the shaft/bushing side of the encoder ( see the AEDRpage).

### Electrical

Parameter	Min.	Typ.	Max.	Units	Notes
Detector Supply Current	-	6	9	mA	
High Level Output Voltage	2.4	-	-	V	IOH = -1.2 mA
Low Level Output Voltage	-	-	0.4	V	IOL = 6.0 mA
Rise Time	-	500	-	ns	CL = 25pF, RL = 2.7kOhm
Fall Time	-	100	-	ns	
ESD	-	-	-	-	Human Body Model JESD22-A114-A Class 2 Machine Model JESD22-A115-A Class B

- Specifications apply over entire operating temperature range.
- Values are for the worst error over full rotation.
- Specifications are based on the AEDR module used in the product, together with 2.67k pull-ups on the quadrature outputs.

### Pin-out

Pin	Description
1	+5VDC power
2	A channel
3	Ground
4	B channel

### Product Change Notifications

Title	Date	Description	Download
E4 - E4P - S4 Update - PCN 1014	11/29/2011	We have modified the E4, E4P and S4 product lines in order to improve the performance and durability of the encoder. Changes include new molds for the plastic base and cover parts with an over-molded bushing in the S4 base, a new SMT connector (compatible with current mating connector), and a modified PCB profile to accommodate the new connector and plastic part modifications.	<a href="#">Download</a>

**Ordering Information**

S4 -  -  -  -

CPR	Shaft	Torque	Power
100	125 = 1/8"	D = Default	D = Default
108	236 = Metric 6mm diameter shaft	B = Ball Bearing	L = Low Power Strobe
120	250 = 1/4"	N = Light Static Drag	
125			
128			
200			
250			
256			
300			
360			

**Notes**

- For ordering information please see the Compatible Cables / Connectors section above.
- US Digital warrants its products against defects in materials and workmanship for two years. See complete warranty for details.

**Base Pricing**

Quantity	Price
1	\$51.65
10	\$43.46
50	\$38.53
100	\$34.24

- Add \$1.00 per unit for **Shaft** of Metric 6mm diameter shaft
- Add \$5.80 per unit for **Torque** of Ball Bearing

# Appendix C

## Test Results

### C.1 Results from the Undamped case

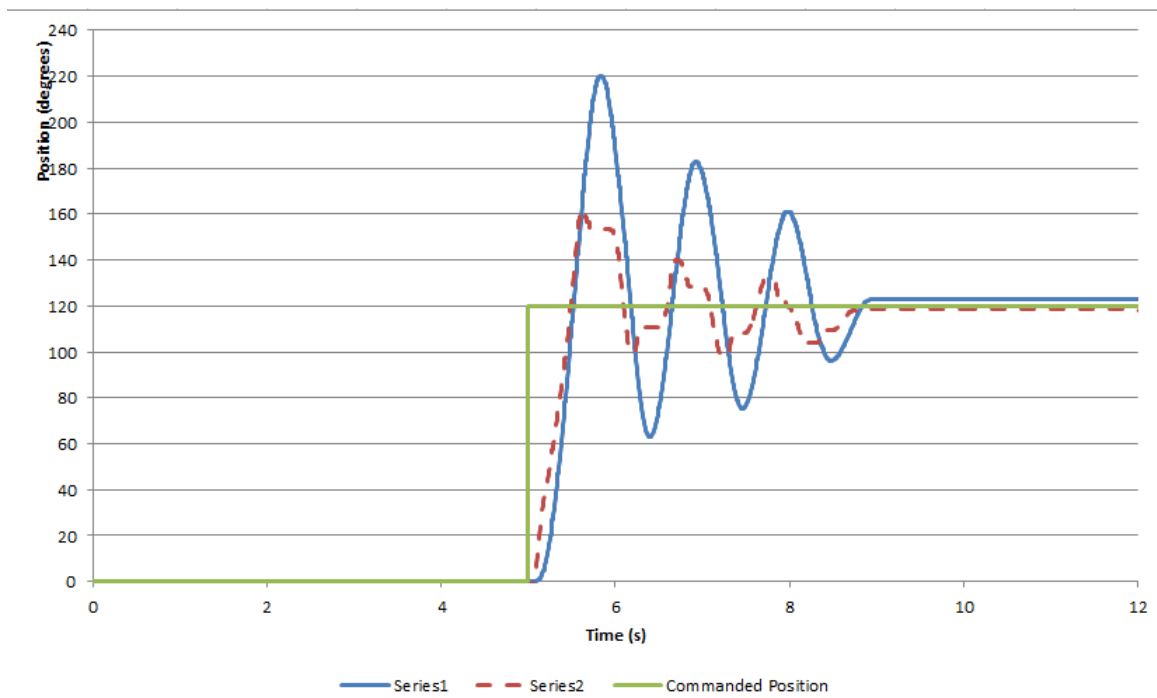


Figure 46: Test 3: Arm and Motor position

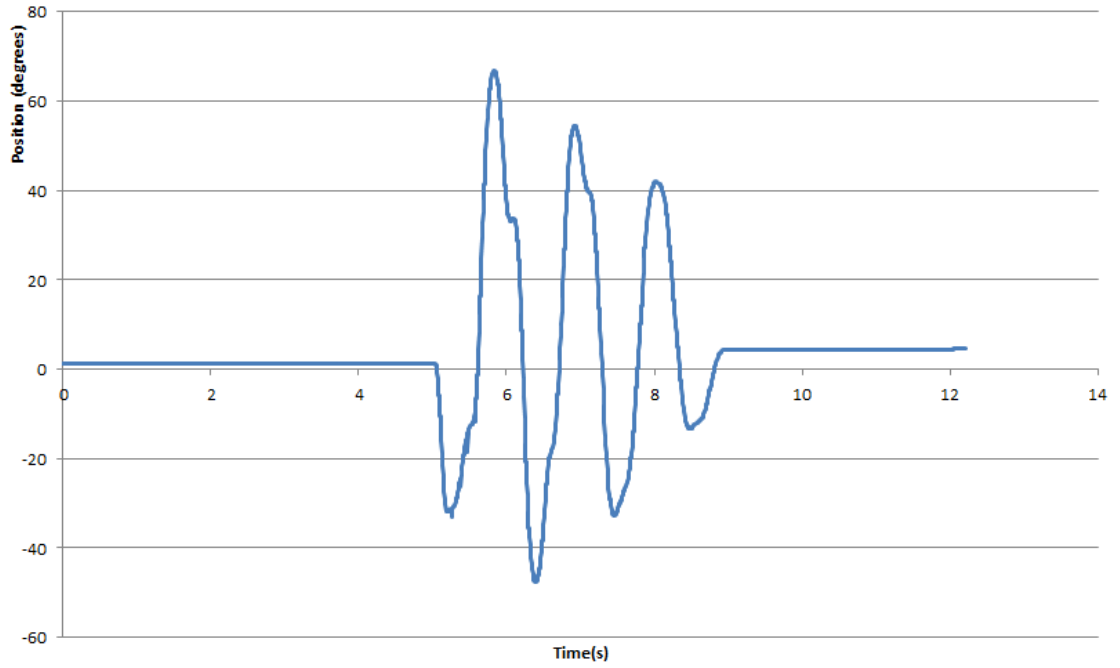


Figure 47: Test 3: Arm-motor error

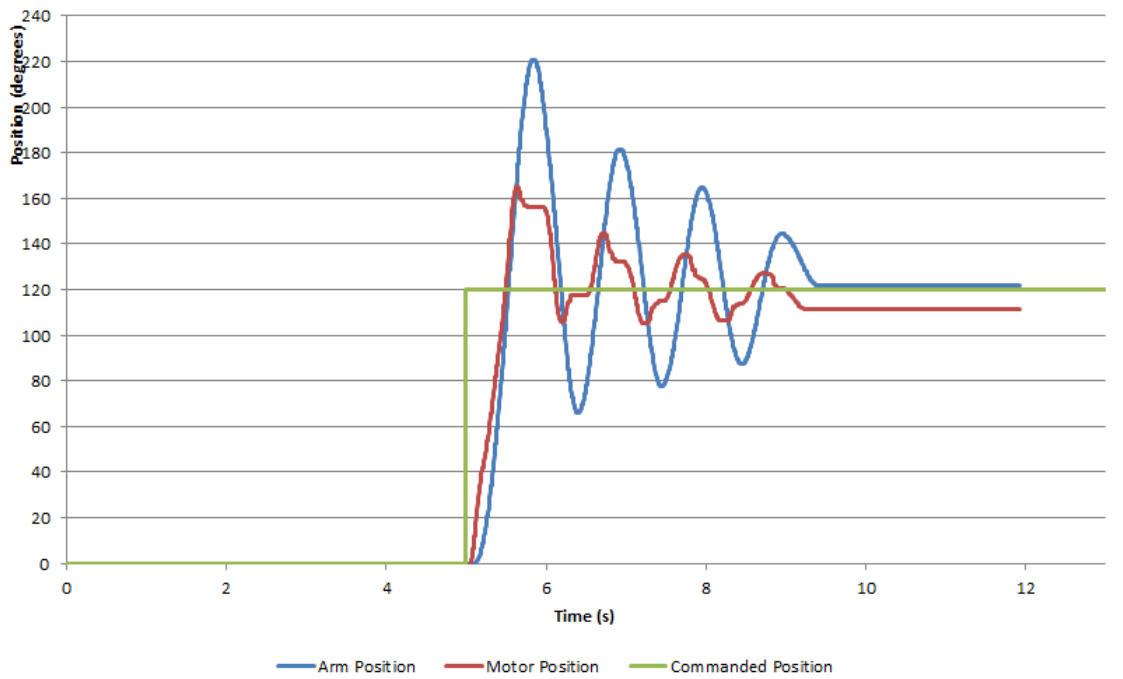


Figure 48: Test 4: Arm and Motor position

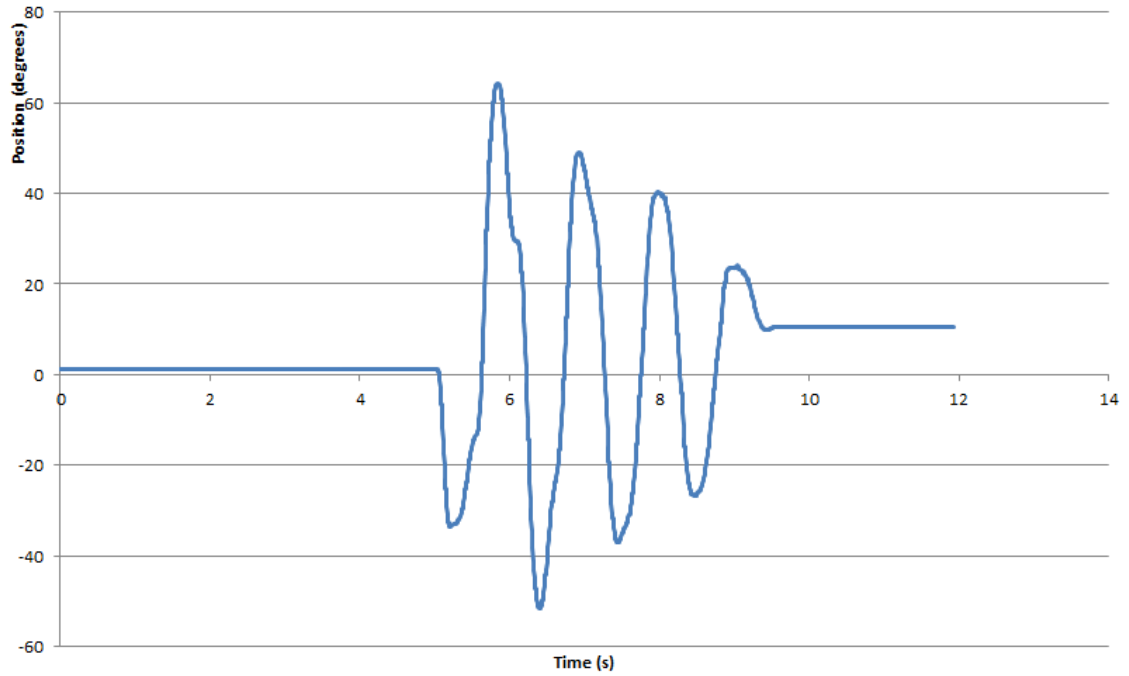


Figure 49: Test 4: Arm-motor error

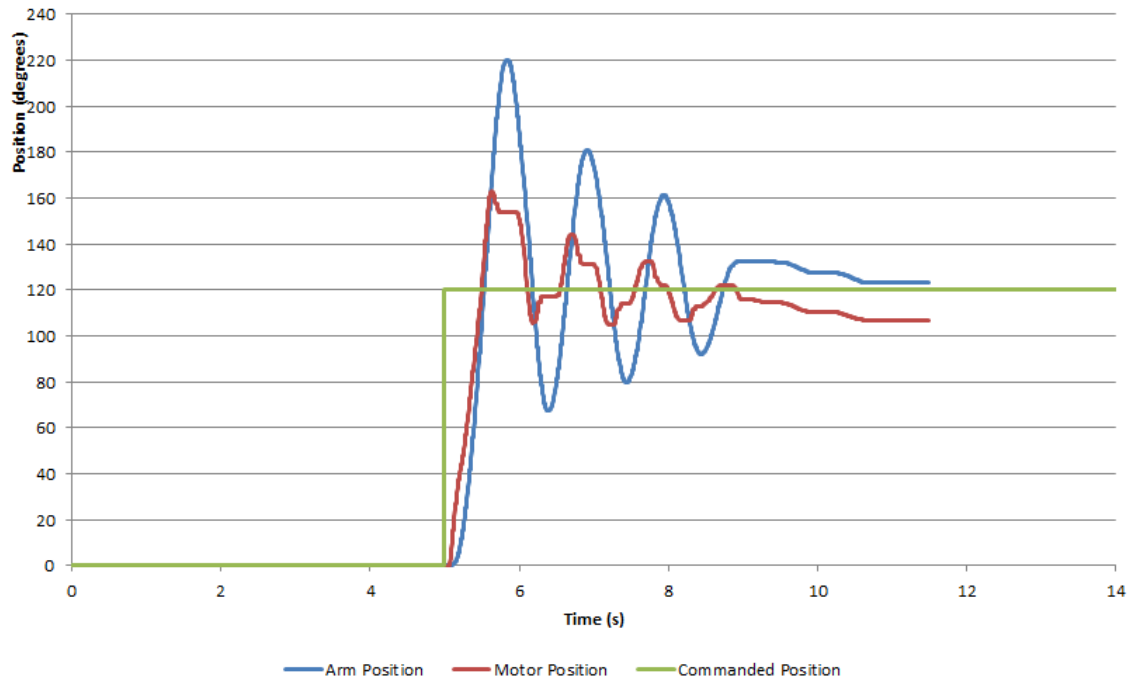
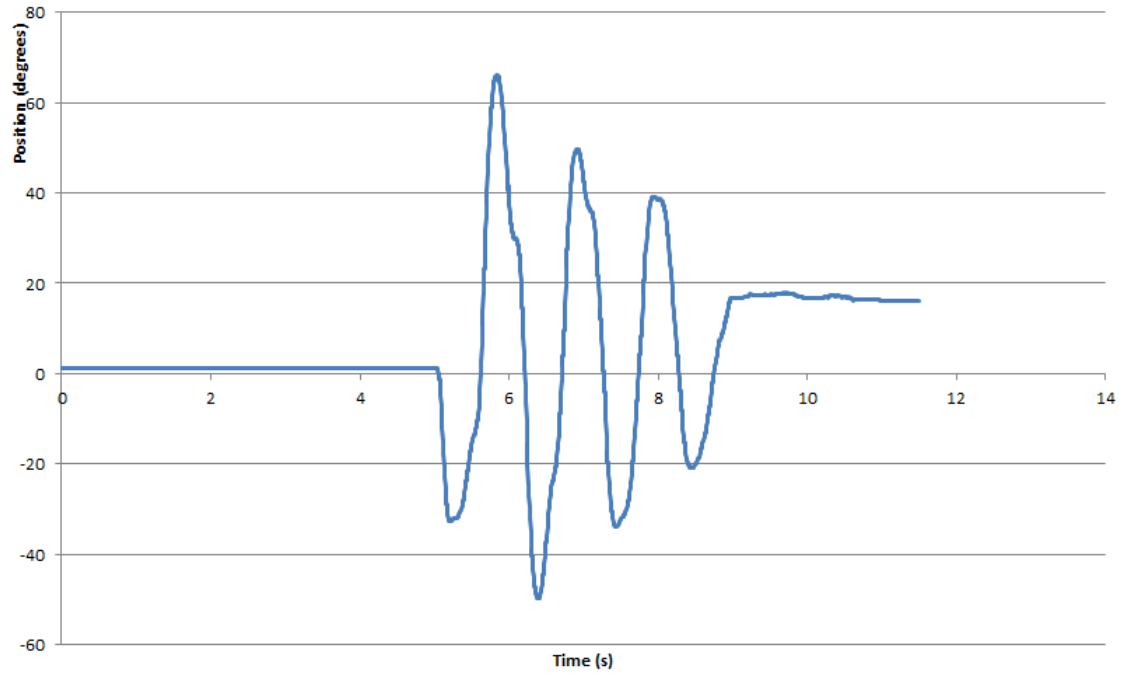


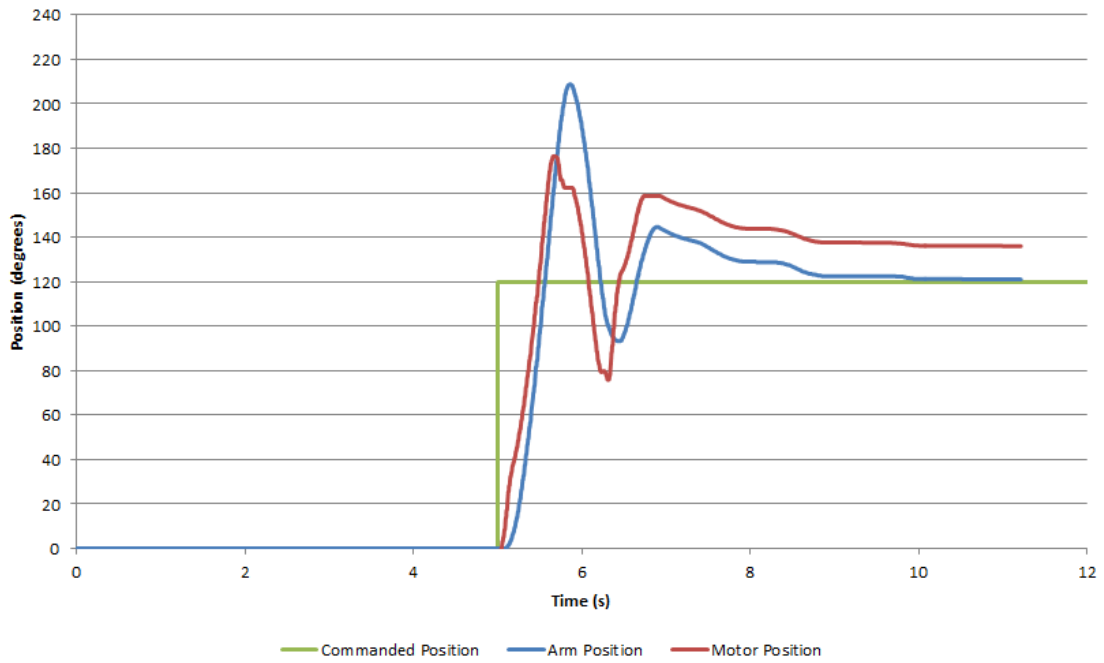
Figure 50: Test 5: Arm and Motor position



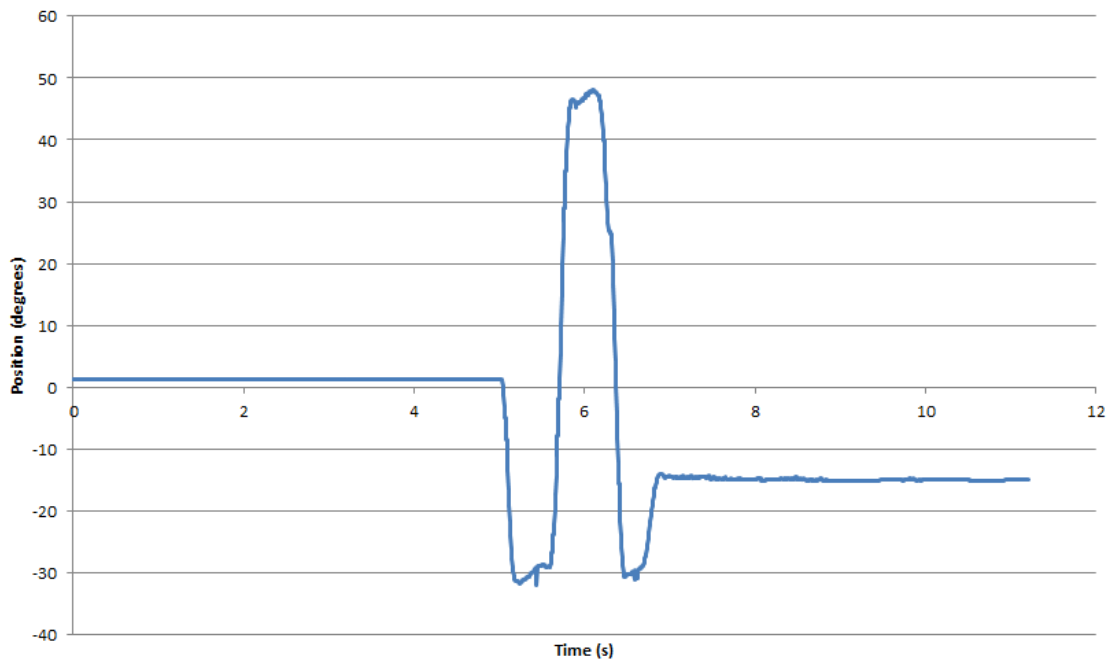


**Figure 51: Test 5: Arm-motor error**

## C.2 Results from the Controlled Damping case



**Figure 52: Test 2: Arm and Motor response**



**Figure 53: Test 2: Arm-motor error**

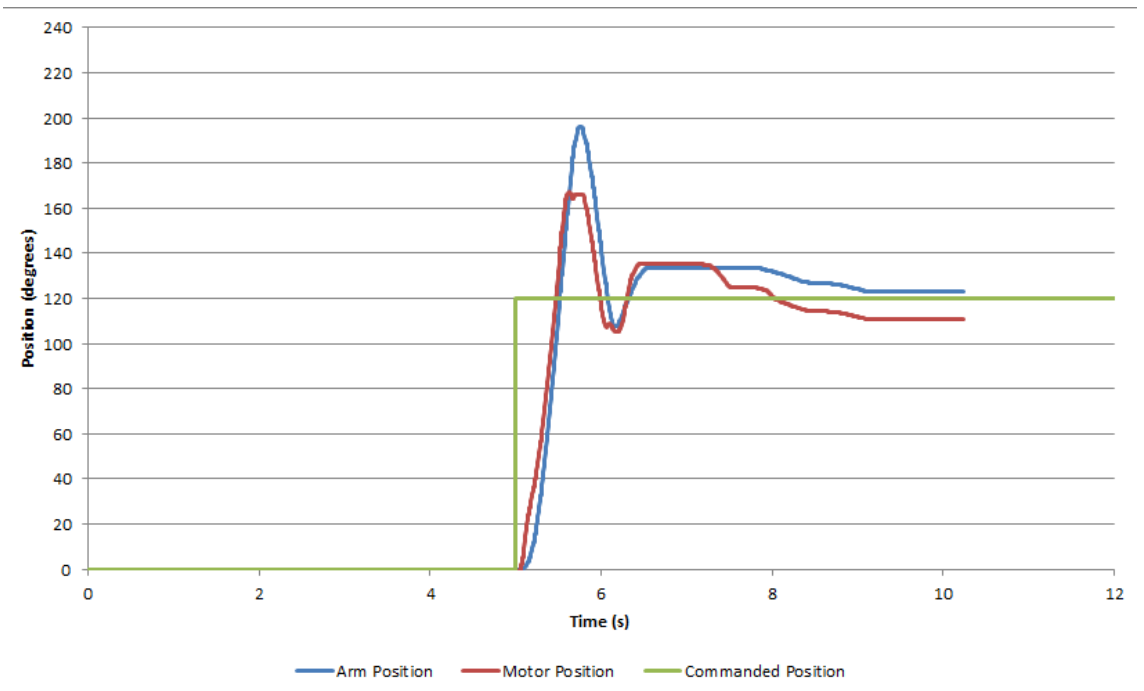


Figure 54: Test 4: Arm and Motor response

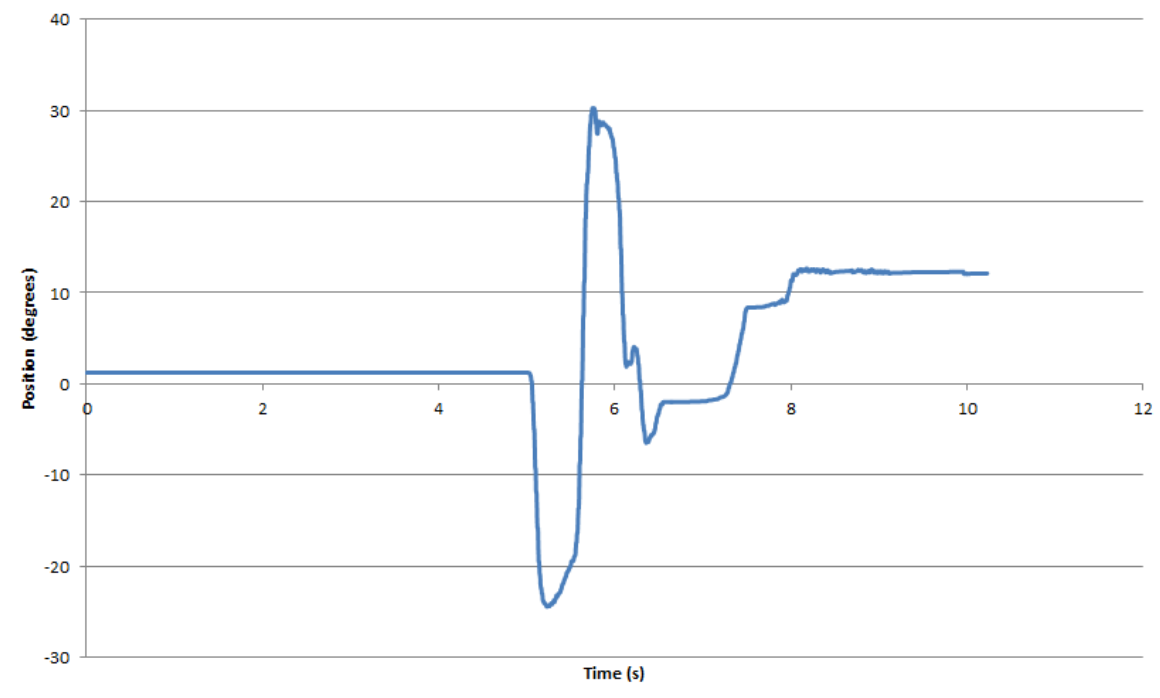


Figure 55: Test 4: Arm-motor error

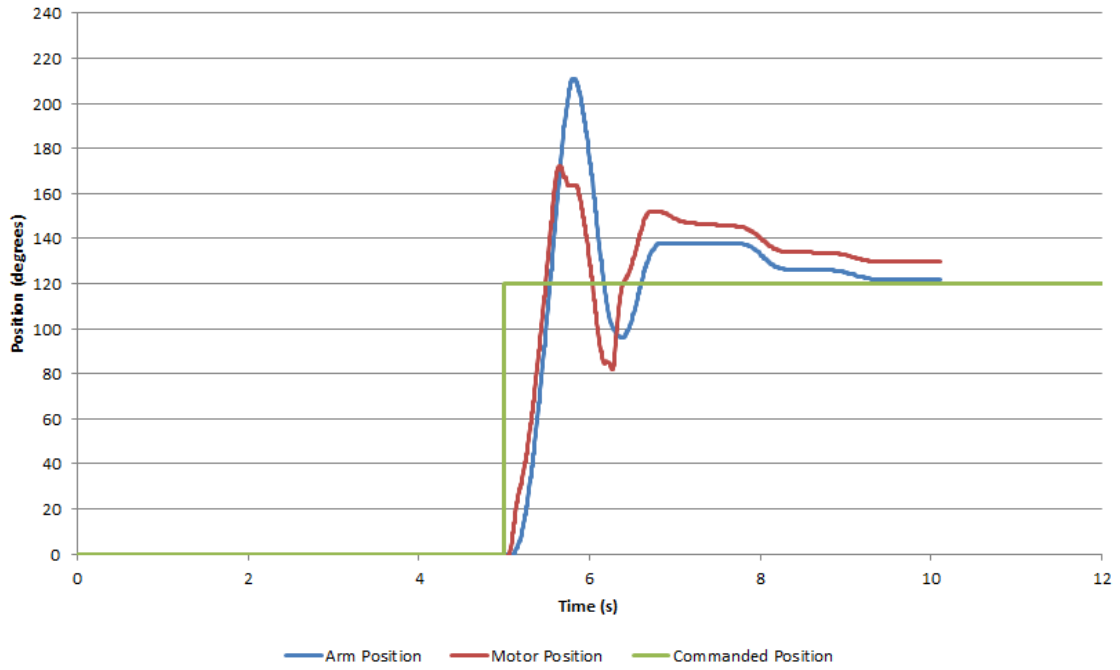


Figure 56: Test 5: Arm and Motor response

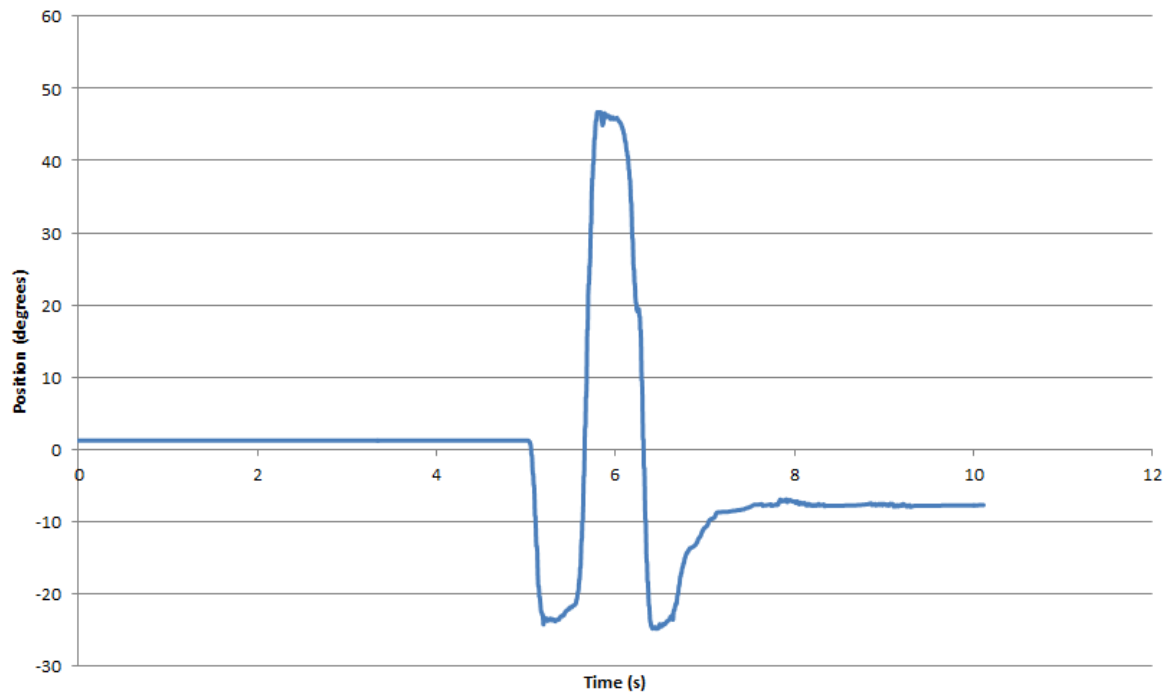


Figure 57: Test 5: Arm-motor error